



Michigan Technological University
Create the Future Digital Commons @ Michigan Tech

Dissertations, Master's Theses and Master's
Reports - Open

Dissertations, Master's Theses and Master's
Reports

2013

PROPERTIES AND STRUCTURES OF Li-N BASED HYDROGEN STORAGE MATERIALS

Junqing Zhang
Michigan Technological University

Follow this and additional works at: <https://digitalcommons.mtu.edu/etds>


 Part of the [Materials Chemistry Commons](#), and the [Physical Chemistry Commons](#)

Copyright 2013 Junqing Zhang

Recommended Citation

Zhang, Junqing, "PROPERTIES AND STRUCTURES OF Li-N BASED HYDROGEN STORAGE MATERIALS",
Dissertation, Michigan Technological University, 2013.
<https://doi.org/10.37099/mtu.dc.etds/579>

Follow this and additional works at: <https://digitalcommons.mtu.edu/etds>

 Part of the [Materials Chemistry Commons](#), and the [Physical Chemistry Commons](#)

**PROPERTIES AND STRUCTURES OF Li-N BASED
HYDROGEN STORAGE MATERIALS**

By

Junqing Zhang

A DISSERTATION

Submitted in partial fulfillment of the requirements for the degree of

DOCTOR OF PHILOSOPHY

In Materials Science and Engineering

MICHIGAN TECHNOLOGICAL UNIVERSITY

2013

© 2013 Junqing Zhang

This dissertation has been approved in partial fulfillment of the requirements for the Degree of DOCTOR OF PHILOSOPHY in Materials Science and Engineering.

Department of Materials Science and Engineering

Dissertation Advisor: *Yun Hang Hu*

Committee Member: *Jaroslav W. Drelich*

Committee Member: *Stephen A. Hackney*

Committee Member: *Feng Zhao*

Department Chair: *Stephen L. Kampe*

Table of Contents

List of Figures.....	viii
List of Tables.....	xi
Preface	xii
Acknowledgements	xiv
List of Abbreviations.....	xvi
Abstract.....	xvii
Chapter 1 Background.....	1
1.1 Why choosing hydrogen as fuel for transportation?	1
1.2 Hydrogen storage targets	3
1.3 Technologies for hydrogen storage.....	4
1.3.1 Compressing hydrogen.....	5
1.3.2 Liquefying hydrogen.....	6
1.3.3 Physical adsorption	8
1.3.4 Metal hydrides.....	9
1.3.5 Complex hydrides	10
1.3.6 Clathrate	11
1.4 Lithium nitride for hydrogen storage.....	11
1.5 Lithium nitride crystal structure and optical property	15
1.5.1 Crystal structure	15
1.5.2 Optical property	17
1.6 Lithium nitride halides structure and properties	18
1.7 Scope of this study.....	19
Chapter 2 Decomposition of lithium amide *	21
2.1 Introduction.....	21
2.2 Experiments	22
2.2.1 Sample preparations	22
2.2.2 Temperature-programmed decomposition	23
2.2.3 X-ray diffraction (XRD)	24

2.3 Results and discussion.....	25
2.4 Conclusion.....	32
Chapter 3 Decomposition of lithium imide *	33
3.1 Introduction	33
3.2 Experiments and kinetic calculation method.....	34
3.2.1 Sample preparations.....	34
3.2.2 Temperature-programmed decomposition.....	34
3.2.3 X-ray diffraction (XRD)	35
3.2.4 Kinetic calculation method for TPD-TCD peaks	35
3.3 Results and discussion.....	39
3.4 Conclusion.....	52
Chapter 4 Effect of anion promoter Cl ⁻ on the decomposition of lithium amide *	53
4.1 Introduction	53
4.2 Experiments.....	57
4.2.1 Sample preparations.....	57
4.2.2 Temperature-programmed decomposition.....	57
4.2.3 X-ray diffraction (XRD)	58
4.3 Results and discussion.....	58
4.4 Conclusion.....	63
Chapter 5 Chemical stability of lithium nitride in air*	64
5.1 Introduction	64
5.2 Experiments.....	66
5.2.1 Treatment of Li ₃ N in O ₂	66
5.2.2 Degradation of Li ₃ N in air	66
5.2.3 Characterization	67
5.3 Results and discussion.....	69
5.3.1 Oxidation of Li ₃ N in O ₂	69
5.3.2 Effect of H ₂ O in air on Li ₃ N	70
5.4 Conclusion.....	76
Chapter 6 Chemical stability of lithium nitride bromide Li ₁₃ N ₄ Br in air *	78

6.1 Introduction.....	78
6.2 Experiments	80
6.2.1 Lithium nitride bromide $\text{Li}_{13}\text{N}_4\text{Br}$ preparation	80
6.2.2 X-ray diffraction (XRD)	80
6.2.3 Temperature-programmed decomposition mass spectroscopy (TPD-MS).....	81
6.2.4 Ultraviolet–visible (UV-vis) absorption	82
6.3 Results and discussion	82
6.3.1 XRD and TPD-MS analysis	82
6.3.2 UV-vis absorption analysis	87
6.4 Conclusion	95
Chapter 7 Summary	97
References	99
Appendix	118

List of Figures

Figure 1.1 Petroleum consumption estimates by sector from 1949 to 2011 in USA [1].	1
Figure 1.2 Volumetric density of compressed hydrogen gas as a function of gas pressure comparing with the ideal gas and liquid hydrogen [7].....	5
Figure 1.3 Primitive phase diagram for hydrogen. Liquid hydrogen only exists within the blue area which is between 13.8K and 33 K [7, 8].....	7
Figure 1.4 Logarithm of dissociation pressure vs. reciprocal of absolute temperature [53].....	13
Figure 1.5 Equilibrium hydrogen pressure and reaction temperature of Reaction (1.2).	14
Figure 2.1 Thermal conductivity detector of Varian 3300 Gas Chromatograph.	23
Figure 2.2 HP 5970 series mass selective detector.	24
Figure 2.3 Scintag XDS2000 Powder Diffractometer.	25
Figure 2.4 (a) TPD-TCD profile and (b) TPD-MS profile of pure LiNH_2	27
Figure 2.5 (a) TPD-TCD profile and (b) TPD-MS profile of LiNH_2 with a cooler where produced gases were cooled to 159K before entering TCD and MS detectors.	28
Figure 2.6 XRD patterns of the solid products from the TPD process of LiNH_2 that was stopped at (a) room temperature, (b) 160 °C, (c) 330 °C, (d) 380 °C, and (e) 520 °C.	29
Figure 3.1 Typical TPD-TCD profile of a sample with a uniform gas product.....	36
Figure 3.2 TPD-TCD profile of Li_2NH . The two peaks are resolved by (A) Gaussian equation fitting and (B) kinetic calculation.	41
Figure 3.3 $\ln h_i$ vs. $(1/\text{Ti-SplnSi}/h_p\text{Tp}2)$ for the first peak of the composition of Li_2NH	44

Figure 3.4 Inhi vs. (1/Ti-SplnSi/hpTp2) for the second peak of the composition of Li_2NH .	46
Figure 3.5 XRD patterns of the solid products from the TPD process of Li_2NH that were stopped at (a) 550 °C, (b) 607 °C, (c) 650 °C, (d) 680 °C, (e) 690 °C, (f) 700 °C, and (g) 710 °C.	49
Figure 3.6 Lattice parameters of the solid products from the TPD process of Li_2NH vs. the molar fraction of Li_2NH in $\text{Li}_2\text{NH}/\text{Li}_4\text{NH}$ solid solution.	50
Figure 3.7 (a) TPD-TCD profile and (b) TPD-MS profile of Li_3N .	51
Figure 4.1 Thermal desorption profiles of H_2 and NH_3 of the ball milled mixtures of LiNH_2 and LiH with 1:1 molar ratio, in which added with a small amount (1 mol%) of Ni, Fe and Co nanometer sized metals, and VCl_3 and TiCl_3 before milling [40].	55
Figure 4.2 (A) TPD-TCD profiles and (B) TPD-MS profiles of LiCl -doped LiNH_2 with various $\text{LiNH}_2/\text{LiCl}$ mole ratios: (a) pure LiNH_2 , (b) 9:1, (c) 8:2, (d) 7:3, (e) 6:4, (f) 5:5, (g) 4:6, (h) 3:7, (i) 2:8, and (j) 1:9.	60
Figure 4.3 XRD patterns of the solid products from the TPD process of $\text{LiNH}_2/\text{LiCl}$ (8:2 molar ratio) that was stopped at various temperatures: (a) room temperature, (b) 160 °C, (c) 275 °C, (d) 320 °C, (e) 330 °C, (f) 380 °C, (g) 520 °C, and (h) 570 °C.	62
Figure 5.1 Shimadzu UV-2450 Spectrometer.	68
Figure 5.2 Perkin Elmer Spectrum One FTIR spectrometer.	68
Figure 5.3 XRD patterns of Li_3N (a) without treatment and treated with O_2 for 3 h at (b) 170 °C, (c) 230 °C, (d) 280 °C, and (e) 330 °C.	70
Figure 5.4 XRD patterns of Li_3N exposed to air for (a) 0 min, (b) 15 min, (c) 30 min, (d) 1 h, (e) 2 h, (f) 4 h, (g) 14 h (h) 32 h, and (i) 100 h.	72
Figure 5.5 FTIR spectra of Li_3N exposed to air for (a) 0 min, (b) 15 min, (c) 30 min, (d) 1 h, (e) 2 h, (f) 4 h, (g) 14 h (h) 32 h, and (i) 100 h.	74
Figure 5.6 UV-vis absorption spectra of Li_3N exposed to (A) air with relative humidity of 16% and (B) air with relative humidity of 88%.	75
Figure 5.7 UV-vis absorption spectra of individual Li_2O , LiOH , and Li_2CO_3 .	76

Figure 6.1 XRD patterns of $\text{Li}_{13}\text{N}_4\text{Br}$ in air for various time before testing. (a) Newly made $\text{Li}_{13}\text{N}_4\text{Br}$, (b) 1h, (c) 2h, (d) 4h, (e) 14h, (f) 32h and (g) 100h.	84
Figure 6.2 TPD-MS profile of $\text{Li}_{13}\text{N}_4\text{Br}$ in air for (a) 0h, (b) 1h, (d) 6h, (d) 30h, (e) 46h, and (f) 150h.	86
Figure 6.3 UV-vis absorption spectra of (A) $\text{Li}_{13}\text{N}_4\text{Br}$ and (B) $\alpha\text{-Li}_3\text{N}$ in air for various time.	87
Figure 6.4 The energy gap calculation of sample $\text{Li}_{13}\text{N}_4\text{Br}$ in air for various time. (a) Newly made $\text{Li}_{13}\text{N}_4\text{Br}$, (b) 0.5h, (c) 1h, (d) 1.5h, (e) 2h, (f) 2.5h, (g) 3h, (h) 3.5h, (i) 4h, (j) 4.5h, (k) 7.3h, (l) 9h, (m) 16.2h, (n) 27.7h, (o) 40.3h, (p) 99.3h.....	89
Figure 6.5 UV-vis absorption (at wavelength 428nm, 528nm, 628nm, and 728nm) of $\text{Li}_{13}\text{N}_4\text{Br}$ in air with time.	91
Figure 6.6 Reaction order fitting of the degradation of $\text{Li}_{13}\text{N}_4\text{Br}$ in air: $N - t$ and $\ln(N) - t$	94
Figure 6.7 Reaction order fitting of the degradation of $\text{Li}_{13}\text{N}_4\text{Br}$ in air: $1/N - t$, $1/N^{1.43} - t$, and $1/N^2 - t$	95

List of Tables

Table 1.1 Mass energy densities for various fuels [4].	2
Table 1.2 The DOE targets for onboard hydrogen storage systems for light-duty vehicles [6].	4
Table 3.1 Molar fraction of H ₂ and N ₂ produced in the decomposition of Li ₂ NH at different temperatures.	42
Table 3.2 Data obtained from the first peak of the composition of Li ₂ NH.	44
Table 3.3 Data obtained from the second peak of the composition of Li ₂ NH.	46
Table 3.4 Lattice parameters of the solid products from the TPD process of Li ₂ NH.	50
Table 5.1 Molar ratio of β-Li ₃ N to α-Li ₃ N in the Li ₃ N sample exposed to air.	73
Table 6.1 Reaction order fitting of the degradation of Li ₁₃ N ₄ Br in air.	93

Preface

Hydrogen is considered an environmentally cleaner source of energy in transportation applications. Hydrogen storage is the key issue to achieve this purpose. Lithium nitride (Li_3N) is an important material which can be used for hydrogen storage. The decompositions of lithium amide (LiNH_2) and lithium imide (Li_2NH) are important steps for hydrogen storage in Li_3N . The formation of intermediate species during the decomposition of LiNH_2 and Li_2NH has never been studied. The anion promoter effect on the decomposition of LiNH_2 has never been studied either.

In this dissertation, the research work was focused on (1) the mechanism of the decomposition of LiNH_2 ; (2) the mechanism of the decomposition of Li_2NH ; (3) the effect of anion promoter on the decomposition of LiNH_2 ; (4) the chemical stability of Li_3N in air; and (5) the chemical stability of $\text{Li}_{13}\text{N}_4\text{Br}$ in air.

My PhD work was supervised by Professor Yun Hang Hu. The work in the dissertation has been published in several peer-reviewed journals. Professor Hu and I are the only two authors in all the published papers. I performed the experiments and data analysis under the guidance of Professor Hu for the work in this dissertation. The material contained in Chapter 2 and 4 was previously published in the journal *Industrial and Engineering Chemistry Research*. The material contained in Chapter 3 was previously published in the journal *International Journal of Hydrogen Energy*. The material contained in Chapter 5 and 6 was planned for submission to the journal *Industrial and Engineering Chemistry Research*. This work would not be possible without the guidance, encouragement, and support from Professor Hu. This

dissertation would not be accomplished without the guidance, encouragement, and support from Professor Hu.

Acknowledgements

Firstly, I appreciate my advisor, Professor Yun Hang Hu, very much. He provided me financial support. He guided me how to do research, instructed me to publish journal papers, and inspired me scientific thinking. His impact on me will benefit me for the rest of my life.

Next, I would like to thank all faculty and staff in Materials Science and Engineering Department at Michigan Tech for their help and support. Especially, I would like to thank my committee members: Professor Jaroslaw W. Drelich, Professor Stephen A. Hackney, and Professor Feng Zhao for reading my dissertation, listening to my presentation, and giving constructive suggestions. Also, I would like to express my appreciation to Professor Stephen L. Kampe, Professor Mark Plichta, Professor Douglas Swenson, Professor Peter D. Moran, and Professor Jiann-Yang (Jim) Hwang, for their guidance and encouragement.

Thanks are given to Stephen F. Forsell, Paul Fraley, Owen P. Mills, Edward A. Latitila, Patrick Quimby, Margaret Rothenberger, Beth Ruohonen, and Ruth Kramer for their assistance in chemicals ordering, experiments build up, and equipments operations.

I also would like to thank my research group members, Lei Zhang, Yan Huo, Sanchai Kuboon, Pubodee Ratana-Arsanarom, Hui Wang, Peifu Cheng, Bing Han, and Wei Wei, for their assistance and help on my research works. Also, I would like to thank Andrew Galerneau on the Fourier transform infrared spectroscopy measurement.

Finally, I would like to thank my family and friends for all their supports and encouragements. Without them, I would never have accomplished what I have.

List of Abbreviations

Abbreviation	Full name
FTIR	Fourier transform infrared spectroscopy
GC	gas chromatography
MS	mass spectrometry
TCD	thermal conductivity detector
TPD	temperature programmed decomposition
XRD	X-ray diffraction

Abstract

Traditional transportation fuel, petroleum, is limited and nonrenewable, and it also causes pollutions. Hydrogen is considered one of the best alternative fuels for transportation. The key issue for using hydrogen as fuel for transportation is hydrogen storage. Lithium nitride (Li_3N) is an important material which can be used for hydrogen storage. The decompositions of lithium amide (LiNH_2) and lithium imide (Li_2NH) are important steps for hydrogen storage in Li_3N . The effect of anions (e.g. Cl^-) on the decomposition of LiNH_2 has never been studied. Li_3N can react with LiBr to form lithium nitride bromide $\text{Li}_{13}\text{N}_4\text{Br}$ which has been proposed as solid electrolyte for batteries.

The decompositions of LiNH_2 and Li_2NH with and without promoter were investigated by using temperature programmed decomposition (TPD) and X-ray diffraction (XRD) techniques. It was found that the decomposition of LiNH_2 produced Li_2NH and NH_3 via two steps: LiNH_2 into a stable intermediate species ($\text{Li}_{1.5}\text{NH}_{1.5}$) and then into Li_2NH . The decomposition of Li_2NH produced Li , N_2 and H_2 via two steps: Li_2NH into an intermediate species — Li_4NH and then into Li . The kinetic analysis of Li_2NH decomposition showed that the activation energies are 533.6 kJ/mol for the first step and 754.2 kJ/mol for the second step. Furthermore, XRD demonstrated that the Li_4NH , which was generated in the decomposition of Li_2NH , formed a solid solution with Li_2NH . In the solid solution, Li_4NH possesses a similar cubic structure as Li_2NH . The lattice parameter of the cubic Li_4NH is 0.5033nm.

The decompositions of LiNH_2 and Li_2NH can be promoted by chloride ion (Cl^-). The introduction of Cl^- into LiNH_2 resulted in the generation of a new NH_3 peak at low temperature of 250°C besides the original NH_3 peak at 330°C in TPD profiles. Furthermore, Cl^- can decrease the decomposition temperature of Li_2NH by about 110°C .

The degradation of Li_3N was systematically investigated with techniques of XRD, Fourier transform infrared (FT-IR) spectroscopy, and UV-visible spectroscopy. It was found that O_2 could not affect Li_3N at room temperature. However, H_2O in air can cause the degradation of Li_3N due to the reaction between H_2O and Li_3N to LiOH . The produced LiOH can further react with CO_2 in air to Li_2CO_3 at room temperature. Furthermore, it was revealed that $\alpha\text{-Li}_3\text{N}$ is more stable in air than $\beta\text{-Li}_3\text{N}$.

The chemical stability of $\text{Li}_{13}\text{N}_4\text{Br}$ in air has been investigated by XRD, TPD-MS, and UV-vis absorption as a function of time. The aging process finally leads to the degradation of the $\text{Li}_{13}\text{N}_4\text{Br}$ into Li_2CO_3 , lithium bromite (LiBrO_2) and the release of gaseous NH_3 . The reaction order $n = 2.43$ is the best fitting for the $\text{Li}_{13}\text{N}_4\text{Br}$ degradation in air reaction. $\text{Li}_{13}\text{N}_4\text{Br}$ energy gap was calculated to be 2.61 eV .

Chapter 1 Background

1.1 Why choosing hydrogen as fuel for transportation?

Transportation consumes around 2/3 of petroleum in USA during the last few decades (Figure 1.1) [1]. Petroleum on earth, which is limited and nonrenewable, will be used up in the future. From the environment protection point of view, transportation by using petroleum based fuel (gasoline or diesel) can produce greenhouse gases, such as carbon dioxide (CO_2), which can cause global warming. Furthermore, Carbon monoxide (CO), nitrogen oxides (NO_x) and sulfur oxide (SO_x) from the exhaust gas of petroleum based fuel vehicles have been shown to have variety of negative effects on public health and the natural environment. So, it is necessary and urgent to find an alternative fuel.

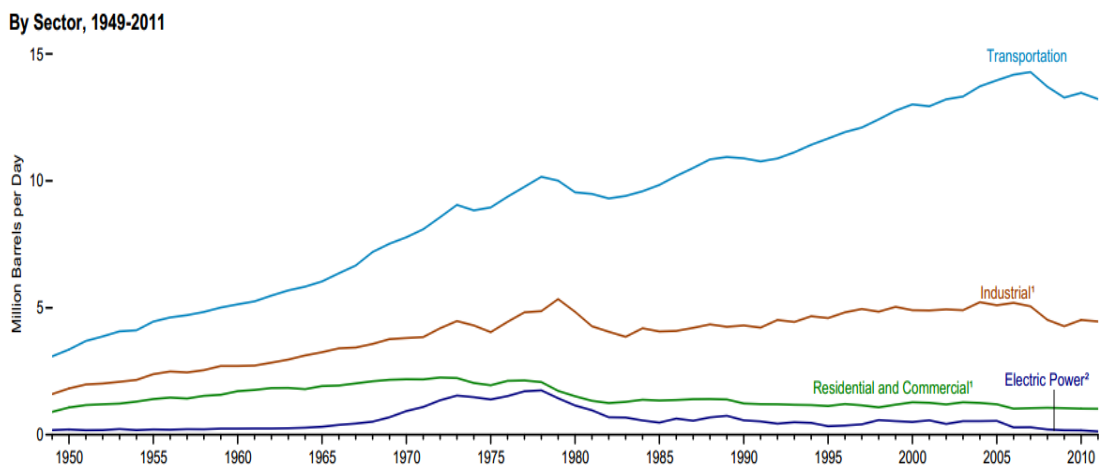



Figure 1.1 Petroleum consumption estimates by sector from 1949 to 2011 in USA [1]. (Reprinted from U.S. Energy Information Administration)

Hydrogen, the most abundant element in the universe, is considered one of the best alternative fuels for transportation [2, 3]. Firstly, the mass energy density of hydrogen is much higher than other common fuels (Table 1.1) [4]. Secondly, by using hydrogen as fuel for transportation, it can reduce the dependence on petroleum. Thirdly, H₂O is only a product which is clean and no pollution to the environment. Lastly, the hydrogen fuel cell efficiency (more than 60%) is significantly higher than those powered by internal combustion engines (the internal combustion engine energy efficiency is only around 20%) [5].

Table 1.1 Mass energy densities for various fuels [4]. (Reprinted from DOE)



Fuel	Hydrogen weight fraction	Ambient state	Mass energy density (MJ/kg)
Hydrogen	1	Gas	120
Methane	0.25	Gas	50 (43) ²
Ethane	0.2	Gas	47.5
Propane	0.18	Gas (liquid) ¹	46.4
Gasoline	0.16	Liquid	44.4
Ethanol	0.13	Liquid	26.8
Methanol	0.12	Liquid	19.9

(1) A gas at room temperature, but normally stored as a liquid at moderate pressure.

(2) The larger values are for pure methane. The values in parantheses are for a “typical” Natural Gas.

1.2 Hydrogen storage targets

The key issue for using hydrogen as fuel for transportation is hydrogen storage. Hydrogen has the highest gravimetric energy densities of any known fuels (Table 1.1) [4]. However, its volumetric energy density is only a quarter of that of gasoline (8 MJ/L for liquid hydrogen versus 32 MJ/L for gasoline). At 1 atm and room temperature, 2 g hydrogen gas has a volume of around 22.4 liters. So, it's a challenge to store hydrogen gas with such a low volumetric energy density, especially for the given requirements to achieve a driving range of greater than 300 miles (500 km) which is comparable with today's gasoline driven automobiles [6].

The DOE has performed a partnership with the U.S. DRIVE, the U.S. Council for Automotive Research, and major energy and utility companies to develop targets for onboard hydrogen storage systems for light-duty vehicles. The goal of the targets is to meet packaging, cost, safety, and performance requirements to be competitive with comparable vehicles in the market place [6]. The DOE targets for onboard hydrogen storage systems for light-duty vehicles are listed in table 1.2.

Table 1.2 The DOE targets for onboard hydrogen storage systems for light-duty vehicles [6]. (Reprinted from DOE)

storage parameter	Units	2015	Ultimate
system gravimetric capacity	wt. %	5.5	7.5
system volumetric capacity	g/L	40	70
H ₂ delivery temperature (min. /max.)	°C	-40/85	-40/95-105
operating pressure (min./max.) fuel cell	bar	5/12	3/12

1.3 Technologies for hydrogen storage

An effective hydrogen storage technology, which provides high storage capacity, suitable operating temperature, and fast kinetics, is a critical factor in the development of hydrogen fuel for transportation [2, 6]. So far, three types of technologies are available to store hydrogen: compressing hydrogen, liquefying hydrogen, and hydrogen storage in solid materials. In general, hydrogen storage in solid materials is achieved via two processes: physical adsorption, in which hydrogen is adsorbed on the surface of solid materials, and chemical reactions, in which hydrogen reacts with solid materials to form new compounds.

1.3.1 Compressing hydrogen

Compressing hydrogen is the easiest and commonest way for hydrogen storage. According to the ideal gas law, at constant temperature, increasing the gas pressure will reduce the gas volume, and improve the gas volumetric density. As shown in Figure 1.2, there is a deviation of the H_2 gas from the ideal gas, especially at high pressure. With increasing pressure, the volumetric density of the hydrogen gas increases and reaches the maximum at about 55 kg/m^3 . Further increasing of the hydrogen gas pressure has little impact on the volumetric density of the compressed hydrogen gas.

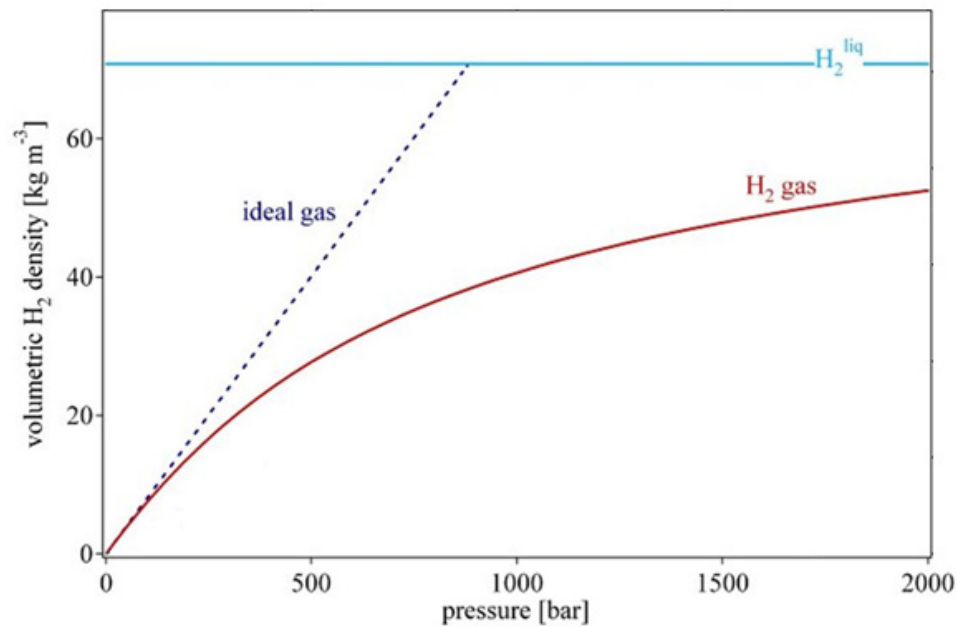


Figure 1.2 Volumetric density of compressed hydrogen gas as a function of gas pressure comparing with the ideal gas and liquid hydrogen [7]. (With permission from Springer)

For the reality use of storing enough hydrogen fuel for a reasonable driving range of 400-500 km, compressing hydrogen requires a very high pressure (up to 700 bar), and this causes a safety issue related to tank rupture in an accident [3]. Large amount of energy is also needed to reach this high pressure.

1.3.2 Liquefying hydrogen

Storing hydrogen in a liquid state has higher energy density than compressing hydrogen. It is a technology used in NASA's Space Shuttle programs. However, the drawbacks with liquefying hydrogen are the big energy requirement for hydrogen liquefaction, hydrogen boil-off, and tank cost.

As shown in the primitive phase diagram for hydrogen (Figure 1.3), there is no liquid phase above the critical temperature, 33 K [7, 8]. To exist as a liquid, hydrogen must be cooled to its critical point (33 K). Liquid hydrogen is stored in cryogenic tanks at 20.28 K at ambient pressure. It needs large amount of energy to liquefy hydrogen from room temperature to this low temperature. Moreover, all of the components for storage and delivery of the liquid hydrogen must also be cooled to this low temperature, which leads to a further energy cost.

Because there is no liquid phase of hydrogen existing above its critical temperature (33 K), liquid hydrogen can only be stored at open systems. Otherwise, in a closed storage system, the hydrogen pressure at room temperature could reach to

about 10^4 bar [7]. Thus, continuous boil-off of liquid hydrogen is unavoidable. Therefore, liquefying hydrogen for on-board use is not an energy efficient method.

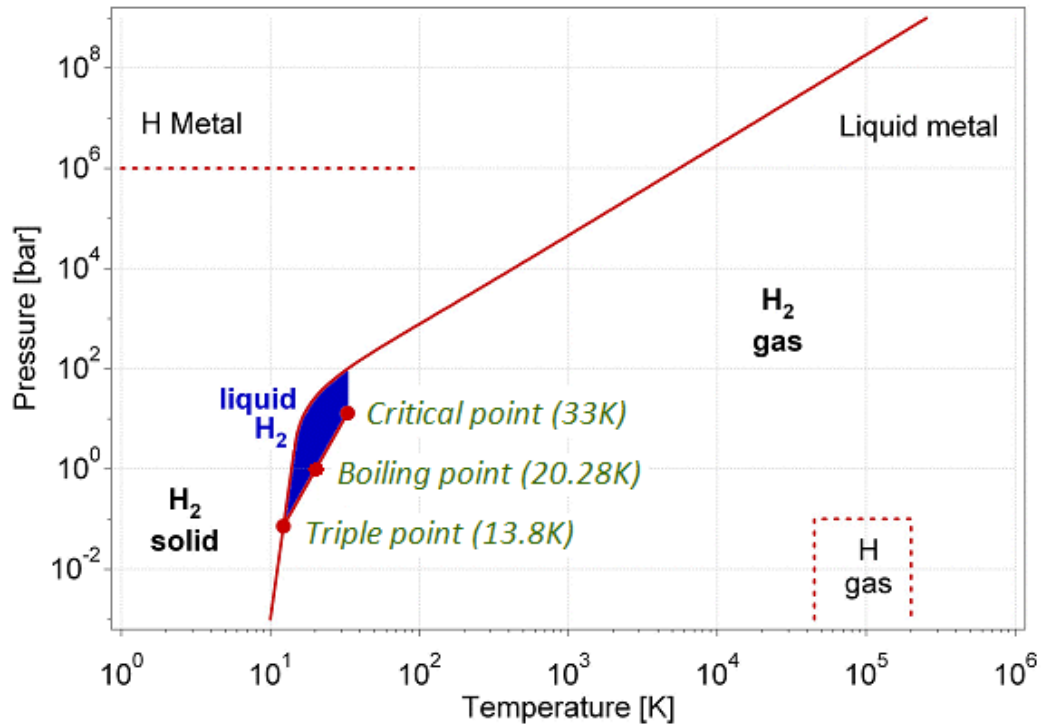


Figure 1.3 Primitive phase diagram for hydrogen. Liquid hydrogen only exists within the blue area which is between 13.8K and 33 K [7, 8]. (With permission from Springer)

For those reasons, hydrogen storage in solid materials is now seen as the safest and most effective way of routinely handling hydrogen for transportation application. Therefore, the emphasis of hydrogen storage was and will be focused on storage in solid materials.

1.3.3 Physical adsorption

Like all other gases, hydrogen will be adsorbed onto solid surfaces via weak Van der Waals force (1-10 kJ/mol H). Because of the weak interaction, thermal energy at room temperature is enough to desorb the majority of hydrogen from the surface. A significant physisorption is only observed at low temperatures (< 273 K). Liquid nitrogen (boiling point 77 K) is often used as coolant to maximize this interaction.

Materials for hydrogen storage via physisorption are typically solids with high surface area such as zeolites [9], activated carbons [10], metal-organic frameworks (MOFs) [11, 12] etc. The amount of adsorbed hydrogen is proportional to the BET surface area (total surface area based on the multipoint Brunauer, Emmett and Teller method) of the materials at low temperature (77 K).

The hydrogen capacity via physical adsorption is low at ambient temperature. The maximum absorption capacity for hydrogen on carbon materials is 2 wt%. The adsorption capacity of zeolites at 77K is typically below 2 wt%. By modifying the organic linkers, the pore size and effective surface area can be tailored quite effectively. For example, hydrogen adsorption capacities of up to 7.5 wt% at 77K have been obtained for MOF-177 [13, 14].

1.3.4 Metal hydrides

Metal hydrides can be generated by the reaction of hydrogen and many metals and alloys at elevated temperature. For some cases, the formation of metal hydrides does not change the original structure of these metals. These hydrides are called interstitial hydrides, e.g. PdH, LaNi_5H_x and $(\text{Vi-Ti-Fe})\text{H}_2$. For other cases, the formation of metal hydrides changes the original metal structure, e.g. MgH_2 and AlH_3 .

For many binary metal hydrides, the thermodynamics of H bonding is either too strong or too weak. For example, the binding energy of AlH_3 is so weak (7.6 kJ/mol H_2 [15]) that it is impossible to generate AlH_3 directly from the reaction of Al and H_2 at moderate pressure. While the binding energy of MgH_2 is so strong (62.3 kJ/mol H_2 [16]) that it needs $\sim 290^\circ\text{C}$ to release hydrogen at 1 atm.

In order to obtain intermediate thermodynamic affinities for hydrogen, Researchers [17, 18] combined strong hydride forming elements A with weak hydride forming elements B to form alloys. Typical alloys for hydrogen storage include AB_5 , AB_2 , AB, and, A_2B . The latter element B is often Ni due to its excellent hydrogen dissociation performance [7]. For example, LaH_2 (binding energy 208 kJ/mol H_2) and NiH (binding energy 8.8 kJ/mol H_2) can form $\text{LaNi}_5\text{H}_{6+}$ (binding energy 30.9 kJ/mol H_2) [19].

Metal hydrides have larger volumetric hydrogen density than hydrogen gas or liquid hydrogen [2]. However, the gravimetric hydrogen density is limited to less than 3 weight % for metal hydrides working around ambient temperature and

atmospheric pressure because they consist of transition metals. Therefore, it is still a challenge to explore metal hydrides for onboard hydrogen storage usage.

1.3.5 Complex hydrides

Group I and II salts of $[\text{AlH}_4]^-$, $[\text{NH}_2]^-$, $[\text{BH}_4]^-$ are referred to as “complex hydrides” because in which hydrogen is covalently bonded to central atoms to form “complex” anions in contrast to interstitial hydrides [20].

Hydrogen storage in light weight complex hydride can meet the DOE gravimetric and volumetric capacities targets. Many complex hydrides even show very high gravimetric and volumetric hydrogen densities. For example, the gravimetric and volumetric hydrogen densities for LiBH_4 are 18.5 wt % and 120 kg/m^3 [21]; for $\text{Al}(\text{BH}_4)_3$ are 17 wt% and 150 kg/m^3 [22]. However, the slow kinetics, high hydrogen release temperature and low charge and discharge rates are still challenges for mobile applications [23]. LiBH_4 and NaBH_4 are most promising candidates among the known borohydrides which can be potentially used for onboard applications due to their high hydrogen densities. Nevertheless, their low dynamics of hydrogen release is still a big problem associated with these systems [23].

Most complex hydrides change their morphology of particles and cannot maintain their original structure after the hydrogen absorption/desorption cycles [24]. Therefore, the reversibility is also a problem.

1.3.6 Clathrate

Recently, hydrogen storage in clathrate hydrogen hydrates was explored [25-30]. Hydrogen storage in this type of material is achieved by capturing hydrogen in H_2O -cages, instead of chemical reaction or physical adsorption. Because the hydrogen hydrates are neither flammable nor corrosive, they provide a safe and environmentally-friendly material to store hydrogen. However, it still remains a challenge to employ hydrogen hydrates as practical hydrogen storage materials. For example, formation of hydrogen hydrate is a slow process. The permanent cooling, which is necessary to keep hydrogen hydrates stable, may be another issue.

1.4 Lithium nitride for hydrogen storage

As early as 1910, Dafert and Miklauz found that Li_3N and H_2 generated Li_3NH_4 at 220-250 °C and Li_3NH_4 can be partially decomposed to release H_2 [31]. The next year, Ruff, H. Goerges identified that Li_3NH_4 is a mixture of LiNH_2 and 2LiH [32]. Consequently, the reversible process of the hydrogenation of Li_3N and the dehydrogenation of the hydrogenated Li_3N can be used for hydrogen storage. Although Li_3N can be used as hydrogen storage material, it did not attract any attention for almost a century. Since 2002, the interests of Li_3N as a hydrogen storage material have been activated [33-51].

The Li-N-H system for hydrogen storage is based on the following hydrogenation and dehydrogenation process [33]:



The enthalpy changes of the dehydrogenation process are shown as follows:



Because further dehydrogenation of $\text{Li}_2\text{NH}/\text{LiH}$ back to Li_3N is difficult (as we can see from the big enthalpy change of Reaction 1.3), the attention was focused on Reaction 1.2 as a reversible process, which provides 6.8 wt % hydrogen storage capacity [52].

Hydrogen absorption and desorption by Li_2NH (Reaction 1.2) was measured with a commercial pressure-composition-temperature (PTC) automatic measuring system [53]. The results are shown in Figure 1.4.

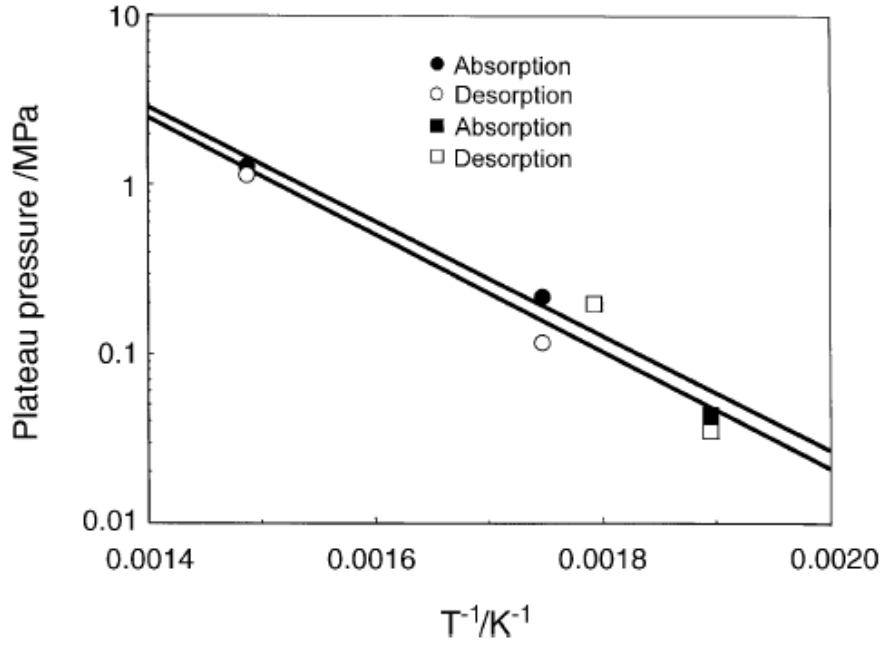


Figure 1.4 Logarithm of dissociation pressure vs. reciprocal of absolute temperature [53]. (With permission from Elsevier)

The equations of hydrogen absorption and desorption based on Figure 1.4 are [53]:

$$\ln P = -\frac{7760}{T} + 14.2 \text{ (absorption)} \quad (1.4)$$

$$\ln P = -\frac{8010}{T} + 14.4 \text{ (desorption)} \quad (1.5)$$

Assuming that H_2 absorption and desorption reaction paths are the same, by averaging Equation (1.4) and (1.5), we can get:

$$\ln P = -\frac{7885}{T} + 14.3 \quad (1.6)$$

Through Equation (1.6), we can calculate the enthalpy and entropy change of Reaction (1.2): $\Delta H = 65.6 \text{ kJ/mol H}_2$ and $\Delta S = 119 \text{ J/mol H}_2 \cdot \text{K}$. The value of enthalpy obtained by this experiment is different from the one by theoretical calculation $\Delta H = 44.63 \text{ kJ/mol H}_2$ probably because the errors of each method.

By Equation (1.6), we can draw a plot of the equilibrium hydrogen pressure and reaction temperature of the hydrogenation and dehydrogenation of $\text{Li}_2\text{NH/LiH}$ system (Reaction 1.2) as shown in Figure 1.5.

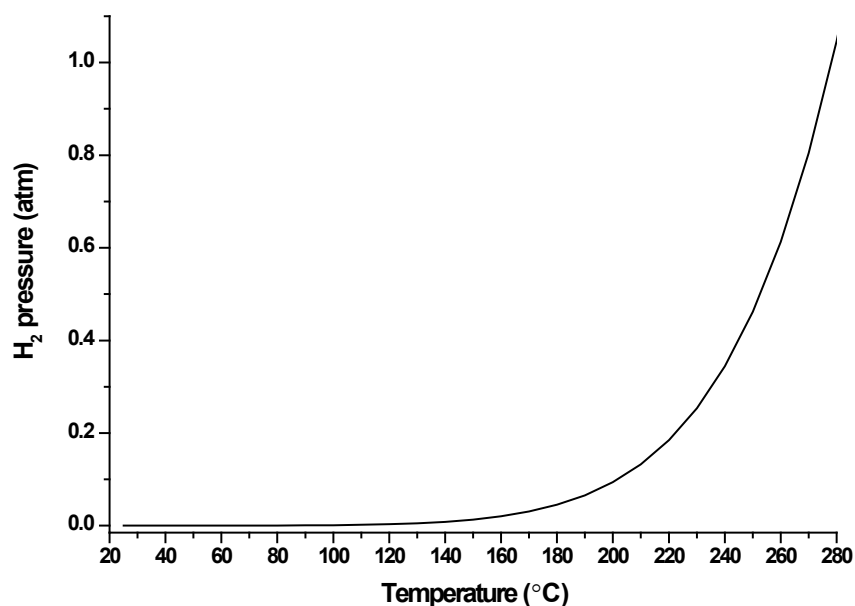


Figure 1.5 Equilibrium hydrogen pressure and reaction temperature of Reaction (1.2).

From Figure 1.5 we know that when the combination of hydrogen pressure and reaction temperature is below the curve, the equilibrium of Reaction (1.2) will

move forward, namely, the dehydrogenation is feasible. In contrast, when the combination of hydrogen pressure and reaction temperature is above the curve, the equilibrium of Reaction (1.2) will move backward, namely, the hydrogenation is feasible.

1.5 Lithium nitride crystal structure and optical property

1.5.1 Crystal structure

Li_3N is the only stable alkali metal nitride [54-56]. The commercial Li_3N used was a two-phase mixture of $\alpha\text{-Li}_3\text{N}$ and $\beta\text{-Li}_3\text{N}$. $\alpha\text{-Li}_3\text{N}$ can be prepared by direct combination of elemental lithium with nitrogen gas at 400 °C [57]. Its structure was first evaluated by Zintl and Brauer [58] and later revised by Rabenau and Schulz [59]. They revealed that the structure of α phase is hexagonal with P6/mmm space group and lattice constants $a = 3.648(1) \text{ \AA}$ and $c = 3.875(1) \text{ \AA}$ ($Z = 1$) [59, 60]. $\alpha\text{-Li}_3\text{N}$ crystal structure consists of two types of layers: in the Li_2N^- layers, the lithium atoms Li(1) are arranged in a graphite like structure with the nitrogen atoms at the center of the hexagons; in the pure lithium layers, the pure Li(2) are on the top of the nitrogen atoms. $\alpha\text{-Li}_3\text{N}$ is known to have an exceptionally large Li ionic conductivity [61-65]. Its conductivity is caused by intrinsic defects (1-2% Li vacancies) in the $\alpha\text{-Li}_2\text{N}$ layers [66]. Due to the defects within the Li_2N layers, the structure of $\alpha\text{-Li}_3\text{N}$ is packed loosely, and consequently it could be expected to

undergo a pressure-induced phase transformation. Indeed, β -Li₃N can be produced by the pressure (~ 0.5 GPa) induced phase transformation of α -Li₃N [67, 68]. This phase possesses a hexagonal structure in the $P6_3/mmc$ space group with $a = 3.552(1)$ Å and $c = 6.311(3)$ Å ($Z = 2$) [69] in which pure-lithium layers alternate LiN layers as opposed to the Li₂N layers in α phase.

Since the phase transformation from α -Li₃N to β -Li₃N takes place at the relatively low pressure of 0.5 GPa, it can hardly be ruled out that at least a partial β -Li₃N can be formed by grinding α -Li₃N in a mortar [69]. Mechanically ball milling commercial Li₃N can also transform α -Li₃N to β -Li₃N due to the high pressure produced by the strong striking between the ball and the jar wall [70]. Heat treatment ($\sim 500^\circ\text{C}$) of β -Li₃N can lead the phase transformation of β -Li₃N back to α -Li₃N [70, 71]. The β -Li₃N phase remains stable up to 35 GPa.

The third solid phase of Li₃N, γ -Li₃N, exist at ultra high pressure. Theoretical calculations predicted the phase transformation from β -Li₃N to a cubic structure — $P\bar{4}3m$ at 37.9 GPa [72] or $Fm\bar{3}m$ at 27.6 ± 5.4 GPa [68] — γ -Li₃N. Furthermore, experimental evidence showed that β -Li₃N indeed transforms to a cubic structure (γ -Li₃N) in the pressure range of 36-45 GPa [73]. γ -Li₃N possesses a FCC structure in the $Fm\bar{3}m$ space group with $a = 4.976$ Å and remains stable up to 200 GPa [73].

1.5.2 Optical property

The electronic structure and energy gap of Li_3N have been evaluated experimentally [71, 74, 75] and theoretically [76-82]. Brendecke and Bludau investigated the optical absorption of single crystal $\alpha\text{-Li}_3\text{N}$ with incident light perpendicular and parallel to the c-direction [74, 75]. Their results showed $\alpha\text{-Li}_3\text{N}$ with anisotropic behavior of optical absorption: $E_{//c}=2.15$ eV at 4.2 K, $E_{//c}=2.00$ eV at 300 K, and $E_{\perp c}=2.18$ eV at 4.2 K [74]. Our research group evaluated the optical properties of α and β Li_3N by ultraviolet-visible (UV-vis) absorption method and found that the energy gap of α and β Li_3N are 1.81 ± 0.01 and 2.14 ± 0.01 eV, respectively [71]. In addition, ab initio calculations were employed to evaluate the band structure of Li_3N . Kerker's self-consistent electronic structure calculation for $\alpha\text{-Li}_3\text{N}$ predicted that the energy gap between the occupied valence band and the lowest excited band is 1 eV [76]. Cui et al. carried out density functional calculations with the plane wave pseudopotential method, predicting that the energy gap of $\alpha\text{-Li}_3\text{N}$ is 1.32 eV at pressure of 0 GPa [81]. This value is close to Kerker's result [76]. However, both of these theoretical values are smaller than the experimental ones: 2.2 eV by Brendecke and Bludau [74, 75] and 1.81 ± 0.01 eV by our group [71]. This discrepancy between theory and experiment is often observed for band-structure calculations of semiconductors [83]. Lazicki et al. performed first-principles electronic structure calculations and predicted that the energy gap of $\beta\text{-Li}_3\text{N}$ is 1.5 eV [78]. This predicted value is smaller than our experimental value (2.14 ± 0.01 eV). This happened because theoretical calculations usually underestimate energy gaps of

semi-conductors [76, 82]. The energy gap of γ -Li₃N was predicted to be 5.5 eV by Lazicki et al. [78] and 5.68 eV by Cui et al. [81]. The big increase of the energy gap of the phase change from β -Li₃N to γ -Li₃N is in accordance with the optical change from the opaque β to the transparent γ phase [73].

1.6 Lithium nitride halides structure and properties

Lithium nitride halides Li_{3-2y}N_{1-y}X_y (X=Cl, Br, I; 0<y<1) compounds were first reported by Sattlegger and Hahn in 1964 [84, 85] and were subsequently studied widely [85-101]. Generally, the crystal structures of Li_{3-2y}N_{1-y}X_y (X=Cl, Br, I; 0<y<1) can be understood as products of the reaction between α -Li₃N and LiX (X=Cl, Br) in which the framework structure of α -Li₃N is broken down into units of lower dimensionality [102]. Li₉N₂Cl₃ (2Li₃N: 3LiCl) possesses an anti-fluorite type structure with 10% of the lithium sites are vacancies, while the anion sites are almost completely randomly occupied by N and Cl [90]. It shows more clearly by using formula (Li_{0.9}□_{0.1})₂(N_{0.4}Cl_{0.6}) comparing with Li₂O in which the sites are almost fully occupied [103]. The more vacancies of the Li sites of Li₉N₂Cl₃ than that of Li₂O makes Li₉N₂Cl₃ a better ionic conductor than Li₂O [103]. The ternary compounds Li₁₁N₃Cl₂ and Li₉N₂Cl₃ melt congruently at 705 °C and 710 °C respectively [88]. The incongruent melting points of compounds Li₁₃N₄Br, Li₉N₂Br₃ and Li₆NBr₃ decrease with increasing lithium bromide content: 600 °C for Li₁₃N₄Br, 510 °C for Li₉N₂Br₃ and 484 °C for Li₆NBr₃ [88]. Compound Li_{3x+1}N_xI

($1.89 \leq x \leq 2.76$) shows the maximum congruent melting point of 775 °C while Li_5NI_2 melts congruently at 573 °C [88]. Lithium nitride halides have been proposed as solid electrolytes in practical battery applications due to their high Li^+ ion conductivity, negligible electronic conduction, and high enough thermodynamic decomposition voltage [87, 89].

Of all the lithium nitride halides $\text{Li}_{3-2y}\text{N}_{1-y}\text{X}_y$ ($\text{X}=\text{Cl}, \text{Br}, \text{I}; 0 < y < 1$) stable compounds, $\text{Li}_{13}\text{N}_4\text{Br}$ shows the highest Li_3N to LiX ($\text{X}=\text{Cl}, \text{Br}, \text{I}$) molar ratio. $\text{Li}_{13}\text{N}_4\text{Br}$ was prepared by annealing of the two binary compounds Li_3N and LiBr in the molar ratio of 4:1 at 400 °C for about 20 hours [86]. It was found that $\text{Li}_{13}\text{N}_4\text{Br}$ has a hexagonal symmetry with $a = 7.417(1) \text{ \AA}$ and $c = 3.865(1) \text{ \AA}$ [88]. $\text{Li}_{13}\text{N}_4\text{Br}$ shows a phase transition at about 230 °C with a small enthalpy change of 0.927 kJ/mol [88]. The ionic conductivities of $\text{Li}_{13}\text{N}_4\text{Br}$ at 150 and 300 °C are $3.5 \times 10^{-6} \Omega^{-1}\text{cm}^{-1}$ and $1.4 \times 10^{-3} \Omega^{-1}\text{cm}^{-1}$, respectively; the electronic conductivity of $\text{Li}_{13}\text{N}_4\text{Br}$ is negligible [90].

1.7 Scope of this study

Lithium nitride is an important material which can be used for hydrogen storage. The decompositions of lithium amide and lithium imide are important steps for hydrogen storage in Li_3N . As far as our knowledge, the effect of anions (e.g. halide ions) on the decomposition have never been studied.

Lithium nitride is also an important material which can be used for CO₂ conversion, and electric charge storage. Lithium nitride halides are also significant materials which can be potentially used for batteries. Therefore, the chemical stability of lithium nitride and lithium nitride halides in air is very important for guiding how to deal with them while being used. As far as our knowledge, the chemical stability of lithium nitride and lithium nitride halides in air has never been studied.

Therefore, the objectives of this dissertation are to (1) evaluate the mechanism of the decomposition of lithium amide; (2) evaluate the mechanism of the decomposition of lithium imide; (3) examine the effect of anion promoter Cl⁻ on the decomposition of lithium amide; (4) investigate the chemical stability of lithium nitride in air; and (5) investigate the chemical stability of lithium nitride halide Li₁₃N₄Br in air.

Chapter 2 Decomposition of lithium amide *

2.1 Introduction

Since 2002, Li_3N has attracted much attention for hydrogen storage [33-51], which is based on the following hydrogenation and dehydrogenation [34]:



Because further dehydrogenation of $\text{Li}_2\text{NH}/\text{LiH}$ back to Li_3N (the reverse direction of Reaction 2.1) is difficult, the attention was focused on Reaction 2.2 as a reversible process, which provides 6.8 wt % hydrogen storage capacity [52]. The dehydrogenation mechanism of LiNH_2/LiH (Reaction 2.2) consists of two elementary steps with NH_3 as intermediate species (Reaction 2.3 and Reaction 2.4) [34].



The reaction between NH_3 and LiH (Reaction 2.4) is exothermic and ultra fast [34].

The decomposition of LiNH_2 (Reaction 2.3) is the rate-determining step.

*The material contained in this chapter was previously published in the journal *Industrial and Engineering Chemistry Research* 2011, 50 (13), 8058-8064 by Junqing Zhang and Yun Hang Hu. See Appendix for documentation of permission to republish this material.

We hypothesize that a new compound $\text{Li}_{1.5}\text{NH}_{1.5}$ may form during the decomposition of LiNH_2 . It is demonstrated through structural refinement from synchrotron X-ray diffraction that the mechanism of the transformation between LiNH_2 and Li_2NH during hydrogen cycling ($\text{Li}_3\text{N} + 2\text{H}_2 \leftrightarrow \text{Li}_2\text{NH} + \text{LiH} + \text{H}_2 \leftrightarrow \text{LiNH}_2 + 2\text{LiH}$) occurs in a non-stoichiometric manner [104]. This means the formation of any intermediate species $\text{Li}_{1+x}\text{NH}_{2-x}$ ($0 < x < 1$) between LiNH_2 and Li_2NH is possible. Furthermore, density functional theory calculations predict that $\text{Li}_{1.5}\text{NH}_{1.5}$ is the most stable transition state between LiNH_2 and Li_2NH [105]. Therefore, it is reasonable for us to expect that the decomposition of LiNH_2 to Li_2NH is via the intermediate compound $\text{Li}_{1.5}\text{NH}_{1.5}$.

In this chapter, the systematical evaluation for the decompositions of LiNH_2 was carried out. We evaluate how lithium amide (LiNH_2) decomposes and what intermediate species are formed during the decomposition by temperature-programmed decomposition and X-ray diffraction (XRD) techniques.

2.2 Experiments

2.2.1 Sample preparations

Lithium amide (LiNH_2) powder (95%) which had been purchased from Sigma-Aldrich Chemical Co. was used without any further purification.

2.2.2 Temperature-programmed decomposition

The temperature-programmed decomposition (TPD) experiments were performed as follows: A sample was loaded into a vertical quartz tube reactor, which was located in an electric tube furnace. The temperature of the reactor was increased to 850 °C at a rate of 5 °C/min. Argon (30 mL/min) was employed as a carrier gas through the reactor to bring the gaseous products of the decomposition of the sample into a thermal conductivity detector (TCD, Figure 2.1) of Varian 3300 Gas Chromatograph, generating a TPD-TCD profile. Thermal conductivity is the property of a material to conduct heat.



Figure 2.1 Thermal conductivity detector of Varian 3300 Gas Chromatograph.

Furthermore, to determine all gas products except hydrogen, helium was used to carry the products from the TPD reactor into a mass spectrometer (HP 5970 series mass selective detector, Figure 2.2) instead of TCD detector, generating a TPD-MS profile. The masses from 16.7 to 17.7 were used to monitor NH_3 and from 27.7 to 28.7 to detect N_2 .



Figure 2.2 HP 5970 series mass selective detector.

2.2.3 X-ray diffraction (XRD)

A sample (0.1 g) was loaded into a vertical quartz tube reactor (5-mm diameter) located in an electric tube furnace. Argon (30 mL/min) was introduced into the reactor at room temperature, followed by heating to a selected temperature at a rate of 5 °C/min and then cooling down to room temperature. The obtained samples were subjected to XRD measurements, which were performed with a Scintag

XDS2000 Powder Diffractometer equipped with a Cu K α source, at 45 kV and 35 mA (Figure 2.3). The scanning speed was 1°/min. Samples were covered with plastic wrap during the XRD measurements to prevent from absorbing H₂O in air.



Figure 2.3 Scintag XDS2000 Powder Diffractometer.

2.3 Results and discussion

It is well-known that the decomposition of LiNH₂ can produce Li₂NH and NH₃ [106, 107]. However, the answers for the two questions are still unknown: whether hydrogen is formed during the decomposition of LiNH₂ and how Li₂NH

further decomposes. To clarify them, LiNH_2 was subjected to temperature-programmed decompositions (TPD) with TCD and MS detectors.

As shown in Figure 2.4, one can see that the TPD-TCD and TPD-MS profiles are very similar. Furthermore, the TPD-MS profile showed that NH_3 was formed in the temperature range of 160-470 °C and N_2 produced between 550 and 800 °C. However, hydrogen cannot be detected by the MS detector due to the limitation of the MS instrument. In contrast, the TPD-TCD provides total signals of all gases due to their different thermal conductivities from the carrier gas (Argon). In other words, all three possible gas products (H_2 , NH_3 , and N_2) can contribute to the peaks in the TPD-TCD profile. To clarify whether the peaks between 200 and 500 °C are associated with hydrogen, the gas products from the temperature-programmed decomposition of LiNH_2 were cooled to 159K before entering a TCD or MS detector. As a result, the peaks between 200 and 500 °C disappeared (Figure 2.5). The boiling temperatures of H_2 (20.28 K) and N_2 (77.36 K) are lower than the cooling temperature (159 K), whereas the melting temperature of NH_3 (195 K) is higher than the cooling temperature. Therefore, the disappearance of the peak between 200 °C and 500 °C should be due to the condensation of NH_3 . A small bump between 200 and 500 °C can be observed in Figure 2.5a. The further analysis of a gas chromatography (GC) equipped with TCD detector and a Porapak Q column revealed that the small bump is due to small amount of H_2 and N_2 . In other words, the peaks at 330 °C in Figure 2.4a consist of mainly NH_3 with a very little amount of H_2 and N_2 . Such a negligible amount of N_2 and H_2 may be due to the decomposition

of NH_3 .

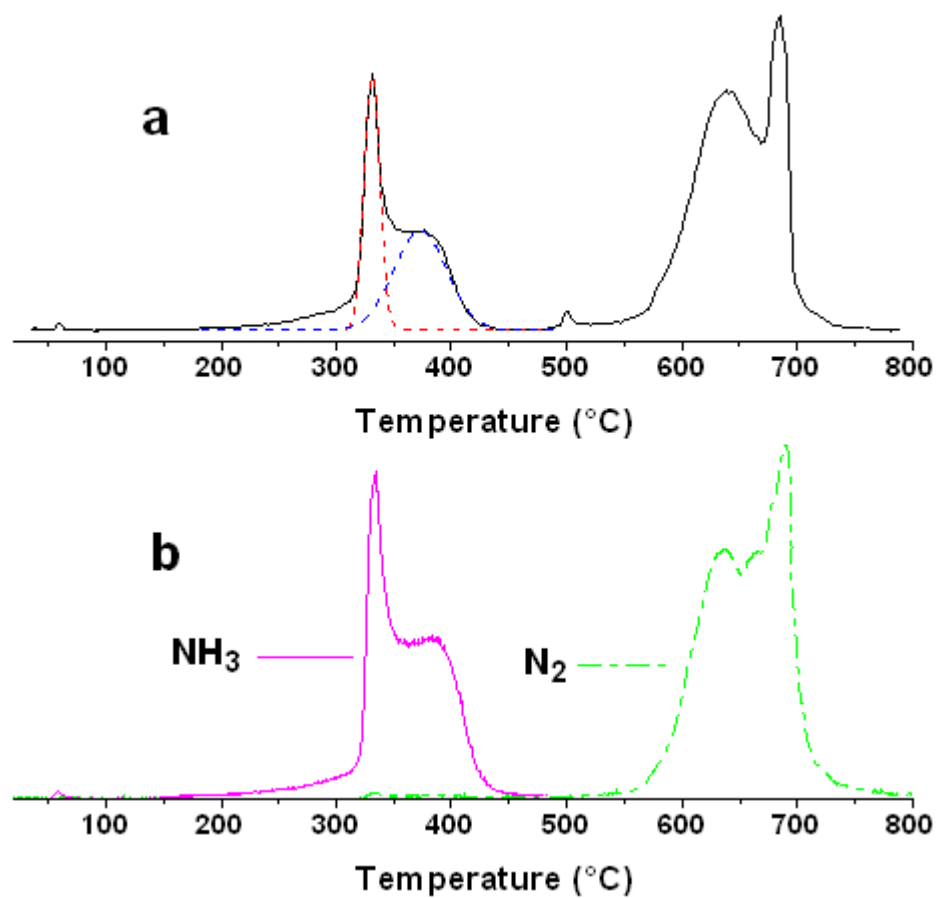


Figure 2.4 (a)TPD-TCD profile and (b) TPD-MS profile of pure LiNH_2 .

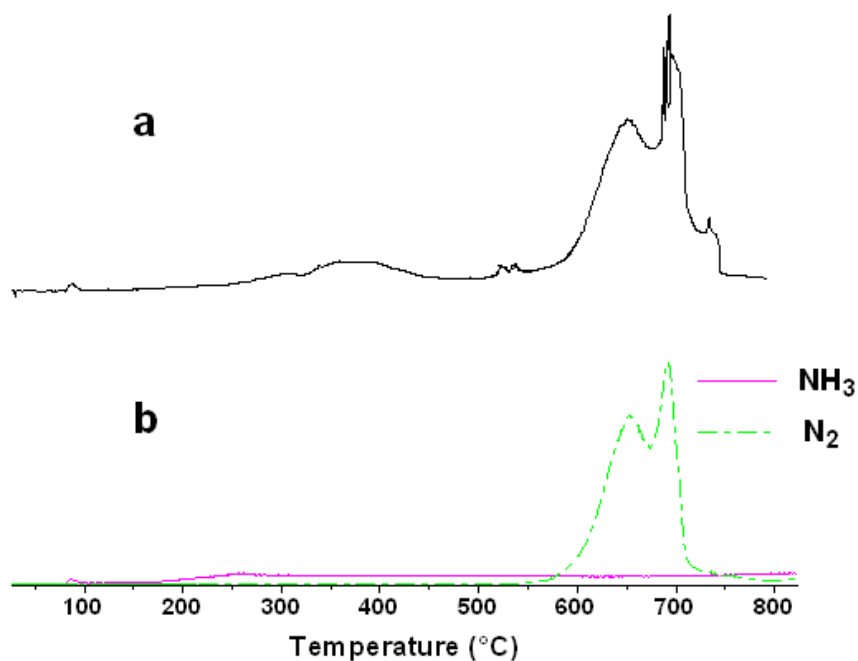


Figure 2.5 (a) TPD-TCD profile and (b) TPD-MS profile of LiNH_2 with a cooler where produced gases were cooled to 159K before entering TCD and MS detectors.

Furthermore, the solid products from the TPD process were analyzed by XRD. As shown in Figure 2.6, one can see that the solid product obtained after the decomposition of LiNH_2 at 330 $^{\circ}\text{C}$ or above was Li_2NH . This indicates that the decomposition of LiNH_2 produced NH_3 and Li_2NH between 200 and 500 $^{\circ}\text{C}$, which can be expressed by Equation 2.3.

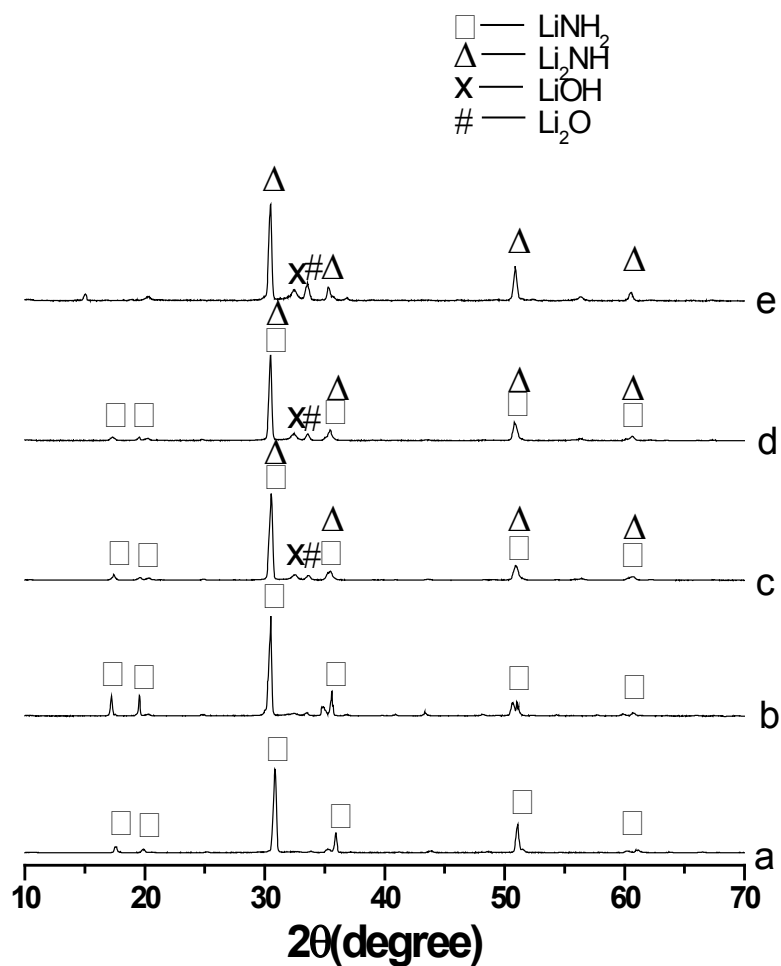
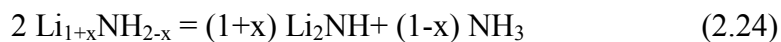
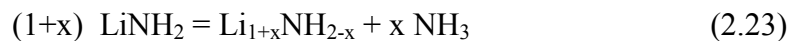


Figure 2.6 XRD patterns of the solid products from the TPD process of LiNH_2 that was stopped at (a) room temperature, (b) 160 °C, (c) 330 °C, (d) 380 °C, and (e) 520 °C.

However, the decomposition process is not a single step, because there were two peaks (one at 330 °C and the other at 380 °C) between 200 and 500 °C in the TPD profiles (Figure 2.4). This means that the two steps were involved in the decomposition of LiNH_2 into Li_2NH and NH_3 . In other words, a stable intermediate

species $\text{Li}_{1+x}\text{NH}_{2-x}$ ($0 < x < 1$), which is between LiNH_2 and Li_2NH , was formed as follows:



The ratio of x to $(1-x)/2$ equals to the ratio of the areas of peak 1 (at 330 °C, corresponding to reaction 2.23) to peak 2 (at 380 °C, corresponding to reaction 2.24). The value (0.5) of x was obtained from the TPD profiles (overlapped peaks in Figure 2.4a were resolved by Gaussian function fitting to obtain their areas). Therefore, the intermediate species in the decomposition of LiNH_2 is $\text{Li}_{1.5}\text{NH}_{1.5}$.

During the hydrogenation of Li_3N , Weidner et al. detected a series of non-stoichiometric lithium imides [108], in which compositions can be changed from $\text{Li}_{1.70}\text{NH}_{1.30}$ to $\text{Li}_{1.02}\text{NH}_{1.98}$ [104, 109]. This would be dependent on the unique structure of Li_2NH . Juza et al. first reported that the crystal structure of lithium imide (Li_2NH) is an anti-fluorite face centered cubic (fcc) structure [106]. Recently, Ohoyama et al. performed neutron powder diffraction experiments on Li_2NH [110]. They confirmed the fcc structure. However, they refined the positions of hydrogen atoms, because there is not any fully occupied model representing experimental data. They found two partially occupied models that can explain the experimental data: Model I, in which every hydrogen is located at the 48h site of the $\text{Fm}\bar{3}\text{m}$ space group and the site occupancy of hydrogen is only 8.7%, and Model II, in which every

hydrogen is located at the 16e site of the $F\bar{4}3m$ space group and the site occupancy of hydrogen is 27%. Furthermore, Noritake et al. [111] carried out synchrotron X-ray powder diffraction experiments and charge density analysis for the same sample as Ohoyama et al. used. They also confirmed the anti-fluorite structure. Based on the Rietveld analysis accomplished for various structure models on the expected hydrogen sites around N atom, they revealed that both the structure model with hydrogen located at the 48h of the $Fm\bar{3}m$ space group and the model with hydrogen located at the 96j site of the $Fm\bar{3}m$ space group can well match their experimental data. Other models were also proposed [112-115]. Although those models have some differences, they reached the same conclusion that sites for N and Li are fully occupied but sites for H only partially occupied. Each H atom randomly occupies the hydrogen sites around each N. In other words, the crystal structure of Li_2NH is hydrogen disordered structure, which has huge number of unoccupied hydrogen sites. As a result, hydrogen can be introduced into the unoccupied hydrogen sites around N in stoichiometric lithium imide (Li_2NH) to form a series of non-stoichiometric intermediate species between $LiNH_2$ and Li_2NH . This can explain why the stable intermediate species ($Li_{1.5}NH_{1.5}$) was observed during the thermal decomposition of $LiNH_2$. Furthermore, very recently, Crivello et al. reported density functional theory calculations for intermediate Li-N-H compounds [105]. Their results showed that the formation of the intermediate $Li_{1.5}NH_{1.5}$ is possible and it should occupy a cubic Li-vacant-type structure, in which ordered $[NH]^{2-}$ and $[NH_2]^-$ anions coexist. Therefore,

our detected stable intermediate $\text{Li}_{1.5}\text{NH}_{1.5}$ compound is consistent with the DFT prediction.

2.4 Conclusion

The decomposition of LiNH_2 was evaluated. It was found that the decomposition of LiNH_2 produced Li_2NH and NH_3 via two-steps: LiNH_2 into a stable intermediate species ($\text{Li}_{1.5}\text{NH}_{1.5}$) and then into Li_2NH . This proved that the hypothesis a new compound $\text{Li}_{1.5}\text{NH}_{1.5}$ may form during the decomposition of LiNH_2 is true.

Chapter 3 Decomposition of lithium imide *

3.1 Introduction

Li_2NH is a promising material for hydrogen storage with 6.8 % reversible capacity [52]. However, the decomposition of lithium imide (Li_2NH) has not been investigated. This prompts us to evaluate how Li_2NH decomposes and what intermediate species is formed during the decomposition by temperature-programmed decomposition and X-ray diffraction (XRD) techniques as well as kinetic analysis.

Li_4NH , which is a stable compound, has been synthesized by the reaction of LiNH_2 and Li_3N in liquid Li in the presence of Fe at 747 °C followed by slow cooling to 27 °C within 20 h [116], or by the reaction of Li_3N and LiH at 490 °C [117]. We hypothesize that Li_4NH may be an intermediate compound during the decomposition of Li_2NH .

*The material contained in this chapter was previously published in the journal *International Journal of Hydrogen Energy* 2012, 37 (13), 10467-10472 by Junqing Zhang and Yun Hang Hu. See Appendix for documentation of permission to republish this material.

3.2 Experiments and kinetic calculation method

3.2.1 Sample preparations

Lithium amide (LiNH_2) powder (95%) and lithium nitride Li_3N powder ($\geq 99.5\%$) which had been purchased from Sigma-Aldrich Chemical Co. were used without any further purification. Lithium imide (Li_2NH) was prepared with thermal decomposition method: LiNH_2 was located in a stainless steel tube reactor at room temperature under argon (30 mL/min) flow, followed by increasing temperature to 500 °C at a rate of 5 °C/min.

3.2.2 Temperature-programmed decomposition

5.5 mg Li_2NH or 10 mg Li_3N was loaded into a stainless steel tube reactor, which was located in an electric tube furnace. The temperature of the reactor was increased to 850 °C at a rate of 5 °C/min from room temperature. Argon (30 mL/min) was employed as a carrier gas through the reactor to bring the gaseous products of the decomposition into a thermal conductivity detector (TCD, Figure 2.1), generating a TPD profile.

Furthermore, to determine all gas products except hydrogen, helium was used to carry the products from the TPD reactor into a mass spectrometer (HP Quadrupole, 5970 series mass selective detector, Figure 2.2) instead of TCD detector, generating

a TPD-MS profile. The masses from 16.7 to 17.7 were used to monitor NH_3 and from 27.7 to 28.7 to detect N_2 .

3.2.3 X-ray diffraction (XRD)

0.1 g Li_2NH was loaded into a stainless steel tube reactor (5-mm diameter) located in an electric tube furnace. Argon (30 mL/min) was introduced into the reactor at room temperature, followed by heating to a selected temperature at a rate of 5 °C/min and then cooling down to room temperature. The obtained samples were subjected to XRD measurements, which were performed with a Scintag XDS2000 Powder Diffractometer equipped with a $\text{Cu K}\alpha$ source, at 45 kV and 35 mA (Figure 2.3). The scanning speed was 1°/min. Samples were covered with plastic wrap during the XRD measurements to prevent from absorbing H_2O in air.

3.2.4 Kinetic calculation method for TPD-TCD peaks

Assuming temperature-programmed decomposition of a sample generate gas (gases) which is (are) uniform during the whole decomposition process. If TPD-TCD of the sample is taken, a peak signal will be generated recoding the decomposition process. A typical TPD-TCD profile is shown in Figure 3.1.

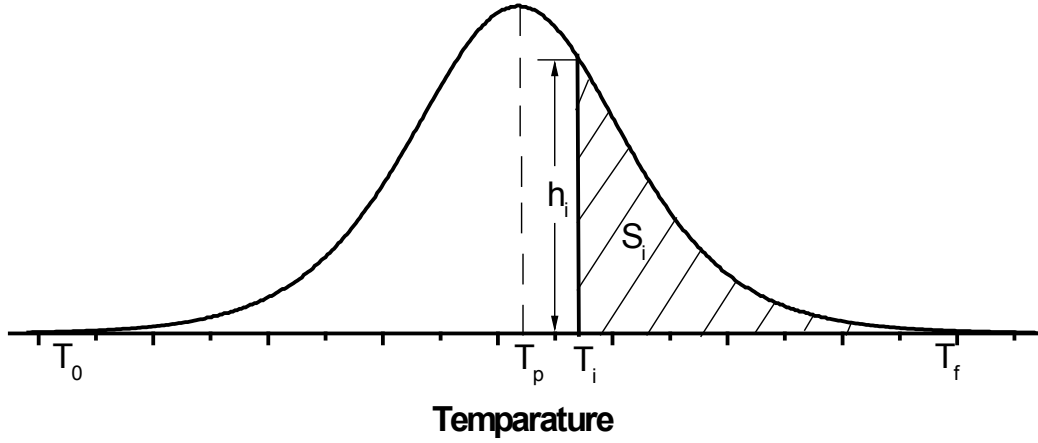


Figure 3.1 Typical TPD-TCD profile of a sample with a uniform gas product.

According to Polangi-Wagner model [118],

$$-\frac{dN}{dt} = A \exp\left(-\frac{E_a}{RT}\right) N^n \quad (3.5)$$

where N is the amount of sample (mg) before decomposition; t the reaction time, A the pre-exponential factor, E_a the decomposition activation energy, n the decomposition order, R the gas constant, and T the absolute temperature.

When temperature increases linearly with time,

$$T = T_0 + \beta t \quad (3.6)$$

where T_0 is initial decomposition temperature and β heating rate. From Equation 3.6, one can obtain

$$dt = \frac{dT}{\beta} \quad (3.7)$$

Because the amount of sample is proportional to the area of the peak,

$$N = aS_i \quad (3.8)$$

where a is the proportionality constant and S_i the area of the peak from T_i to T_f (where T_f is the ending temperature of the peak)

The combination of Equation 3.5 with Equations 3.7 and 3.8 gives

$$-\frac{dS_i}{dT} = \frac{Aa^{n-1}}{\beta} \exp\left(-\frac{E_a}{RT}\right) S_i^n \quad (3.9)$$

Because

$$S_i = \int_{T_i}^{T_f} h_i dT \quad (3.10)$$

where h_i is the height of the curve at any specified temperature T_i ,

$$h_i = -\frac{dS_i}{dT} \quad (3.11)$$

Combining Equations 3.9 and 3.11 provides

$$h_i = \frac{Aa^{n-1}}{\beta} \exp\left(-\frac{E_a}{RT}\right) S_i^n \quad (3.12)$$

At the highest point of the peak,

$$\frac{dh_i}{dT} = \left[\frac{Aa^{n-1}}{\beta} \exp\left(-\frac{E_a}{RT}\right) \right] \left(\frac{E_a}{RT^2} S_i^n + nS_i^{n-1} \frac{dS_i}{dT} \right) = 0 \quad (3.13)$$

Thus,

$$\frac{E_a}{RT_p^2} S_p + n \left(\frac{dS_i}{dT} \right)_{T=T_p} = 0 \quad (3.14)$$

Where T_p is temperature at the highest point of the peak and S_p the area of the peak from T_p to T_f .

Introduction of Equation 3.11 into Equation 3.14 produces

$$n = \frac{S_p E_a}{h_p R T_p^2} \quad (3.15)$$

where h_p is the peak height at the maximum point of the peak.

The rearrangement of Equation (3.12) provides

$$\ln h_i = \ln \left(\frac{A a^{n-1}}{\beta} \right) - \frac{E_a}{RT} + n \ln S_i \quad (3.16)$$

The combination of Equations 3.15 and 3.16 provides

$$\ln h_i = \ln \left(\frac{A a^{n-1}}{\beta} \right) - \frac{E_a}{R} \left(\frac{1}{T_i} - \frac{S_p \ln S_i}{h_p T_p^2} \right) \quad (3.17)$$

Equation 3.17 indicates a linear relationship between $\left(\frac{1}{T_i} - \frac{S_p \ln S_i}{h_p T_p^2} \right)$ and $\ln h_i$,

which has $-\frac{E_a}{R}$ as slope and $\ln \left(\frac{A a^{n-1}}{\beta} \right)$ as intersection. This equation can allow ones to calculate the kinetic parameters including E_a , n , and A .

According to Equation (3.9),

$$-\frac{dS_i}{S_i^n} = \frac{A a^{n-1}}{\beta} \exp \left(-\frac{E_a}{RT} \right) dT \quad (3.18)$$

Integration of Equation 3.18 gives

$$\int_{S_{T_0}}^S -S^{-n} dS = \int_{T_0}^T \frac{A a^{n-1}}{\beta} \exp \left(-\frac{E_a}{RT} \right) dT \quad (3.19)$$

Thus,

$$S^{1-n} = S_{T_0}^{1-n} - (1-n) \int_{T_0}^T \frac{A a^{n-1}}{\beta} \exp \left(-\frac{E_a}{RT} \right) dT \quad (3.20)$$

Rearrangement of Equation 3.20 gives

$$\ln S = \frac{1}{1-n} \ln[S_{T_0}^{1-n} - (1-n) \int_{T_0}^T \frac{Aa^{n-1}}{\beta} \exp\left(-\frac{E_a}{RT}\right) dT] \quad (3.21)$$

Equations 3.17 and 3.21 are combined as

$$\ln h_i = \ln \left(\frac{Aa^{n-1}}{\beta} \right) - \frac{E_a}{R} \left\{ \frac{1}{T_i} - \frac{S_p}{(1-n)h_p T_p^2} \ln[S_{T_0}^{1-n} - (1-n) \int_{T_0}^{T_i} \frac{Aa^{n-1}}{\beta} \exp\left(-\frac{E_a}{RT_i}\right) dT_i] \right\} \quad (3.22)$$

According to Equation 3.22 with obtained E_a , n , and A , one can draw the entire peak.

3.3 Results and discussion

The decomposition of Li_2NH was evaluated by TPD technique. As shown in Figure 3.2, one can see that Li_2NH started to decompose at 550 °C and finished at 800 °C. Because the TPD-TCD provides only total signals of all gases due to their different thermal conductivities from the carrier gas (Argon), the composition of the product gases during the TPD process was analyzed by a gas chromatography (GC) equipped with TCD detector and a Porapak Q column for each 2 min. One can see from Table 3.1 that the peaks consisted of H_2 and N_2 with almost 1:1 molar ratio in the entire temperature range of the two peaks. Although Li is too reactive to be detected by XRD before it transferred into Li_2O and LiOH during its relocation from the reactor to the XRD instrument, we did see shiny matter attached to the inner wall

of the quartz tube reactor after LiNH_2 decomposition at 850°C , indicating the formation of Li. Therefore, the complete decomposition of Li_2NH produced Li, H_2 , and N_2 as follows:



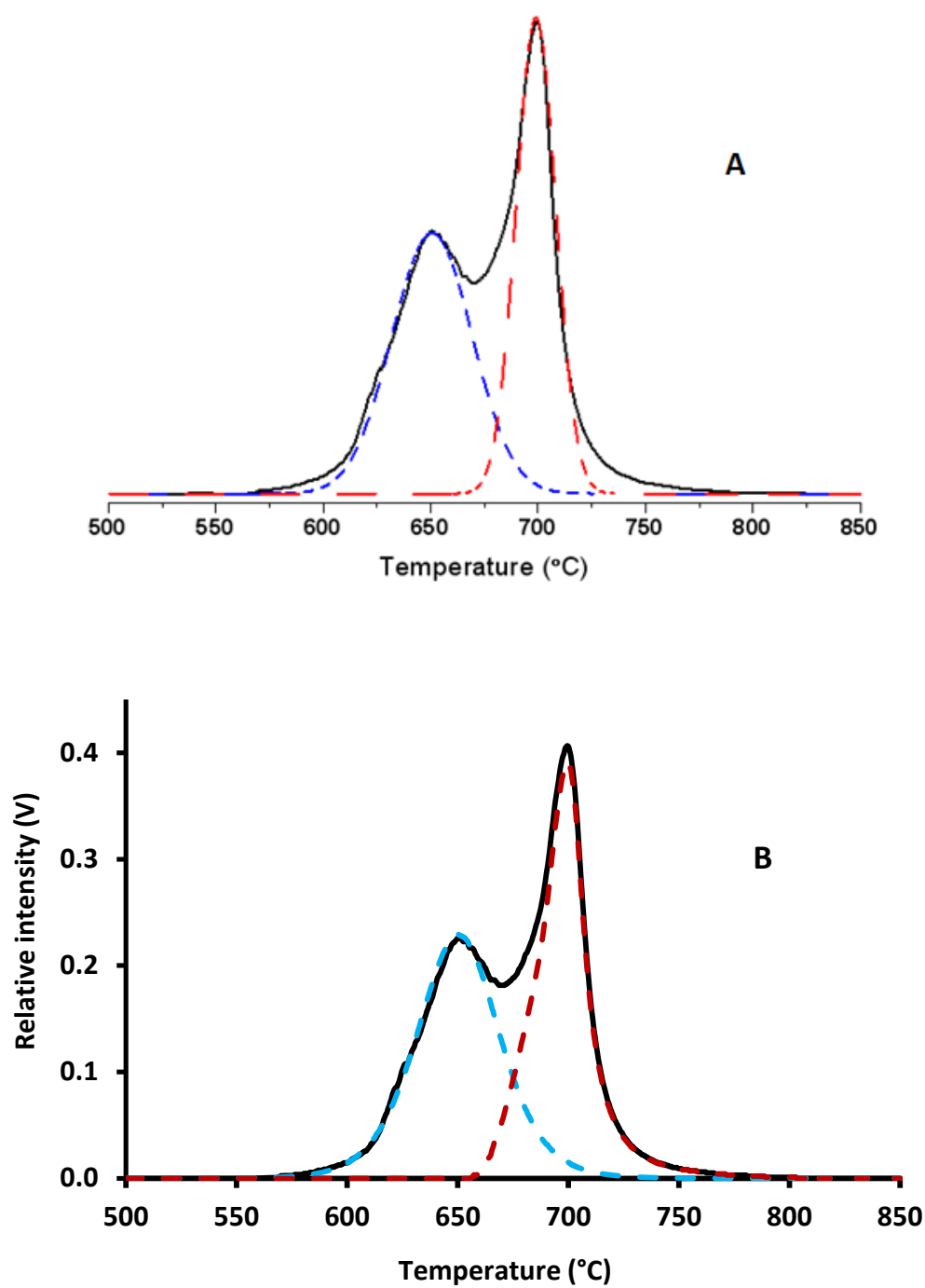


Figure 3.2 TPD-TCD profile of Li_2NH . The two peaks are resolved by (A) Gaussian equation fitting and (B) kinetic calculation.

Table 3.1 Molar fraction of H₂ and N₂ produced in the decomposition of Li₂NH at different temperatures.

T(°C)	H ₂ (mol%)	N ₂ (mol%)
600	35.1	64.9
610	39.4	60.6
620	48.4	51.6
630	47.4	52.6
640	48.1	51.9
650	49.5	50.5
660	48.5	51.5
670	46.2	53.8
680	46.2	53.8
690	41.2	58.8
700	50.8	49.2
710	56.1	43.9

However, as shown in Figure 3.2, the decomposition of Li₂NH is not a single step, because there were two TPD peaks (one at 650 °C and the other at 700 °C) between 550 and 800 °C. This means that the decomposition contains two steps. In other words, an intermediate species Li_xNH_y was formed as follows:

$$\frac{x}{2} Li_2NH = Li_xNH_y + \frac{x-2}{4} N_2 + \frac{x-2y}{4} H_2 \quad (3.24)$$

$$Li_xNH_y = xLi + \frac{1}{2} N_2 + \frac{y}{2} H_2 \quad (3.25)$$

Because the molar ratio of H₂ to N₂ is equal to 1 (Table 3.1), one can know from equation 3.25 that y should be 1. The ratio of $(\frac{x-2}{4} + \frac{x-2y}{4})$ to $(\frac{1}{2} + \frac{y}{2})$ equals

to the ratio of the areas of peak 1 (corresponding to reaction 3.24) to peak 2 (corresponding to reaction 3.25). The overlapped peaks in Figure 3.2 were resolved by Gaussian function fitting, revealing that the areas of the two peaks are the same. This means that the value of x is 4. Therefore, the intermediate species in the decomposition of Li_2NH is Li_4NH .

The kinetics of the first step of the decomposition of Li_2NH (Reaction 3.24) was evaluated from Figure 3.2. Because Gaussian fitting showed that the two peaks of Li_2NH TPD (Figure 3.2A) have equal areas, the area (S_{t1}) of the first peak should be the half of the total area of the two peaks. Furthermore, one can make an approximation that the part of the first peak before the highest point has a negligible overlapping with the second peak. Therefore, the data, which are listed in Table 3.2, were obtained for temperatures not larger than T_{p1} (temperature at the highest point of the first peak). From Table 3.2, one can obtain a linear relationship between $\frac{1}{T_i} - \frac{S_p \ln S_i}{h_p T_p^2}$ and $\ln h_i$, which is shown in Figure 3.3. From the slope (-64180) and intersection (64.86) of the line, one can obtain activation energy (E_a) of 533.6 kJ/mol, decomposition order (n) of 1.84, and pre-exponential factor (A) of 1.34×10^{29} . This indicates that the decomposition of Li_2NH to Li_4NH is almost the second-order reaction.

Table 3.2 Data obtained from the first peak of the composition of Li₂NH.

T _{p1} (°C)	h _{p1} (V)	S _{p1} (VK)	S _{t1} (VK)	a(mg/VK)	β(°C/min)
650.4	0.23	5.54	11.21	0.49	5
T _i (°C)	lnS _i	$\frac{1}{T_i} - \frac{S_p \ln S_i}{h_p T_p^2}$		lnh _i	
600.3	2.40	0.001076		-4.22	
610.1	2.38	0.001064		-3.52	
620.2	2.33	0.001053		-2.57	
630.3	2.22	0.001043		-2.09	
640.1	2.05	0.001036		-1.70	
650.4	1.71	0.001034		-1.48	

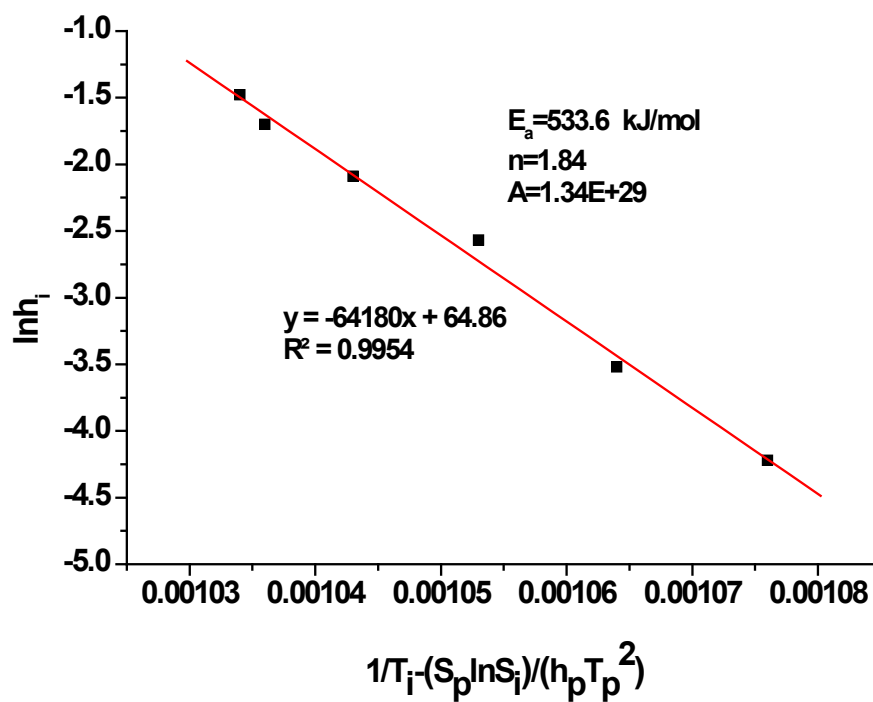


Figure 3.3 $\ln h_i$ vs. $(\frac{1}{T_i} - \frac{S_p \ln S_i}{h_p T_p^2})$ for the first peak of the composition of Li₂NH.

According to Equation 3.22 with obtained E_a , n , and A , one can draw the entire first peak (corresponding to reaction 3.24) as the dashed blue peak (Figure 3.2B). The area of the first peak generated by Equation 3.22 is exactly equal to the half of the area of the two peaks, which is consistent with the peak separation from the Gaussian function fitting.

The subtraction of the first peak height (calculated with Equation 3.22) from the total height of the overlapped two peaks can generate the separated second peak (Figure 3.2B), from which the data for the second peak were obtained (Table 3.3).

As shown in Figure 3.4, one can see a linear relationship between $\frac{1}{T_i} - \frac{S_p \ln S_i}{h_p T_p^2}$ and $\ln h_i$.

This provides the kinetic parameters for reaction 3.25, including activation energy (E_a) of 754.2 kJ/mol, decomposition order (n) of 1.18, and pre-exponential factor (A) of 1.05×10^{40} . Therefore, the decomposition of Li_4NH to Li , H_2 , and N_2 is almost the first-order reaction.

Table 3.3 Data obtained from the second peak of the composition of Li₂NH.

T _{p2} (°C)	h _{p2} (V)	S _{p2} (VK)	S _{i2} (VK)	a(mg/VK)	β(°C/min)
699.8	0.39	4.82	11.21	0.49	5
T _i (°C)	lnS _i	$\frac{1}{T_i} - \frac{S_p \ln S_i}{h_p T_p^2}$		lnh _i	
667.1	2.41	0.001032		-3.31	
672.4	2.38	0.001027		-2.64	
677.3	2.34	0.001022		-2.18	
682.5	2.27	0.001017		-1.82	
687.4	2.17	0.001013		-1.55	
692.6	2.00	0.001009		-1.20	
697.2	1.76	0.001008		-0.98	
699.8	1.57	0.001007		-0.94	

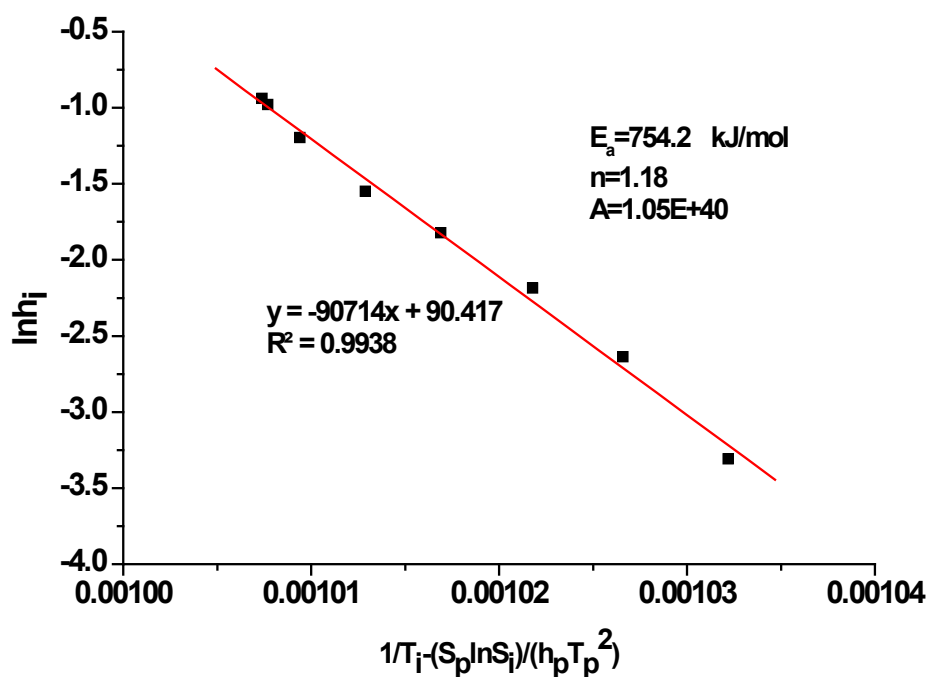


Figure 3.4 $\ln h_i$ vs. $(\frac{1}{T_i} - \frac{S_p \ln S_i}{h_p T_p^2})$ for the second peak of the composition of Li₂NH.

Furthermore, the solid products from the Li_2NH TPD process were characterized by XRD. As shown in Figure 3.5, one can see cubic Li_2NH peaks at 550 °C before the decomposition started. With increasing temperature, there is an obvious peak-shifting in the XRD pattern of Li_2NH (Figure 3.5), corresponding to the change of cubic lattice parameter. As discussed above, the decomposition of Li_2NH produced Li_4NH in the first step (reaction 3.24). The XRD patterns for all samples, which were obtained in the temperature range where two TPD peaks occurred, indicated that there is only a cubic phase. In other words, Li_4NH should possess a similar cubic crystal structure as Li_2NH . The lattice parameters of the solid products obtained at different temperatures were listed in Table 3.4. It can be seen that the lattice parameter decreases with increasing decomposition of Li_2NH . Because the first peak is associated with the decomposition of Li_2NH to Li_4NH , the samples, which were obtained in the temperature range of the first peak, should contain both Li_2NH and Li_4NH . The observation of only one phase in their XRD patterns indicates that Li_2NH and Li_4NH form a solid solution. Furthermore, the lattice parameters of those samples were correlated with molar ratio of Li_2NH to Li_4NH when the Li_2NH content is greater than or equal to 13 mol%, leading to a linear equation (Figure 3.6):

$$a = 0.0027x + 0.5033 \quad (3.26)$$

Where a is lattice parameter (with unit of nm) and x is molar fraction of Li_2NH in $\text{Li}_2\text{NH}/\text{Li}_4\text{NH}$ solid solution. This indicates that the solid solution follows Vegard's law. Furthermore, the above equation can be used to predict the lattice parameter of

Li_4NH , which is 0.5033 nm. It was reported that Li_4NH can be formed from the reaction of LiNH_2 and Li_3N in liquid Li [116] or the reaction of Li_3N and LiH [117]. The Li_4NH obtained from those reactions occupied a tetragonal structure [116, 117]. Furthermore, the DFT calculations showed that the tetragonal structure is stable [105]. In contrast, the Li_2NH decomposition produced cubic Li_4NH . This indicates that cubic Li_2NH induced the formation of cubic Li_4NH and stabilize it via the formation of solid solution. However, when the content of cubic Li_2NH becomes too small to stabilize the relatively instable cubic structure of Li_4NH , the cubic Li_4NH might tend to more stable tetragonal state. This can explain why the lattice parameter of solid solution decreased very much with increasing Li_4NH content when the content of Li_2NH is less than 13 % (Figure 3.6).

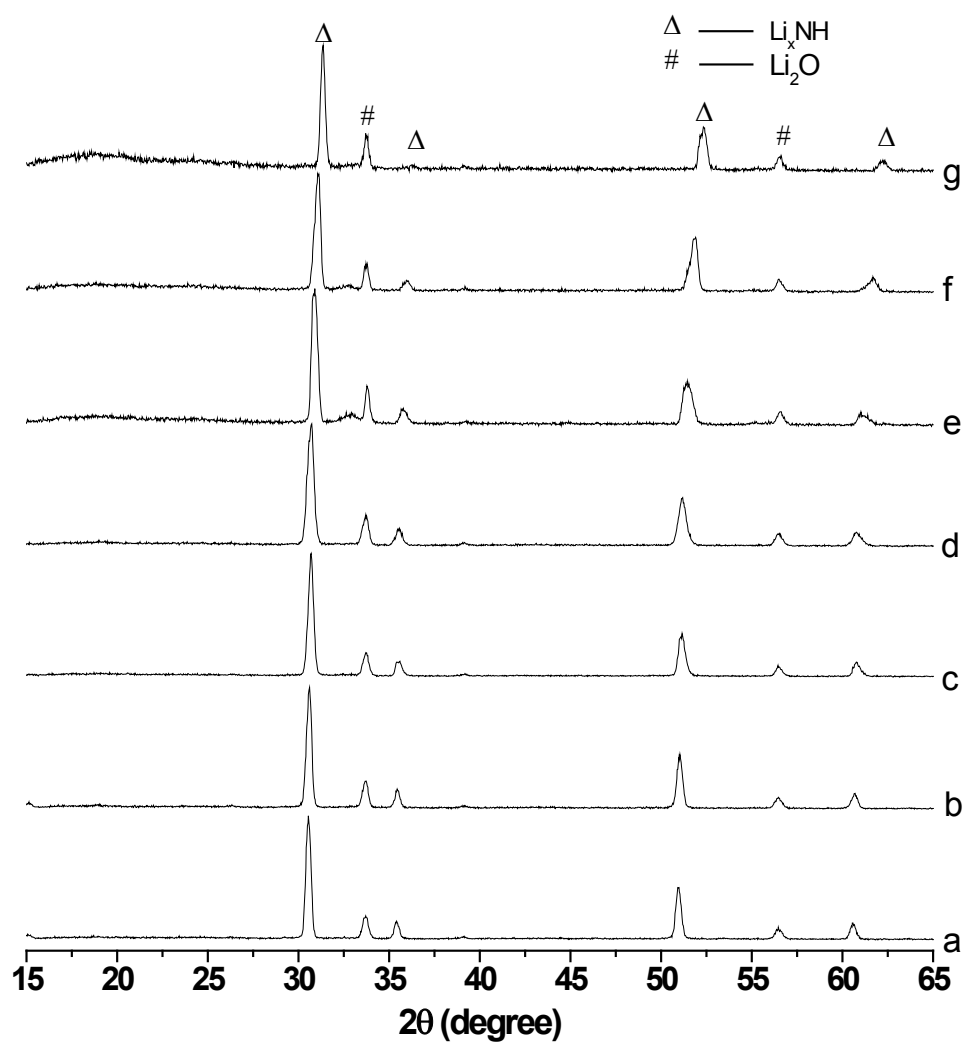


Figure 3.5 XRD patterns of the solid products from the TPD process of Li_2NH that were stopped at (a) 550 °C, (b) 607 °C, (c) 650 °C, (d) 680 °C, (e) 690 °C, (f) 700 °C, and (g) 710 °C.

Table 3.4 Lattice parameters of the solid products from the TPD process of Li_2NH .

T (°C)	Molar fraction of Li_2NH in $\text{Li}_2\text{NH}+\text{Li}_4\text{NH}$ solid solution	a (nm)
550	1.00	0.5067
607	0.99	0.5056
650	0.66	0.5044
680	0.13	0.5039
690	0.06	0.5013
700	0.03	0.4980
710	0.02	0.4939

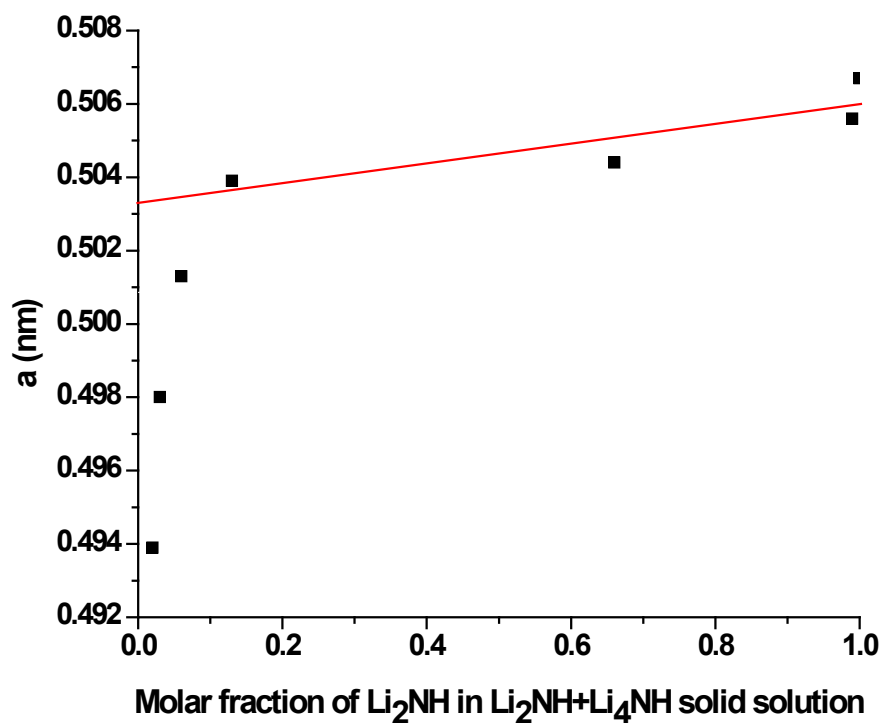


Figure 3.6 Lattice parameters of the solid products from the TPD process of Li_2NH vs. the molar fraction of Li_2NH in $\text{Li}_2\text{NH}/\text{Li}_4\text{NH}$ solid solution.

Thus, Li_2NH is decomposed into Li , H_2 and N_2 without Li_3N formation. This can further be supported by the XRD measurement, in which no Li_3N in the samples of LiNH_2 decomposed at 650 and at 690 °C was detected (Figure 3.5). Furthermore, Li_3N sample was subjected to TPD measurements. As shown in Figure 3.7, one can see that Li_3N started to decompose at 470 °C, which is lower than that (550 °C) of Li_2NH . This indicates that Li_2NH is more stable than Li_3N , which can explain why no Li_3N can be formed in the decomposition of Li_2NH .

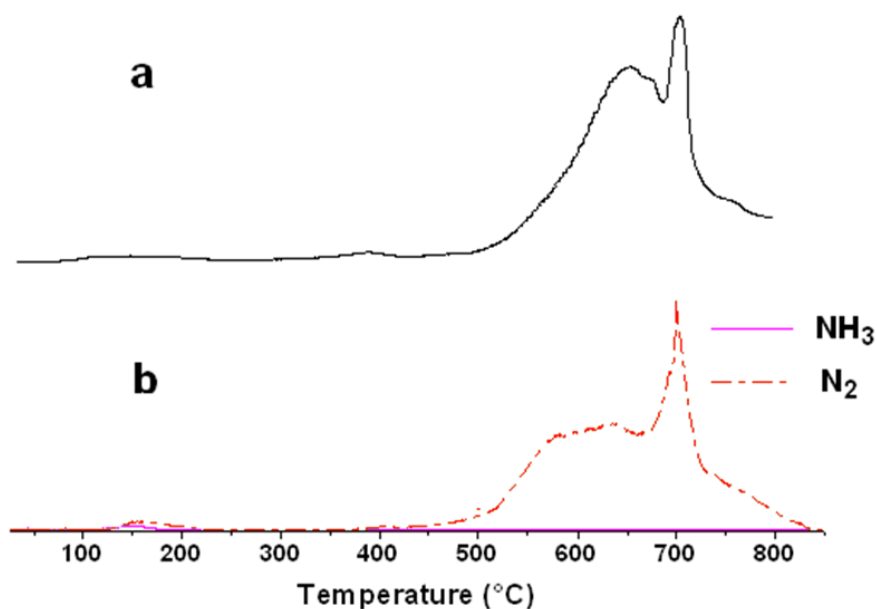


Figure 3.7 (a) TPD-TCD profile and (b) TPD-MS profile of Li_3N .

3.4 Conclusion

Li_2NH is decomposed into Li , H_2 and N_2 without formation of Li_3N in the temperature range of 550 to 800 °C. The decomposition of Li_2NH produced Li , H_2 and N_2 via two steps: (1) Li_2NH into Li_4NH , N_2 , and H_2 and (2) Li_4NH into Li , N_2 , and H_2 . The first step is the second-order reaction with activation energy of 533.6 kJ/mol, whereas the second step is the first-order reaction with activation energy of 754.2 kJ/mol. Li_4NH , which was generated in the decomposition of Li_2NH , formed a solid solution with Li_2NH . In the solid solution, Li_4NH possesses a similar cubic structure as Li_2NH . The lattice parameter of cubic Li_4NH is 0.5033 nm.

Our hypothesis that a new compound Li_4NH may form during the decomposition of Li_2NH is true.

Chapter 4 Effect of anion promoter Cl^- on the decomposition of lithium amide *

4.1 Introduction

Dehydrogenation of $\text{Li}_2\text{NH}/\text{LiH}$ back to Li_3N (the reverse direction of Reaction 2.1) is very difficult, the attention was focused on the reaction 4.2 as a reversible hydrogen storage process, which provides 6.8 wt % hydrogen capacity [52]. The dehydrogenation mechanism of LiNH_2/LiH consists of two steps with NH_3 intermediate species (Equations 2.3 and 2.4) [34]. The reaction between NH_3 and LiH (Equation 2.4) was exothermic and ultra fast [34]. Therefore, the decomposition of LiNH_2 (Equation 2.3) is the rate-determining step, which requires a high temperature.

The DOE target for hydrogen storage dehydrogenation temperature is between $-40\text{ }^\circ\text{C}$ and $85\text{ }^\circ\text{C}$ [6]. However, in the Li-N-H system, the H_2 releasing temperature is nearly $200\text{ }^\circ\text{C}$ [33], which is too high to be used for on-board hydrogen storage.

*The material contained in this chapter was previously published in the journal *Industrial and Engineering Chemistry Research* 2011, 50 (13), 8058-8064 by Junqing Zhang and Yun Hang Hu. See Appendix for documentation of permission to republish this material.

Current efforts to decrease the dehydrogenation temperature of Li-N-H system are being focused on the introduction of metal or cation promoters, including Mg, Ni, Fe, Co, Mn, VCl_3 , and TiCl_3 [47-49]. Figure 4.1 shows the thermal desorption profiles of H_2 and NH_3 of the ball milled mixtures of LiNH_2 and LiH with 1:1 molar ratio, in which added with a small amount (1 mol%) of Ni, Fe and Co nanometer sized metals, VCl_3 and TiCl_3 before milling. The gases were monitored by mass spectrometry with the sample heating rate 5 °C/min [40]. It shows that all the additives have effects on decreasing the hydrogen releasing temperature.

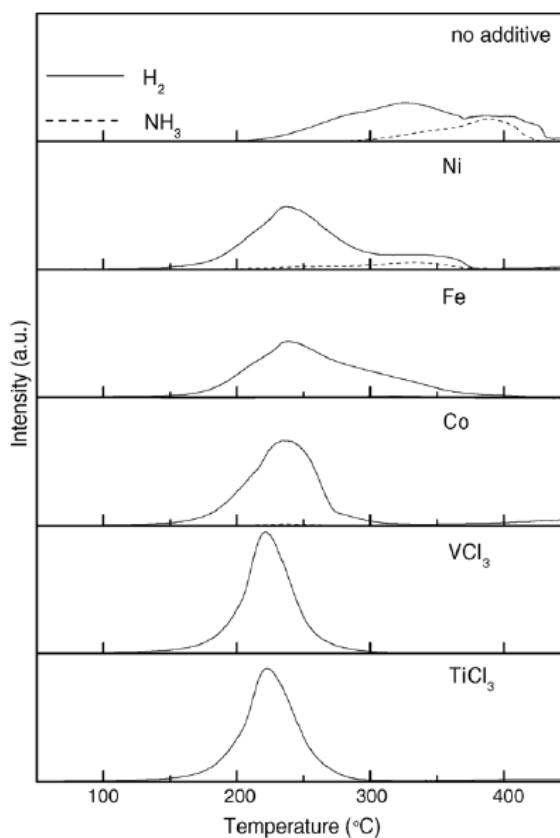


Figure 4.1 Thermal desorption profiles of H_2 and NH_3 of the ball milled mixtures of $LiNH_2$ and LiH with 1:1 molar ratio, in which added with a small amount (1 mol%) of Ni, Fe and Co nanometer sized metals, and VCl_3 and $TiCl_3$ before milling [40]. (With permission from Elsevier)

Nevertheless, effects of doping-anions on this Li-N-H hydrogen storage system have attracted little attention. One of the reasons is probably that the anion of a promoter is always accompanied with a corresponding cation. The effect of the promoter is often attributed to its cation instead of its anion.

We hypothesize that the decomposition of $LiNH_2$ may be promoted by anion promoter. This is based on the following observation. It can be seen in Figure 4.1

that the H_2 peak shapes by adding VCl_3 and TiCl_3 are almost the same. Since the cations are different, the effect probably should be attributed to the anion (Cl^-). The decomposition of LiNH_2 is the elementary and rate-determining reaction of the hydrogen releasing process in the LiNH_2/LiH mixture. So, the decomposition of LiNH_2 may be promoted by the anion (Cl^-).

As the realization of the important roles that anions play in biology, [119] catalysis [120], and the environment [121, 122] has grown; interest in anion chemistry has become more widespread. For example, the stringent environmental regulations on the sulfur content in transportation fuels force ones to use hydrotreatment catalysts with enhanced hydrogenating and acid functionalities in order to improve the removal of the most refractory sulfur compounds, substituted dibenzothiophenes, from the different petroleum fractions. Anion-modified alumina-based catalysts present these characteristics [123, 124]. This work stimulated much interest to reveal why the doping-anion can exhibit so remarkable promoting-effect. Nevertheless, effects of doping-anions on hydrogen storage materials have attracted limited attention. One of reasons is probably that the anion of a promoter is always accompanied with a corresponding cation. The effect of the promoter is often attributed to its cation instead of its anion. However, recently, the anion promoting effects on hydrogen storage in LiBH_4 and MgH_2 were reported [125-128]. Furthermore, in the Li-N-H hydrogen storage system, LiNH_2 doped with LiBH_4 was intensively studied [129-132]. This proved the effect of $[\text{BH}_4]^-$ anion on hydrogen storage in Li-N-H system.

In this work, the effect of Cl^- anion on the decompositions of LiNH_2 and Li_2NH was examined, because Cl^- anion was widely employed as a promoter to improve various catalysts. As a result, the remarkable effects of Cl^- anion were found.

4.2 Experiments

4.2.1 Sample preparations

Lithium amide powder (95%) and lithium chloride reagent (99+ %), which had been purchased from Aldrich Chemical Co., were used without any further purification. The introduction of lithium chloride into lithium amide was carried out by mixing them with an agate mortar and pestle for 5 min in an argon filled glove box to protect from moisture. The molar ratio of lithium amide and lithium chloride in the mixtures varied from 9:1 to 1:9.

4.2.2 Temperature-programmed decomposition

The temperature-programmed decomposition (TPD) experiments were performed as follows: A sample (0.01 g) was loaded into a vertical quartz tube reactor, which was located in an electric tube furnace. The temperature of the reactor was increased to 800 °C at a rate of 5 °C/min. Argon (30 mL/min) was employed as a carrier gas through the reactor to bring the gaseous products of the decomposition of the sample into a thermal conductivity detector (TCD, Figure 2.1), generating a

TPD-TCD profile. Furthermore, to determine all gas products except hydrogen, helium was used to carry the products from the TPD reactor into a mass spectrometer (HP 5970 series mass selective detector, Figure 2.2) instead of TCD detector, generating a TPD-MS profile.

4.2.3 X-ray diffraction (XRD)

A sample (0.1 g) was loaded into a vertical quartz tube reactor (5-mm diameter) located in an electric tube furnace. Argon (30 mL/min) was introduced into the reactor at room temperature, followed by heating to a selected temperature at a rate of 5 °C/min and then cooling down to room temperature. The obtained samples were subjected to XRD measurements, which were performed with a Siemens D500 X-ray diffraction instrument equipped with a Cu K α source, at 45 kV and 35 mA (Figure 2.3). The scanning speed was 1°/min. The mixture of LiNH₂ and LiCl samples were covered with plastic wrap during the XRD measurements to prevent LiCl from absorbing the H₂O in air.

4.3 Results and discussion

To examine the effect of anion (Cl⁻) on the decomposition of LiNH₂, Cl⁻ was doped into LiNH₂ via mixing LiCl and LiNH₂ with various mole ratios from 1:9 to 9:1 so that any new cation was not introduced. The Cl⁻-doped LiNH₂ samples were

subjected to TPD measurements with TCD and MS detectors. As shown in Figure 4.2, LiCl changed the TPD profiles of LiNH₂, namely, a new NH₃ peak occurred at low temperature of about 250 °C besides the original NH₃ peak at 330 °C. This indicates that Cl⁻ promoted the decomposition of LiNH₂ into Li₂NH and NH₃. This can be explained as the interaction between Cl⁻ and LiNH₂, which can weaken the bond between Li⁺ and (NH₂)⁻. The interaction is determined by the contact between the surfaces of LiCl and LiNH₂ particles to form an interface, which leads to the decomposition of LiNH₂ at a low temperature. Furthermore, LiCl can absorb NH₃ to form a series of lithium chloride ammonia complexes Li(NH₃)_xCl (x=4, 3, 2, 1) [133]. Therefore, the temperature, at which we can detect NH₃, is dependent on the stability of the complexes, which can decompose to release NH₃ at temperature above 200 °C [133]. This can explain why the new NH₃ was detected at temperature of about 250 °C. The original NH₃ at 330 °C still remained, because the LiNH₂ inside the particles don't contact LiCl. It would be noted that the peaks at about 100 °C were confirmed as a result of the reaction between H₂O adsorbed on LiCl and LiNH₂. The adsorbed H₂O originated from the air due to exposing the sample to it.

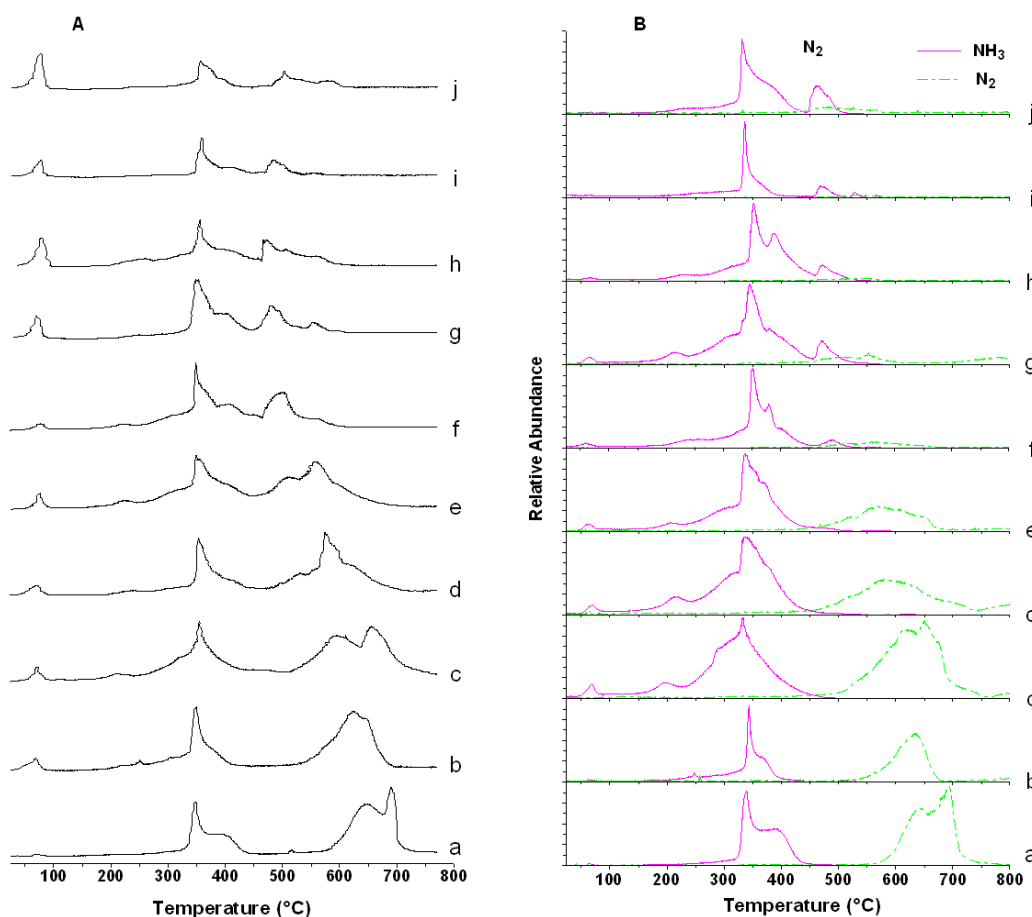


Figure 4.2 (A) TPD-TCD profiles and (B) TPD-MS profiles of LiCl-doped LiNH₂ with various LiNH₂/LiCl mole ratios: (a) pure LiNH₂, (b) 9:1, (c) 8:2, (d) 7:3, (e) 6:4, (f) 5:5, (g) 4:6, (h) 3:7, (i) 2:8, and (j) 1:9.

Furthermore, Cl⁻ exhibited even greater effect on the peaks at high temperature, namely, the two peaks at 645 °C and 690 °C in the TPD profile of LiNH₂ without Cl⁻ merged into a broad one in that of Cl⁻-doped LiNH₂. In addition, the peak-temperature decreased from 625 to 530 °C with increasing LiCl content. It is well-known that LiCl can form a eutectic liquid phase with another Li-based ionic compound below 500 °C [134]. Therefore, it is reasonable for us to believe that LiCl

and Li_2NH can form a eutectic liquid phase at about 500 °C. As a result, LiCl and Li_2NH have a good contact and thus Cl^- can catalyze the decomposition of Li_2NH via the formation of Cl-Li-N bonds. This catalytic performance of Cl^- was further supported by the XRD measurements, which showed that LiCl was still present after the decomposition of Li_2NH (Figure 4.3). It should be noted that there is little evidence of Li_2NH on the XRD pattern above 400 °C (Figure 4.3), probably because Li_2NH became amorphous due to the formation of its eutectic phase with LiCl .

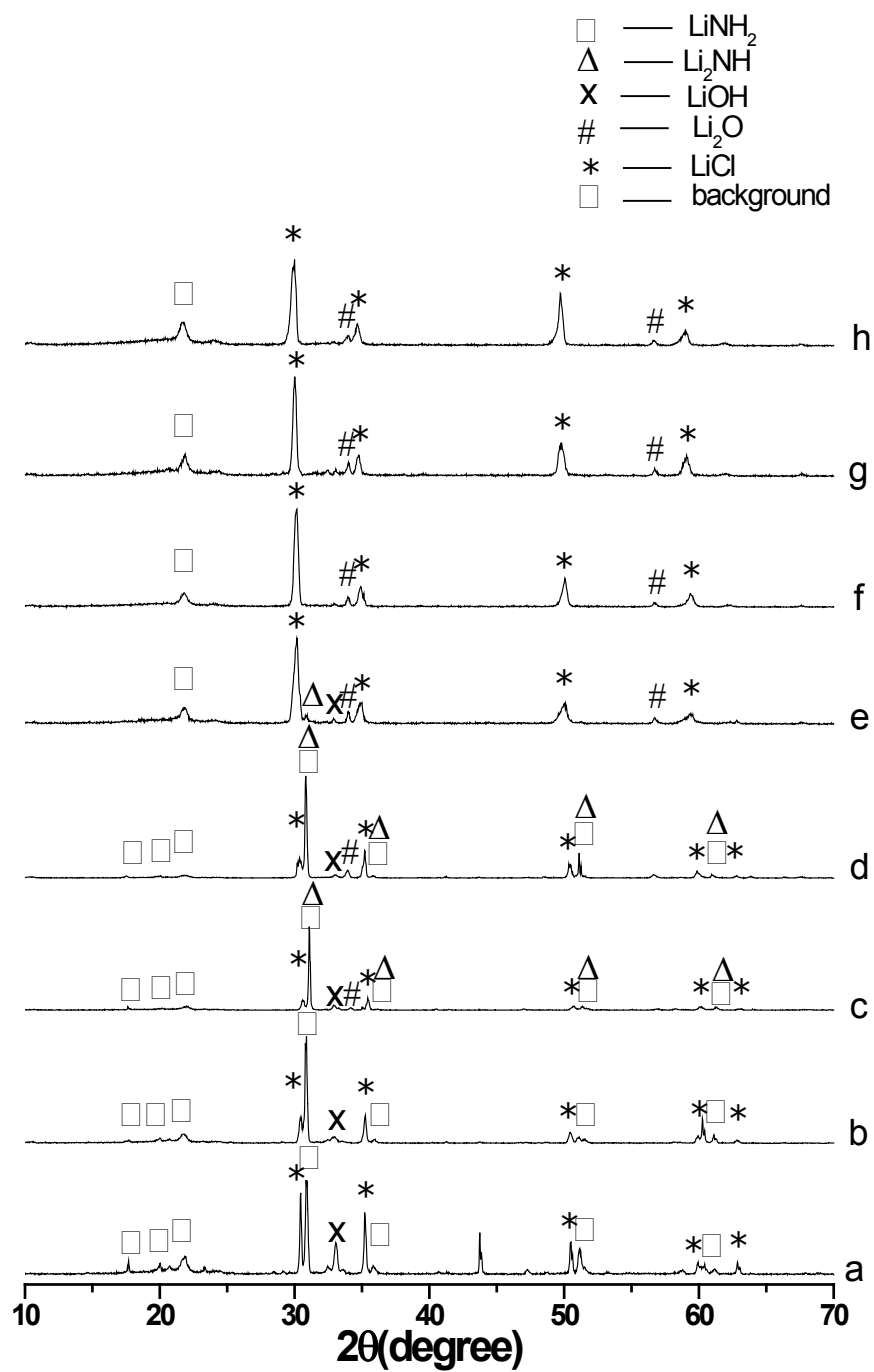


Figure 4.3 XRD patterns of the solid products from the TPD process of $\text{LiNH}_2/\text{LiCl}$ (8:2 molar ratio) that was stopped at various temperatures: (a) room temperature, (b) 160 °C, (c) 275 °C, (d) 320 °C, (e) 330 °C, (f) 380 °C, (g) 520 °C, and (h) 570 °C.

4.4 Conclusion

Chloride ion (Cl^-) had great effects on the decompositions of LiNH_2 and Li_2NH . The introduction of Cl^- resulted in the generation of a new peak at low temperature of about $250\text{ }^\circ\text{C}$ besides the original peak at $330\text{ }^\circ\text{C}$ in the decomposition of LiNH_2 into Li_2NH and NH_3 . Furthermore, Cl^- showed an even greater effect on the decomposition of Li_2NH , namely, the two peaks in TPD profiles merged into one and the peak temperature decrease from 645 to $530\text{ }^\circ\text{C}$ with increasing molar ratio of LiCl to LiNH_2 .

Our hypothesis that the decomposition of LiNH_2 may be promoted by anion promoter is true for introducing Cl^- .

Chapter 5 Chemical stability of lithium nitride in air*

5.1 Introduction

Lithium nitride (Li_3N) is attracting much attention for energy application. As a very reactive material, Li_3N could exothermically convert greenhouse gas CO_2 to two valuable solid materials—carbon nitride (C_3N_4) and lithium cyanamide (Li_2CN_2) compounds at temperature of 250 °C or above [135]. This would provide a novel process to control CO_2 emissions.

The critic issue of hydrogen fuel economy is the lack of an efficient, safe, and low cost technique for hydrogen storage. The practical application of liquid hydrogen storage technology is limited by the large amount of energy consumed during liquefaction and the continuous hydrogen boil-off [2]. Compressed hydrogen in a cylinder, which is widely employed for hydrogen storage in laboratories, requires an ultrahigh pressure to achieve enough hydrogen fuel for a reasonable driving cycle of 300 miles, causing a safety issue [3]. For those reasons, hydrogen storage in solid materials is considered as the safest and most effective way of handling hydrogen for transportation application [136]. In the past 10 years, Li_3N was intensively investigated as hydrogen storage material [33-51].

*The material contained in this chapter was planned for submission to the journal *Industrial and Engineering Chemistry Research* by Junqing Zhang and Yun Hang Hu.

Li_3N possesses a very high Li^+ conductivity along layers perpendicular to the crystallographic c axis of $\alpha\text{-Li}_3\text{N}$ [61-65]. Therefore, Li_3N would be a promising material for lithium ion batteries.

Three phases (α , β , and γ) have been identified for Li_3N . $\alpha\text{-Li}_3\text{N}$ can be prepared by the reaction between Li and N_2 at 400 °C [57]. Its structure was evaluated by Zintl and Brauer [58] and later revised by Rabenau and Schultz [59]. They revealed that $\alpha\text{-Li}_3\text{N}$, which occupies the space group of $P6/mmm$ with $a = 3.648(1)$ Å and $c = 3.875(1)$ Å, consists of Li_2N layers that are alternated by pure-lithium layers along c direction. However, $\alpha\text{-Li}_3\text{N}$ contains intrinsic defects (1-2% Li vacancies) in the $\alpha\text{-Li}_2\text{N}$ layers [66], leading to its high ionic conductivity. Furthermore, such a defect structure of $\alpha\text{-Li}_3\text{N}$ creates its possibility for a pressure-induced phase transformation, namely, $\beta\text{-Li}_3\text{N}$ can be produced via the phase transformation of $\alpha\text{-Li}_3\text{N}$ at pressure of 0.4~4GPa [67, 68]. The $\beta\text{-Li}_3\text{N}$ possesses a hexagonal structure in the $P6_3/mmc$ space group with $a = 3.552(1)$ Å and $c = 6.311(3)$ Å ($Z = 2$) in which pure-lithium layers alternate LiN layers as opposed to the Li_2N layers in α phase [71]. The reverse phase transformation from $\beta\text{-Li}_3\text{N}$ back to $\alpha\text{-Li}_3\text{N}$ can take place by heat treatment at about 500 °C [70, 71]. $\gamma\text{-Li}_3\text{N}$, which is a cubic face-centered crystal compound, was predicted to be formed at ultra-high pressures [69, 72]. Furthermore, the transformation of $\beta\text{-Li}_3\text{N}$ to $\gamma\text{-Li}_3\text{N}$ was observed in the pressure range of 36-45 GPa [73].

The electronic and optical properties of Li_3N have been evaluated experimentally [71, 74, 75] and theoretically [76-82]. However, to our best

knowledge, the chemical stability of Li_3N in air, which is important for its energy application, has not been investigated. For this reason, in this work, the degradation of Li_3N in air was systematically explored by XRD, FT-IR, and UV-vis absorption. Furthermore, the difference of chemical stabilities between $\alpha\text{-Li}_3\text{N}$ and $\beta\text{-Li}_3\text{N}$ was evaluated.

5.2 Experiments

5.2.1 Treatment of Li_3N in O_2

Li_3N powder ($\geq 99.5\%$, Sigma-Aldrich), which was previously vacuumed for degas at room temperature for 2 h, was treated with O_2 at pressure of 50 psi and a selected temperature (170, 230, 280, or 330 $^\circ\text{C}$) in a ceramic tube reactor for 3h.

5.2.2 Degradation of Li_3N in air

Li_3N powder ($\geq 99.5\%$, Sigma-Aldrich) was exposed to air at room temperature. The sample at various exposure times was subjected to structure characterizations (see section 2.3) to monitor Li_3N degradation.

5.2.3 Characterization

The UV-vis absorption spectra of Li_3N samples, which were previously treated in O_2 or air, were recorded using a UV-vis spectrophotometer (Shimadzu, Model UV-2450, Figure 5.1) in the wavelength range of 200–800 nm at room temperature. Barium sulfate was used as a reference material. The X-ray diffraction (XRD) measurements for the samples were performed with a Scintag XDS2000 Powder Diffractometer equipped with a $\text{Cu K}\alpha$ source, at 45 kV and 35 mA (Figure 2.3). The scanning speed and range were 1 °/min and 15-70 °, respectively. The Li_3N samples were also subjected to Fourier transform infrared spectroscopy (FT-IR) measurements that were carried out using a Perkin Elmer Spectrum One FT-IR spectrometer (Figure 5.2).

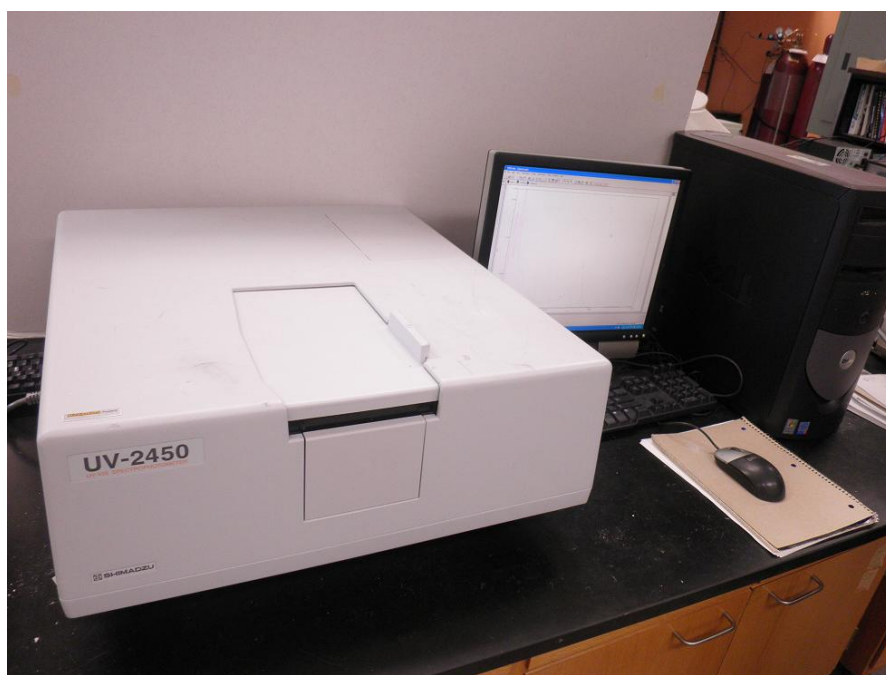


Figure 5.1 Shimadzu UV-2450 Spectrometer.



Figure 5.2 Perkin Elmer Spectrum One FTIR spectrometer.

5.3 Results and discussion

5.3.1 Oxidation of Li_3N in O_2

It is well-known that dry air contains N_2 (78.084% volume), O_2 (20.946% volume), Ar (0.934% volume), CO_2 (0.035% volume), and trace amount of other gases (0.001% volume totally). Furthermore, common air is composed of dry air and H_2O vapor (1 - 4% volume). The effect of trace gases on Li_3N is negligible due to their very small concentrations (0.001% volume totally in dry air). N_2 and CO_2 could not affect Li_3N at room temperature [135]. However, it is unclear whether O_2 has effect on Li_3N at room temperature. To examine the effect, Li_3N was treated by O_2 at various temperatures. As shown in Figure 5.3a, one can see that commercial Li_3N without any treatment contains α - and β -phases, which is consistent with the reported observations [71-73]. No new phase was formed by the O_2 treatment at 170 °C (Figure 5.3b), indicating no reaction between Li_3N and O_2 at 170 °C. However, when temperature was increased to 230 and 280 °C, O_2 can partially convert Li_3N into Li_2O in 3h (Figure 5.3c and d). Furthermore, Li_3N was completely converted into Li_2O by O_2 at 330 °C (Figure 5.3e). One can conclude that the oxidation of Li_3N in O_2 can take place at temperature of 230 °C or higher. In other words, Li_3N is stable in O_2 at room temperature.

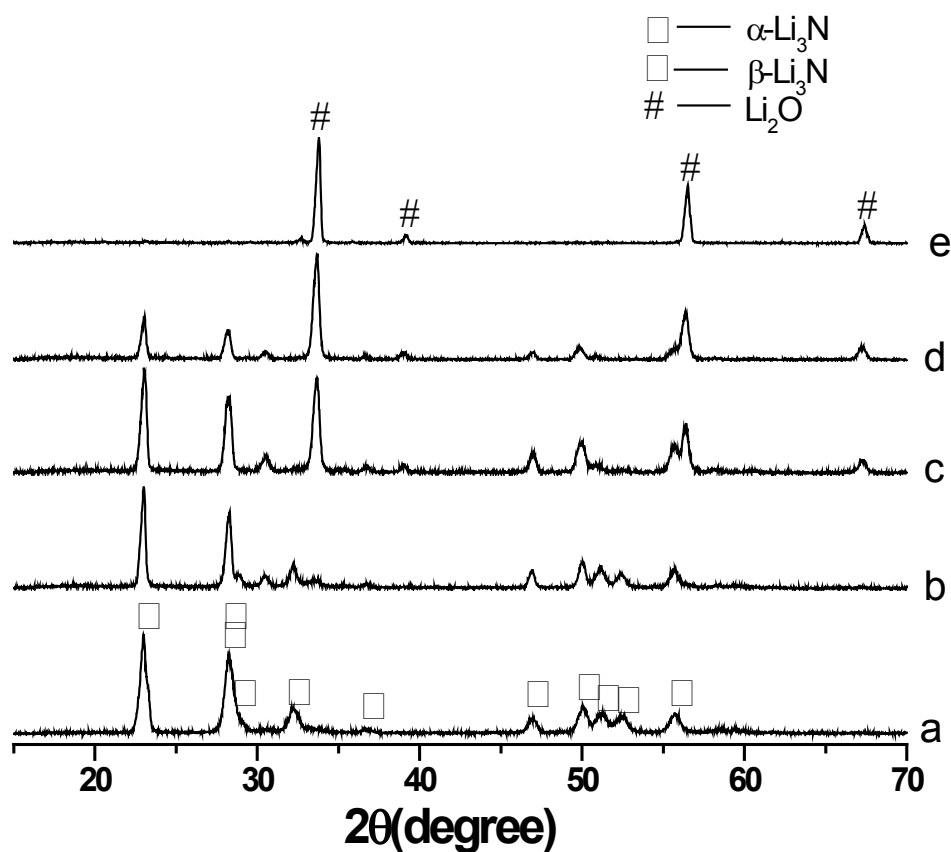
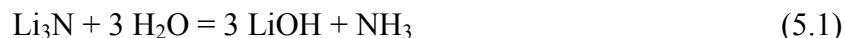


Figure 5.3 XRD patterns of Li_3N (a) without treatment and treated with O_2 for 3 h at (b) 170 °C, (c) 230 °C, (d) 280 °C, and (e) 330 °C.

5.3.2 Effect of H_2O in air on Li_3N

In order to evaluate the effect of H_2O vapor in air on Li_3N structure, XRD patterns were obtained for Li_3N powder samples, which were previously exposed to air with relative humidity of 16%. As shown in Figure 5.4, after exposing Li_3N to air, new phases of LiOH and Li_2CO_3 were formed. Furthermore, as exposure time increased, the relative intensity of Li_2CO_3 increased, whereas the relative intensity of

LiOH first increased and then decreased. This indicates that Li_2CO_3 would be the product of reaction between LiOH and CO_2 . In addition, NH_3 was smelled near Li_3N in air. Therefore, the degradation of Li_3N in air can be described as follows:



To reveal the degradation difference between $\beta\text{-Li}_3\text{N}$ and $\alpha\text{-Li}_3\text{N}$ in air, the molar ratios of $\beta\text{-Li}_3\text{N}$ to $\alpha\text{-Li}_3\text{N}$ at various exposure times were calculated from XRD diffraction peaks of $\beta\text{-Li}_3\text{N}$ (103) and $\alpha\text{-Li}_3\text{N}$ (111) by VOLFRAC program based on Cullity method [137]. The results are listed in Table 5.1, which shows that the molar ratio of $\beta\text{-Li}_3\text{N}$ to $\alpha\text{-Li}_3\text{N}$ of the Li_3N sample decreased with increasing exposure-time in air. This indicates that $\beta\text{-Li}_3\text{N}$ reacts with H_2O faster than $\alpha\text{-Li}_3\text{N}$. Therefore, $\alpha\text{-Li}_3\text{N}$ is more stable than $\beta\text{-Li}_3\text{N}$ in air.

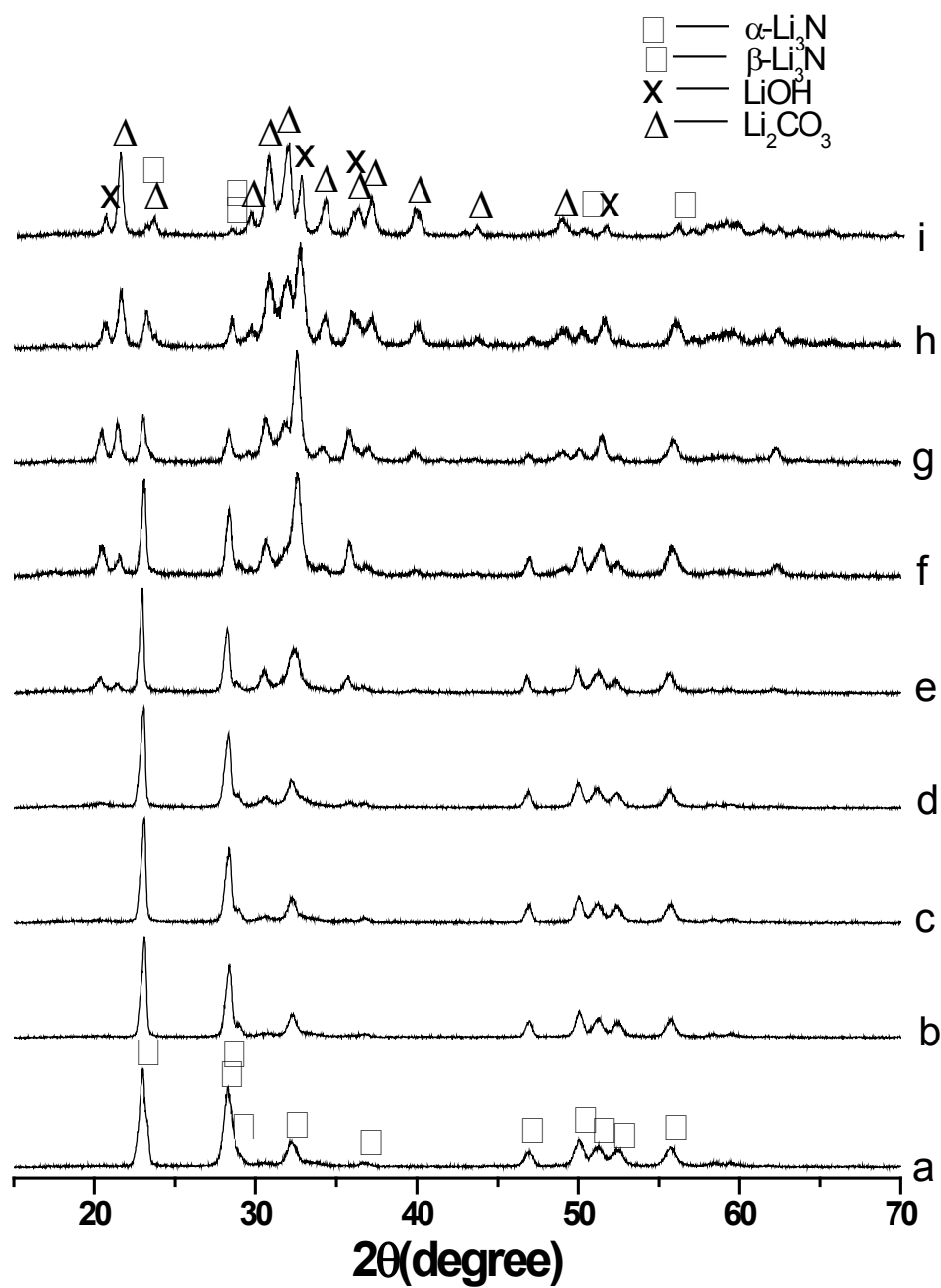


Figure 5.4 XRD patterns of Li_3N exposed to air for (a) 0 min, (b) 15 min, (c) 30 min, (d) 1 h, (e) 2 h, (f) 4 h, (g) 14 h (h) 32 h, and (i) 100 h.

Table 5.1 Molar ratio of β -Li₃N to α -Li₃N in the Li₃N sample exposed to air.

Time in air (h)	Molar ratio of β -Li ₃ N to α -Li ₃ N
0	0.448
0.25	0.420
0.5	0.378
1	0.335
2	0.238
4	0.156
14	0.050
32	0.038
100	0.027

FT-IR spectra were also employed to evaluate the structure change of Li₃N due to its exposure to air. As shown in Figure 5.5a, one can see that Li₃N without exposure to air does not show any IR absorption in the frequency range of 800-4000 cm⁻¹. This happened because the electric vector perpendicular to the z axis of Li₃N exhibited IR absorption only in 200-800 cm⁻¹ [138, 139]. After Li₃N was exposed to air, four absorption bands occurred at around 860, 1088, 1420, and 3678 cm⁻¹. The three absorption bands at 860, 1088, and 1420 cm⁻¹, which are corresponding to the bending, symmetric stretching, and asymmetric stretching vibrations of Li₂CO₃, respectively [140, 141], indicate the formation of Li₂CO₃. The O-H stretching of

LiOH can explain the IR absorption band at 3678 cm^{-1} [142]. Therefore, those FT-IR absorption bands supports the XRD results that the exposure of Li_3N to air generated Li_2CO_3 and LiOH.

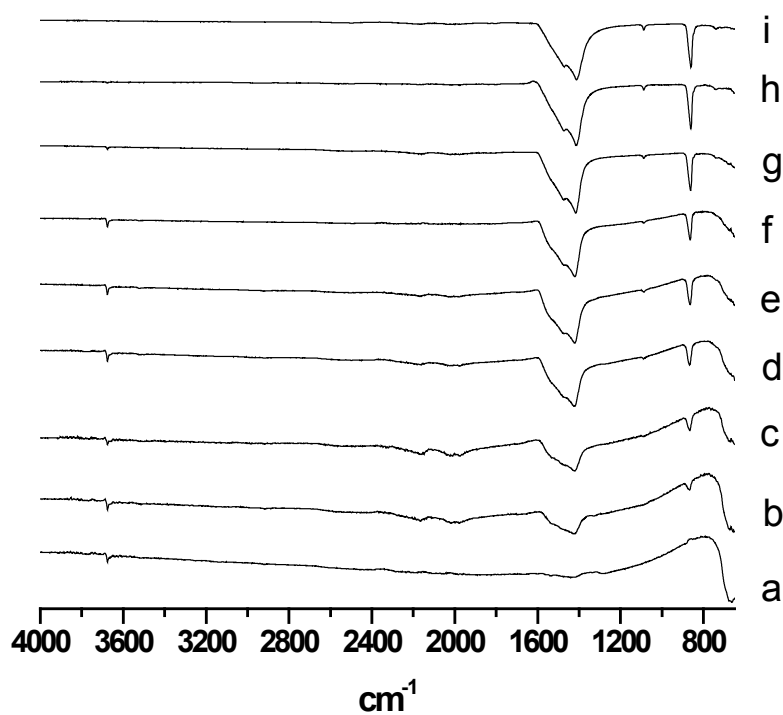


Figure 5.5 FTIR spectra of Li_3N exposed to air for (a) 0 min, (b) 15 min, (c) 30 min, (d) 1 h, (e) 2 h, (f) 4 h, (g) 14 h (h) 32 h, and (i) 100 h.

UV-vis absorption spectra were recorded for Li_3N powder samples that were previously exposed to air (relative humidity of 16%) or wet air (relative humidity of 88%). As shown in Figure 5.6A and B, the exposure of Li_3N to air caused a remarkably decrease in UV/visible absorption. This occurred because of formation of LiOH and Li_2CO_3 , both of which have very low absorbance at the wavelength range of 400-800 nm (Figure 5.7). Furthermore, the higher humidity causes the larger decrease in UV-vis absorbance of Li_3N . This further supports the XRD and FT-IR results that Li_3N degradation in air is due to H_2O vapor.

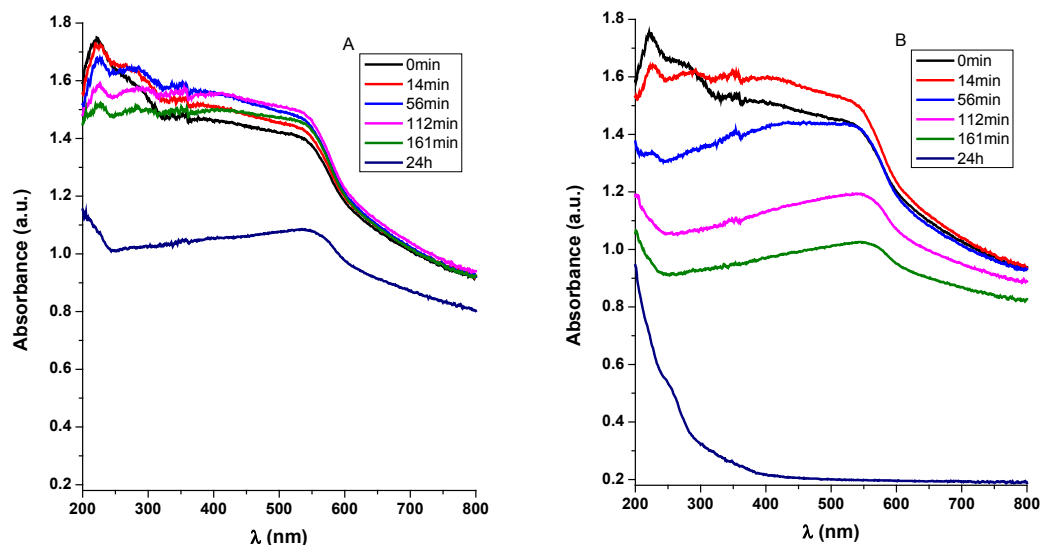


Figure 5.6 UV-vis absorption spectra of Li_3N exposed to (A) air with relative humidity of 16% and (B) air with relative humidity of 88%.

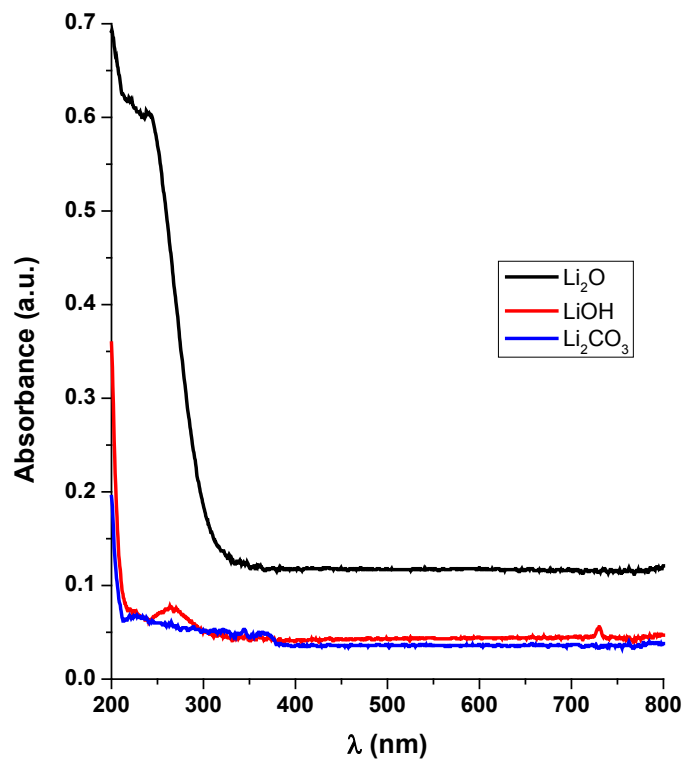


Figure 5.7 UV-vis absorption spectra of individual Li_2O , LiOH , and Li_2CO_3 .

5.4 Conclusion

The degradation of Li_3N in air was evaluated by XRD, FT-IR, and UV-vis absorption. O_2 had no effect on Li_3N at room temperature, because the reaction between Li_3N and O_2 requires a temperature of 230 °C or higher. However, Li_3N exhibited a high reactivity with H_2O vapor in air at room temperature, leading to the conversion of Li_3N to LiOH and then to Li_2CO_3 . Furthermore, it was found that

degradation of β - Li_3N in air was much faster than α - Li_3N . This indicates that α - Li_3N is more stable than β - Li_3N in air.

Chapter 6 Chemical stability of lithium nitride

bromide $\text{Li}_{13}\text{N}_4\text{Br}$ in air *

6.1 Introduction

Battery technology has been playing a key role in modern society because it can be used to power electric and hybrid electric vehicles and to store wind and solar energy in smart grids [143]. Lithium superionic conductors have a promising prospect of making solid state high energy density battery systems. Special attentions have been paid to lithium nitride (Li_3N) because Li_3N has shown high Li^+ conductivity as a potential solid electrolyte [61-65]. However, the thermodynamic decomposition voltage of Li_3N is relatively low at room temperature (0.44V) and it decreases rapidly with the temperature increasing [103]. Therefore, the applicability of binary Li_3N as a solid state electrolyte at elevated temperatures is limited. This has led to the investigation of a series of ternary lithium nitrides which may compensate for this disadvantage.

*The material contained in this chapter was planned for submission to the journal *Industrial and Engineering Chemistry Research* by Junqing Zhang and Yun Hang Hu.

One approach was to partially substitute Li^+ cation of the binary Li_3N with other cations which often have a different valence to increase the disorder or to form new structures, e.g. Li_3AlN_2 has a cubic anti-fluorite type structure with decomposition voltage of 0.85 V at 104 °C [144]. Another approach was to partially substitute N^{3-} anion of the binary Li_3N with other anions, e.g. $\text{Li}_{13}\text{N}_4\text{Br}$ has a decomposition voltage over 1.3 V at 146 °C and 0.65 V at 300 °C [86].

The chemical stability of materials in air is important for guiding how to deal with the materials while being used [145, 146]. For example, a high reactivity of layered lithium cobalt nitride $\text{Li}_{2.13}\text{Co}_{0.43}\text{N}$ with air moisture is found with the rapid appearance of lithium hydroxide and finally leads to the degradation of the nitride into lithium carbonate (Li_2CO_3), cobalt hydroxide ($\text{Co}(\text{OH})_2$) and the release of gaseous ammonia (NH_3) [145]. This suggests handling of $\text{Li}_{2.13}\text{Co}_{0.43}\text{N}$ anodic material in dry air would not damage its electrochemical properties [145]. However, the chemical stability of $\text{Li}_{13}\text{N}_4\text{Br}$ in air has never been studied. In this research, the corrosion process of $\text{Li}_{13}\text{N}_4\text{Br}$ in air is investigated by XRD, TPD-MS, and UV-vis absorption as a function of time. The $\text{Li}_{13}\text{N}_4\text{Br}$ degradation in air reaction order and the energy gap of $\text{Li}_{13}\text{N}_4\text{Br}$ was evaluated by the UV-vis absorption data.

6.2 Experiments

6.2.1 Lithium nitride bromide $\text{Li}_{13}\text{N}_4\text{Br}$ preparation

Lithium nitride powder (99.5%) and lithium bromide reagent (99.9+ %), which had been purchased from Aldrich Chemical Co., were used without any further purification. 80 mol % lithium nitride and 20 mol % lithium bromide were mixed by an agate mortar and pestle for 10 min in an argon filled glove box to protect from moisture. The mixture was placed into a 1/4 -inch- diameter copper tube with one end sealed. The surface of the powder was pressed with a stick by hand. The sample was vacuumed for 2 hours at room temperature and then closed the system. Finally, it was annealed at 400 °C for 20 hours. X-ray diffraction pattern of the resulting sample indicated the formation of the pure lithium nitride bromide $\text{Li}_{13}\text{N}_4\text{Br}$ phase (Figure 6.1a).

6.2.2 X-ray diffraction (XRD)

The XRD measurements were performed with a Scintag XDS2000 Powder Diffractometer equipped with a Cu $\text{K}\alpha$ source, at 45 kV and 35 mA (Figure 2.3). The scanning speed was 1°/min and the scanning range was 10 - 60°. $\text{Li}_{13}\text{N}_4\text{Br}$ sample was covered with plastic wrap during the XRD measurements to prevent from

absorbing H₂O in air. The sample was tested by XRD repeatedly between intervals the sample was exposed in air.

6.2.3 Temperature-programmed decomposition mass spectroscopy (TPD-MS)

The temperature-programmed decomposition mass spectroscopy (TPD-MS) of Li₁₃N₄Br sample was carried out as follows: a suitable amount of sample was loaded into a stainless steel tube reactor, which was located in an electric tube furnace. The temperature of the reactor was increased to 850 °C at a rate of 10 °C/min from room temperature. Helium (30 mL/min) was employed as a carrier gas through the reactor to bring the gaseous product(s) of the decomposition into a mass spectrometer (HP 5970 series mass selective detector, Figure 2.2) generating a TPD-MS profile. The masses from 27.7 to 28.7 were used to detect N₂; the masses from 16.7 to 17.7 were used to detect NH₃; the masses from 17.7 to 18.7 were used to detect H₂O; the masses from 43.7 to 44.7 were used to detect CO₂. The sample was tested by TPD-MS repeatedly between intervals that the sample was exposed in air.

6.2.4 Ultraviolet–visible (UV-vis) absorption

The UV-vis absorption spectra of sample powder were recorded repeatedly with exposing the sample in air for certain intervals, using a UV/vis spectrophotometer (Shimadzu, Model UV-2450, Figure 5.1) in the wavelength range of 200–800 nm at room temperature. Barium sulfate was used as a reference material.

6.3 Results and discussion

6.3.1 XRD and TPD-MS analysis

To observe the structure change of $\text{Li}_{13}\text{N}_4\text{Br}$ in air, XRD was conducted. As shown in Figure 6.1, the XRD pattern of the newly made $\text{Li}_{13}\text{N}_4\text{Br}$ was in agreement with the literature data [88]. After exposing $\text{Li}_{13}\text{N}_4\text{Br}$ to air, new phases of LiBrO_2 , $\alpha\text{-Li}_3\text{N}$, LiOH and Li_2CO_3 were observed. With increasing the exposing time, the relative intensity of LiBrO_2 kept increasing, while $\alpha\text{-Li}_3\text{N}$ phase was observed during the first two hours and disappeared afterwards. This indicates that LiBrO_2 was the final reaction product and Li_3N was the middle reaction product. The O in LiBrO_2 should be from O_2 in the air. Thus, the reaction can be expressed as:



As shown in Figure 6.1, the relative intensity of LiOH first increased and then decreased whereas the relative intensity of Li₂CO₃ increased. This indicates that Li₂CO₃ would be the product of reaction between LiOH and CO₂. In addition, NH₃ was smelled near Li₁₃N₄Br in air. Therefore, the degradation of Li₃N from Li₁₃N₄Br in air can be described as follows:



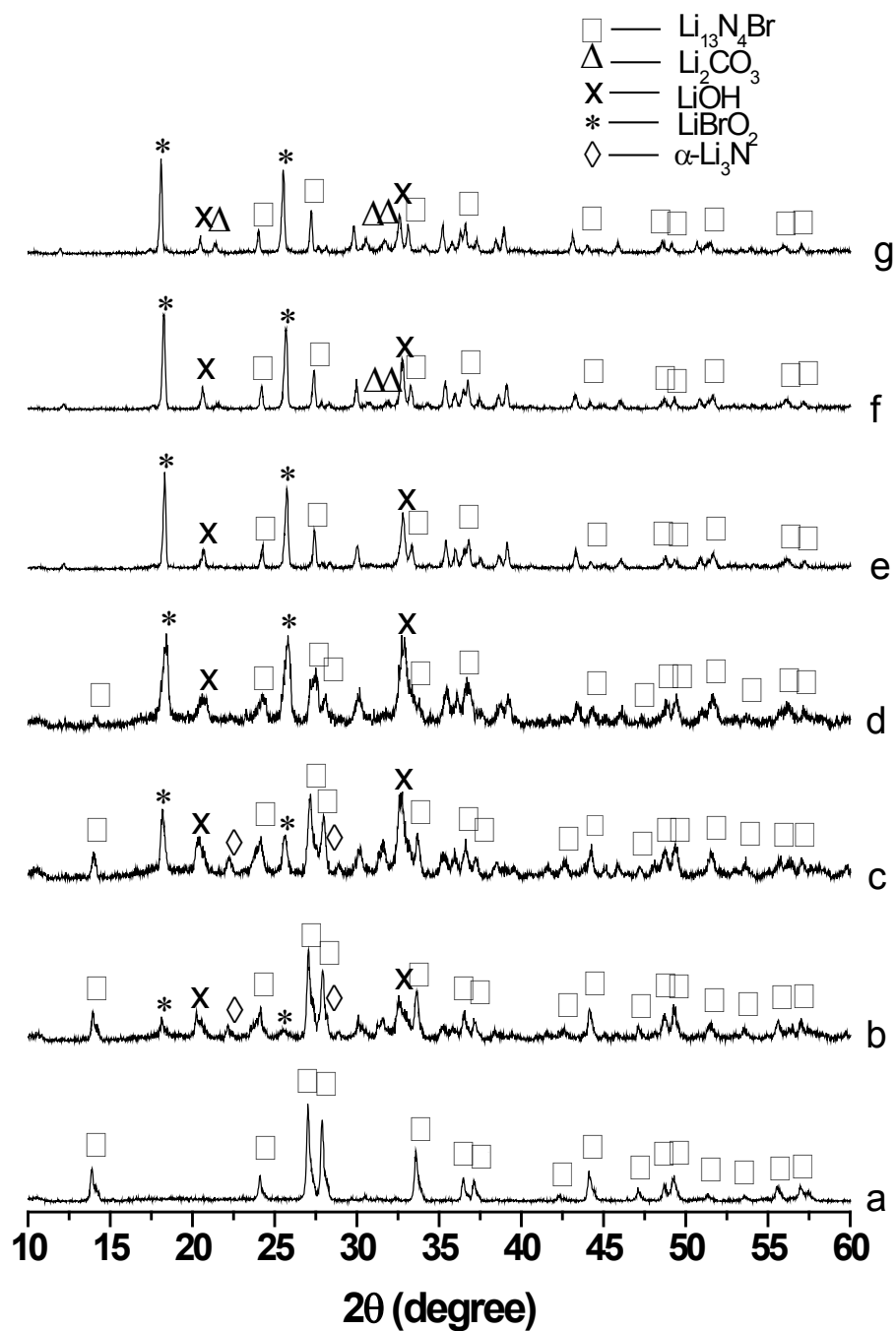


Figure 6.1 XRD patterns of $\text{Li}_{13}\text{N}_4\text{Br}$ in air for various time before testing. (a) Newly made $\text{Li}_{13}\text{N}_4\text{Br}$, (b) 1h, (c) 2h, (d) 4h, (e) 14h, (f) 32h and (g) 100h.

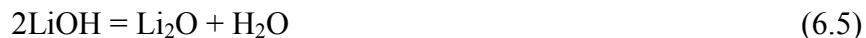
The TPD-MS profiles showed that the decomposition of pure $\text{Li}_{13}\text{N}_4\text{Br}$ only generate N_2 as gas product (Figure 6.2a). This can be explained by equation 6.4:



When $\text{Li}_{13}\text{N}_4\text{Br}$ was exposed in air for 1 or 2h, the decomposition generated mainly NH_3 . This can be explained by equation 6.2.

When $\text{Li}_{13}\text{N}_4\text{Br}$ was exposed in air for a longer time, the decomposition generated H_2O and CO_2 .

The H_2O peak was from the decomposition of LiOH (equation 6.5). As shown in Figure 6.2, the relative intensity of H_2O was increasing first the decreasing afterwards. This is in agreement with the LiOH relative intensity change from its XRD patterns (Figure 6.1).



The CO_2 peak was from the decomposition of Li_2CO_3 (equation 6.6). The increasing of CO_2 is in agreement with the increasing of Li_2CO_3 in the XRD patterns (Figure 6.1).



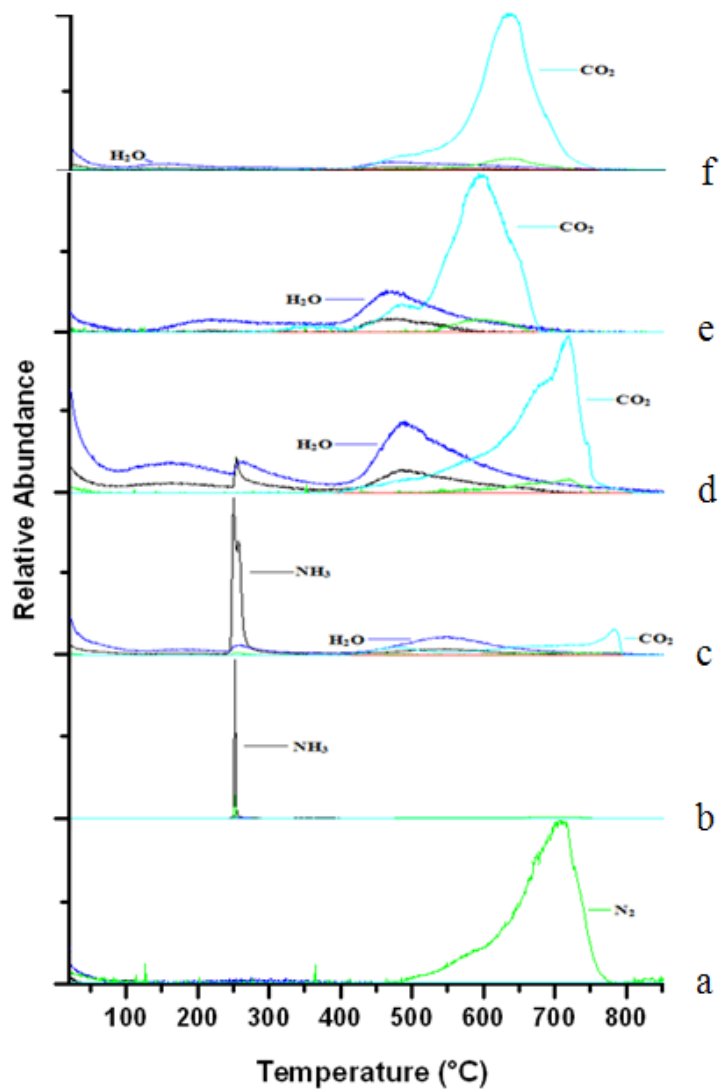


Figure 6.2 TPD-MS profile of $\text{Li}_{13}\text{N}_4\text{Br}$ in air for (a) 0h, (b) 1h, (d) 6h, (d) 30h, (e) 46h, and (f) 150h.

6.3.2 UV-vis absorption analysis

Newly made $\text{Li}_{13}\text{N}_4\text{Br}$ was bright brick red, but its color would get lighter and lighter when it was exposed in air. The UV-vis absorption spectra of $\text{Li}_{13}\text{N}_4\text{Br}$ powder were recorded repeatedly with exposing the sample in air for certain intervals, and the results were shown in Figure 6.3.

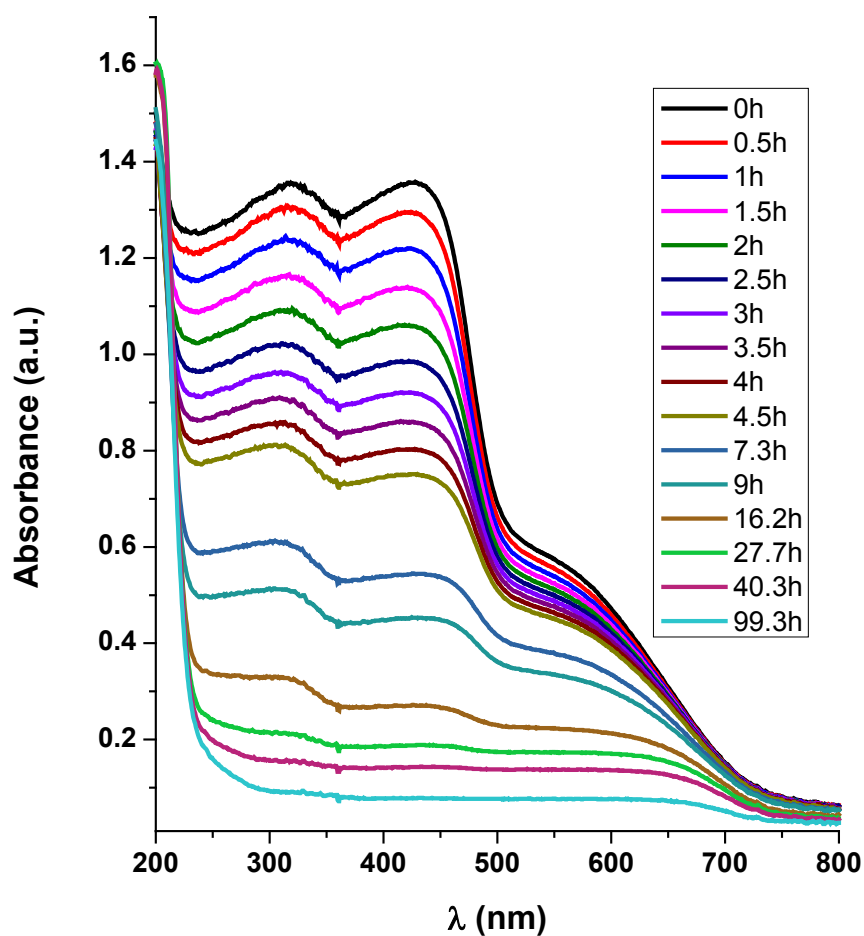


Figure 6.3 UV-vis absorption spectra of (A) $\text{Li}_{13}\text{N}_4\text{Br}$ and (B) $\alpha\text{-Li}_3\text{N}$ in air for various time.

As shown in Figure 6.3, at $t=0$ h, one can see that the absorbance in the high wavelength (low photon energy) region is smaller than in the low wavelength (high photon energy) region. Spectrum shows a sharp edge between 430 to 530 nm. The sharp absorption edge indicates the boundary of the energy of light a solid needed to stimulate electrons from valence band to conduction band. The first derivative of the UV-vis spectroscopy will generate a peak to obtain the energy gap [71, 147-149]. Sotelo-Lerma et al. used the first derivative of the UV-visible absorption spectrum of CdTe to determine its energy gap which is in excellent agreement with accepted values [147]. In addition, Riveros et al. justified the validity of the first derivative method. In this study, the first derivative spectra of $\text{Li}_{13}\text{N}_4\text{Br}$ were obtained from its UV-visible absorbance spectra by using the following equation.

$$\frac{dA}{d(h\nu)} = \frac{dA}{d(\frac{hc}{\lambda})} \quad (6.7)$$

Where A is the absorbance (no unit), h is Planck constant $4.135667516(91) \times 10^{-15}$ (eV·s), c is the speed of light in vacuum 2.99792458×10^8 (m/s), and λ is the wavelength of light (m). Since we already know the relationship between A and λ , it's easy to get the relationship between $dA/d(h\nu)$ and $h\nu$ (Figure 6.4), the energy gap E_g (eV) is the energy at the peak position (Figure 6.4).

The calculated energy gap of $\text{Li}_{13}\text{N}_4\text{Br}$ in this study by the first derivative method is 2.61 eV. By using the data of the UV-vis absorption by $\text{Li}_{13}\text{N}_4\text{Br}$ sample

in air for various time to calculate energy gap, it reached the same value, $E_g=2.61\text{eV}$ (Figure 6.4). It shows the existence of the $\text{Li}_{13}\text{N}_4\text{Br}$ in the sample even when it was exposed in air for 9 h. Even though the concentration of $\text{Li}_{13}\text{N}_4\text{Br}$ had decreased with time, its energy gap could still be precisely calculated by its UV-vis absorption spectra, and the results were keeping the same.

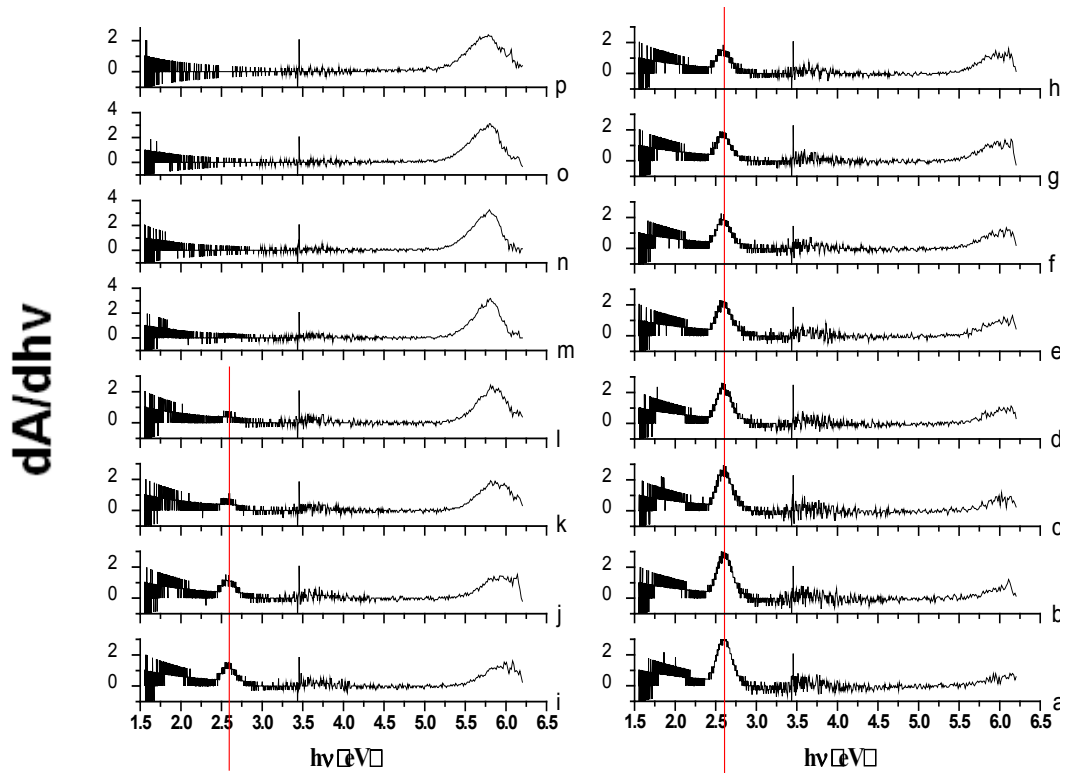


Figure 6.4 The energy gap calculation of sample $\text{Li}_{13}\text{N}_4\text{Br}$ in air for various time. (a) Newly made $\text{Li}_{13}\text{N}_4\text{Br}$, (b) 0.5h, (c) 1h, (d) 1.5h, (e) 2h, (f) 2.5h, (g) 3h, (h) 3.5h, (i) 4h, (j) 4.5h, (k) 7.3h, (l) 9h, (m) 16.2h, (n) 27.7h, (o) 40.3h, (p) 99.3h.

As shown in Figure 6.3, the absorption of the visible light wavelength between 250 and 800 nm by newly made $\text{Li}_{13}\text{N}_4\text{Br}$ is the biggest; the absorbance of this range decreased with time by exposing the sample in air.

All the solid products of the degradation of $\text{Li}_{13}\text{N}_4\text{Br}$, for example, LiOH , Li_2CO_3 , LiBrO_2 are white; the absorbances of visible light by all these products are close to zero. Therefore, the absorbance of the visible light (390 to 750 nm) was caused only by $\text{Li}_{13}\text{N}_4\text{Br}$ in the sample. According to Beer–Lambert law, the concentration of $\text{Li}_{13}\text{N}_4\text{Br}$ in the sample was proportional to its absorbance in the visible light range, the more the concentration of $\text{Li}_{13}\text{N}_4\text{Br}$ in the sample, the larger the absorbance of the visible light by $\text{Li}_{13}\text{N}_4\text{Br}$. We took the 428 nm absorbance (Figure 6.5) represent the concentration of $\text{Li}_{13}\text{N}_4\text{Br}$ in the sample and listed the concentration change with time (Table 6.1).

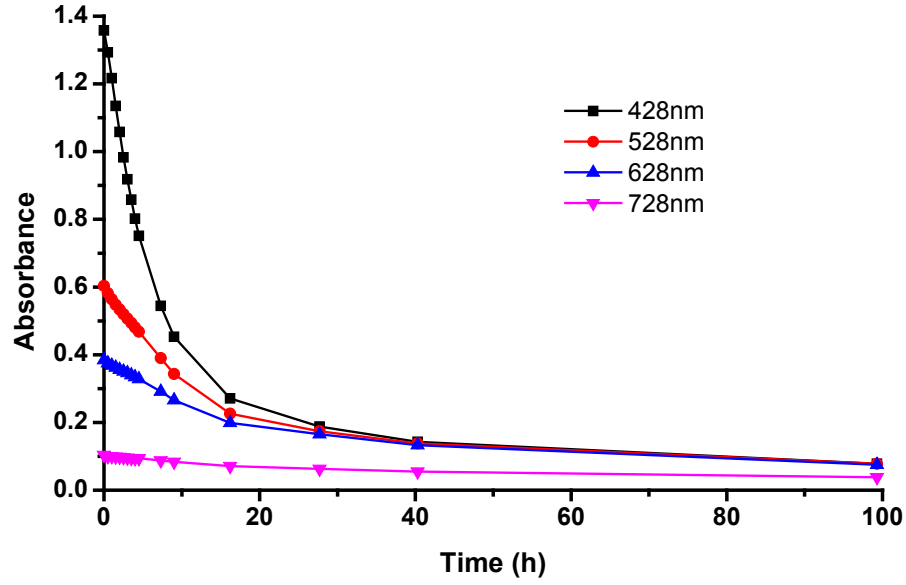


Figure 6.5 UV-vis absorption (at wavelength 428nm, 528nm, 628nm, and 728nm) of $\text{Li}_{13}\text{N}_4\text{Br}$ in air with time.

According to Polangi-Wagner model [118],

$$-\frac{dN}{dt} = A \exp\left(-\frac{E_a}{RT}\right) N^n \quad (6.8)$$

where N is the concentration of $\text{Li}_{13}\text{N}_4\text{Br}$ in the sample; t degradation time, A pre-exponential factor, E_a degradation activation energy, n degradation order, R gas constant, and T absolute temperature. Because the degradation temperature was constant at room temperature, the whole part $A \exp\left(-\frac{E_a}{RT}\right)$ was constant, so equation 6.8 can be rewritten as

$$-\frac{dN}{dt} = k N^n \quad (6.9)$$

where k is constant.

Integrating both side of equation 6.9 can get

$$kt = \begin{cases} -(N - N_0), & \text{when } n = 1 \\ \frac{1}{n-1} \left(\frac{1}{N^{n-1}} - \frac{1}{N_0^{n-1}} \right), & \text{when } n \neq 1 \end{cases} \quad (6.10)$$

where N_0 is the concentration of $\text{Li}_{13}\text{N}_4\text{Br}$ before degradation in air. As we can see from equation 6.10, the concentration of $\text{Li}_{13}\text{N}_4\text{Br}$ in the sample N can has a linear relationship with reaction time t by fitting the reaction order n . Table 6.1 gives the reaction order fitting of the degradation of $\text{Li}_{13}\text{N}_4\text{Br}$ in air. Figure 6.6 and Figure 6.7 give the reaction order fitting of the degradation of $\text{Li}_{13}\text{N}_4\text{Br}$ in air: $N - t$, $\ln(N) - t$, $1/N - t$, $1/N^{1.43} - t$, and $1/N^2 - t$. As we can see, the reaction order $n = 2.43$ ($n-1 = 1.43$) is the best fitting.

Table 6.1 Reaction order fitting of the degradation of $\text{Li}_{13}\text{N}_4\text{Br}$ in air.

time (h)	N	$\ln N$	$1/N$	$1/N^{1.43}$	$1/N^2$
0.00	1.36	0.31	0.74	0.65	0.54
0.50	1.29	0.26	0.77	0.69	0.60
1.00	1.22	0.20	0.82	0.76	0.68
1.50	1.14	0.13	0.88	0.83	0.78
2.00	1.06	0.06	0.95	0.92	0.89
2.50	0.98	-0.02	1.02	1.02	1.03
3.00	0.92	-0.09	1.09	1.13	1.19
3.50	0.86	-0.15	1.17	1.24	1.36
4.00	0.80	-0.22	1.25	1.37	1.55
4.50	0.75	-0.29	1.33	1.51	1.77
7.33	0.54	-0.61	1.84	2.39	3.38
9.00	0.45	-0.79	2.21	3.10	4.87
16.17	0.27	-1.31	3.69	6.47	13.62
27.67	0.19	-1.67	5.32	10.91	28.29
40.33	0.14	-1.94	6.99	16.14	48.90
99.33	0.08	-2.55	12.82	38.40	164.37

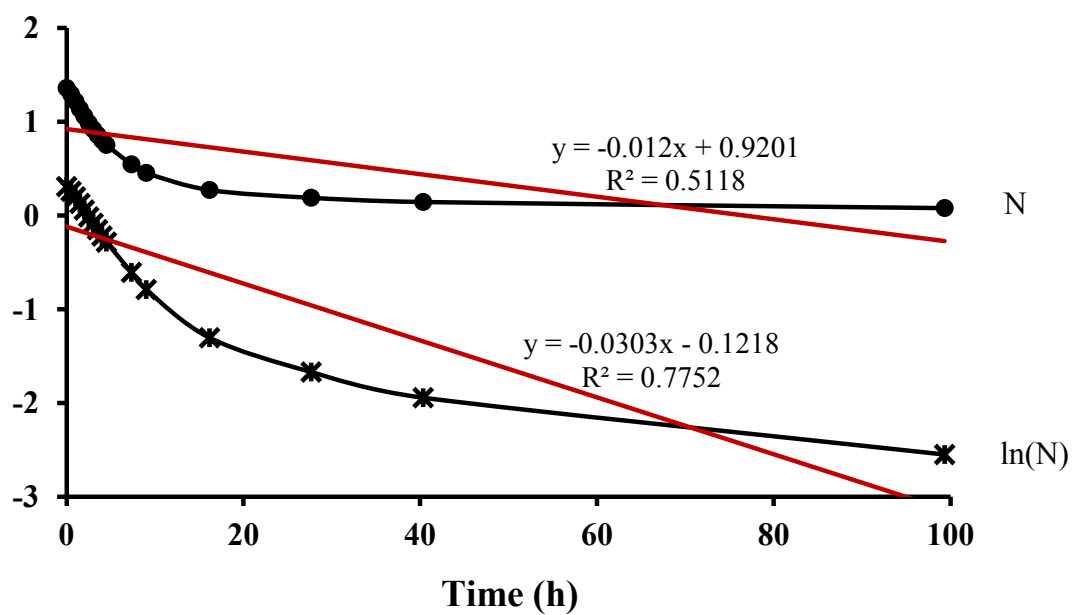


Figure 6.6 Reaction order fitting of the degradation of $\text{Li}_{13}\text{N}_4\text{Br}$ in air: $N - t$ and $\ln(N) - t$.

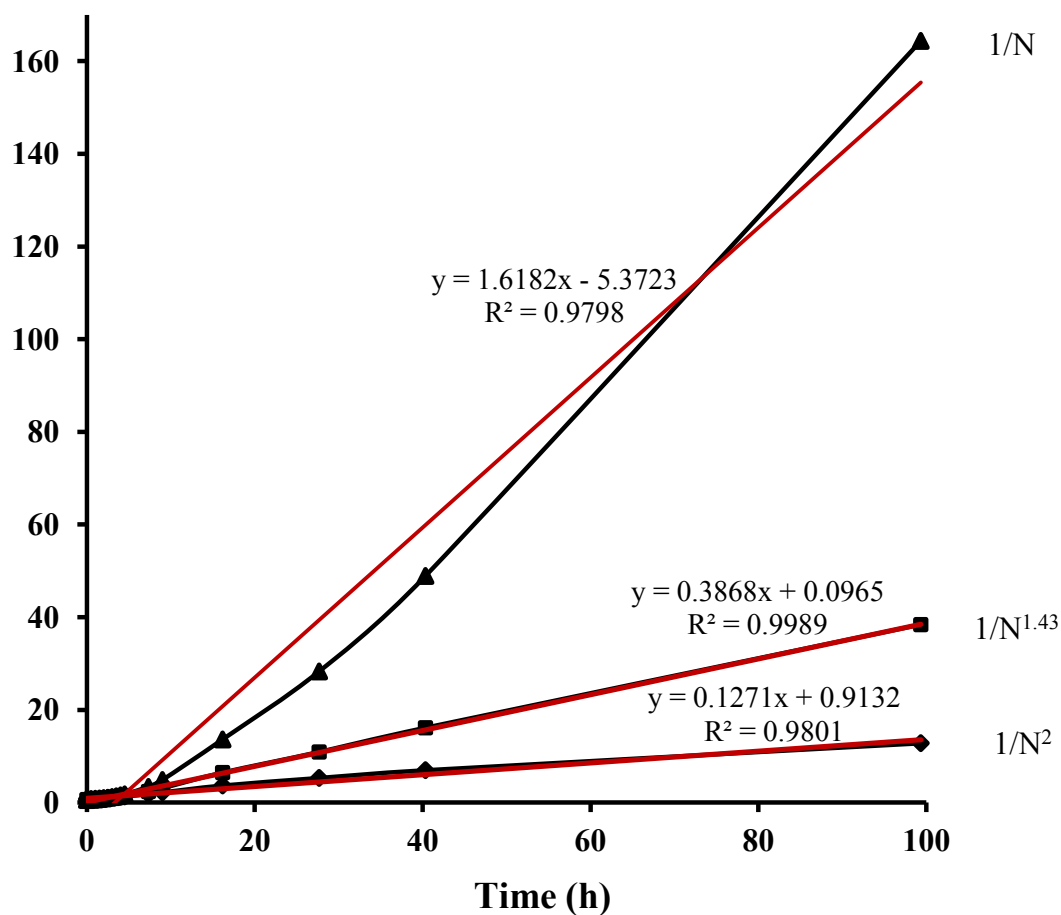


Figure 6.7 Reaction order fitting of the degradation of $\text{Li}_{13}\text{N}_4\text{Br}$ in air: $1/N - t$, $1/N^{1.43} - t$, and $1/N^2 - t$.

6.4 Conclusion

The chemical stability of $\text{Li}_{13}\text{N}_4\text{Br}$ in air has been investigated by XRD, TPD-MS, and UV-vis absorption as a function of time. A high reactivity of the lithium nitride bromide ($\text{Li}_{13}\text{N}_4\text{Br}$) with oxygen and water in air is found with the rapid color change of the sample, from bright brick red to white. The aging process

finally leads to the degradation of the lithium nitride bromide ($\text{Li}_{13}\text{N}_4\text{Br}$) into lithium carbonate (Li_2CO_3), lithium bromite (LiBrO_2) and the release of gaseous NH_3 . The reaction order $n = 2.43$ is the best fitting for the $\text{Li}_{13}\text{N}_4\text{Br}$ degradation in air reaction. $\text{Li}_{13}\text{N}_4\text{Br}$ energy gap was calculated to be 2.61 eV.

Chapter 7 Summary

The decompositions of LiNH_2 and Li_2NH were evaluated. It was found that the decomposition of LiNH_2 produced Li_2NH and NH_3 via two-steps: LiNH_2 into a stable intermediate species ($\text{Li}_{1.5}\text{NH}_{1.5}$) and then into Li_2NH .

The decomposition of Li_2NH produced Li , N_2 and H_2 via two steps: (1) Li_2NH into Li_4NH , N_2 , and H_2 and (2) Li_4NH into Li , N_2 , and H_2 . The first step is the second-order reaction with activation energy of 533.6 kJ/mol, whereas the second step is the first-order reaction with activation energy of 754.2 kJ/mol. Li_4NH , which was generated in the decomposition of Li_2NH , formed a solid solution with Li_2NH . In the solid solution, Li_4NH possesses a similar cubic structure as Li_2NH . The lattice parameter of cubic Li_4NH is 0.5033 nm.

Chloride ion (Cl^-) had great effects on the decompositions of LiNH_2 and Li_2NH . The introduction of Cl^- resulted in the generation of a new peak at low temperature of about 250 °C besides the original peak at 330 °C in the decomposition of LiNH_2 into Li_2NH and NH_3 . Furthermore, Cl^- showed an even greater effect on the decomposition of Li_2NH , namely, the two peaks in TPD profiles merged into one and the peak temperature decrease from 645 to 530 °C with increasing molar ratio of LiCl to LiNH_2 .

The degradation of Li_3N in air was evaluated by XRD, FT-IR, and UV-vis absorption. O_2 had no effect on Li_3N at room temperature, because the reaction between Li_3N and O_2 requires a temperature of 230 °C or higher. However, Li_3N

exhibited a high reactivity with H₂O vapor in air at room temperature, leading to the conversion of Li₃N to LiOH and then to Li₂CO₃. Furthermore, it was found that degradation of β-Li₃N in air was much faster than α-Li₃N. This indicates that α-Li₃N is more stable than β-Li₃N in air.

The chemical stability of Li₁₃N₄Br in air has been investigated by XRD, TPD-MS, and UV-vis absorption as a function of time. A high reactivity of the lithium nitride bromide (Li₁₃N₄Br) with air moisture is found with the rapid color change of the sample, from bright brick red to white. The aging process finally leads to the degradation of the lithium nitride bromide (Li₁₃N₄Br) into lithium carbonate (Li₂CO₃), lithium bromite (LiBrO₂) and the release of gaseous NH₃. The reaction order $n = 2.43$ is the best fitting for the Li₁₃N₄Br degradation in air reaction. Li₁₃N₄Br energy gap was calculated to be 2.61 eV.

References

1. DOE, *Annual Energy Review 2011*. U.S. Energy Information Administration: p. 144.
2. Schlapbach, L. and A. Züttel, *Hydrogen-storage materials for mobile applications*. Nature, 2001. **414**(6861): p. 353-358.
3. Fichtner, M., *Nanotechnological aspects in materials for hydrogen storage*. Advanced Engineering Materials, 2005. **7**(6): p. 443-455.
4. Thomas, G., *Overview of storage development DOE hydrogen program*. Presented at the U.S. DOE hydrogen program 2000 annual review, San Ramon, CA.
5. Migliardini, F., O. Veneri, and P. Corbo, *Hydrogen and proton exchange membrane fuel cells for clean road transportation*. Journal of Industrial and Engineering Chemistry, 2011. **17**(3): p. 633-641.
6. DOE, *Targets for onboard hydrogen storage systems for light-duty vehicles*. US department of energy, office of energy efficiency and renewable energy and the FreedomCAR and fuel partnership, 2009.
7. Züttel, A., *Hydrogen storage methods*. Naturwissenschaften, 2004. **91**(4): p. 157-172.
8. Leung, W.B., N.H. March, and H. Motz, *Primitive phase diagram for hydrogen*. Physics Letters A, 1976. **56**(6): p. 425-426.

9. Yoon, J.H., *Pressure-dependent hydrogen encapsulation in Na12-zeolite A*. The Journal of Physical Chemistry, 1993. **97**(22): p. 6066-6068.
10. Dillon, A.C. and M.J. Heben, *Hydrogen storage using carbon adsorbents: past, present and future*. Applied Physics a-Materials Science & Processing, 2001. **72**(2): p. 133-142.
11. Rosi, N.L., et al., *Hydrogen storage in microporous metal-organic frameworks*. Science, 2003. **300**(5622): p. 1127-1129.
12. Hu, Y.H. and L. Zhang, *Hydrogen storage in metal-organic frameworks*. Advanced Materials, 2010. **22**(20): p. E117-E130.
13. Chae, H.K., et al., *A route to high surface area, porosity and inclusion of large molecules in crystals*. Nature, 2004. **427**(6974): p. 523-527.
14. Furukawa, H., M.A. Miller, and O.M. Yaghi, *Independent verification of the saturation hydrogen uptake in MOF-177 and establishment of a benchmark for hydrogen adsorption in metal-organic frameworks*. Journal of Materials Chemistry, 2007. **17**(30): p. 3197-3204.
15. Sinke, G.C., et al., *Thermodynamic Properties of Aluminum Hydride*. The Journal of Chemical Physics, 1967. **47**(8): p. 2759-2761.
16. Siegel, D.J., C. Wolverton, and V. Ozoliņš, *Thermodynamic guidelines for the prediction of hydrogen storage reactions and their application to destabilized hydride mixtures*. Physical Review B, 2007. **76**(13): p. 134102.
17. Libowitz, G.G., H.F. Hayes, and T.R.P. Gibb, *The System Zirconium–Nickel and Hydrogen*. The Journal of Physical Chemistry, 1958. **62**(1): p. 76-79.

18. Reilly, J.J. and R.H. Wiswall, *Reaction of hydrogen with alloys of magnesium and nickel and the formation of Mg_2NiH_4* . Inorganic Chemistry, 1968. **7**(11): p. 2254-2256.
19. Sandrock, G., *A panoramic overview of hydrogen storage alloys from a gas reaction point of view*. Journal of Alloys and Compounds, 1999. **293–295**(0): p. 877-888.
20. Orimo, S.-i., et al., *Complex Hydrides for Hydrogen Storage*. Chemical Reviews, 2007. **107**(10): p. 4111-4132.
21. Yang, J., et al., *High capacity hydrogen storage materials: attributes for automotive applications and techniques for materials discovery*. Chemical Society Reviews, 2010. **39**(2): p. 656-675.
22. Zhou, L., *Progress and problems in hydrogen storage methods*. Renewable and Sustainable Energy Reviews, 2005. **9**(4): p. 395-408.
23. Jain, I.P., P. Jain, and A. Jain, *Novel hydrogen storage materials: A review of lightweight complex hydrides*. Journal of Alloys and Compounds, 2010. **503**(2): p. 303-339.
24. Thomas, G.J., et al., *Microstructural characterization of catalyzed $NaAlH_4$* . Journal of Alloys and Compounds, 2002. **330–332**(0): p. 702-707.
25. Mao, W.L. and H.K. Mao, *Hydrogen storage in molecular compounds*. Proceedings of the National Academy of Sciences of the United States of America, 2004. **101**(3): p. 708-710.

26. Mao, W.L., et al., *Hydrogen clusters in clathrate hydrate*. Science, 2002. **297**(5590): p. 2247-2249.
27. Florusse, L.J., et al., *Stable low-pressure hydrogen clusters stored in a binary clathrate hydrate*. Science, 2004. **306**(5695): p. 469-471.
28. Lee, H., et al., *Tuning clathrate hydrates for hydrogen storage*. Nature, 2005. **434**(7034): p. 743-746.
29. Patchkovskii, S. and J.S. Tse, *Thermodynamic stability of hydrogen clathrates*. Proceedings of the National Academy of Sciences, 2003. **100**(25): p. 14645-14650.
30. Hu, Y.H. and E. Ruckenstein, *Clathrate Hydrogen Hydrate—A Promising Material for Hydrogen Storage*. Angewandte Chemie International Edition, 2006. **45**(13): p. 2011-2013.
31. Dafert, F.W. and R. Miklauz, *Über einige neue Verbindungen von Stickstoff und Wasserstoff mit Lithium*. Monatshefte für Chemie und verwandte Teile anderer Wissenschaften, 1910. **31**(9): p. 981-996.
32. Ruff, O. and H. Goerges, *Über das Lithium-imid und einige Bemerkungen zu der Arbeit von Dafert und Miklauz: “Über einige neue Verbindungen von Stickstoff und Wasserstoff mit Lithium”*. Berichte der deutschen chemischen Gesellschaft, 1911. **44**(1): p. 502-506.
33. Chen, P., et al., *Interaction of hydrogen with metal nitrides and imides*. Nature, 2002. **420**(6913): p. 302-304.

34. Hu, Y.H. and E. Ruckenstein, *Ultrafast reaction between LiH and NH₃ during H₂ storage in Li₃N*. Journal of Physical Chemistry A, 2003. **107**(46): p. 9737-9739.
35. Hu, Y.H. and E. Ruckenstein, *Highly Effective Li₂O/Li₃N with Ultrafast Kinetics for H₂ Storage*. Industrial & Engineering Chemistry Research, 2004. **43**(10): p. 2464-2467.
36. Hu, Y.H., N.Y. Yu, and E. Ruckenstein, *Effect of the heat pretreatment of Li₃N on Its H₂ storage performance*. Industrial and Engineering Chemistry Research, 2004. **43**(15): p. 4174-4177.
37. Hu, Y.H., N.Y. Yu, and E. Ruckenstein, *Hydrogen storage in Li₃N: Deactivation caused by a high dehydrogenation temperature*. Industrial and Engineering Chemistry Research, 2005. **44**(12): p. 4304-4309.
38. Hu, Y.H. and E. Ruckenstein, *High reversible hydrogen capacity of LiNH₂/Li₃N mixtures*. Industrial and Engineering Chemistry Research, 2005. **44**(5): p. 1510-1513.
39. Ichikawa, T., et al., *Mechanism of novel reaction from LiNH₂ and LiH to Li₂NH and H₂ as a promising hydrogen storage system*. Journal of Physical Chemistry B, 2004. **108**(23): p. 7887-7892.
40. Ichikawa, T., et al., *Hydrogen storage properties in Ti catalyzed Li-N-H system*. Journal of Alloys and Compounds, 2005. **404**: p. 435-438.
41. Nakamori, Y., et al., *Synthesis of LiNH₂ films by vacuum evaporation*. Journal of Alloys and Compounds, 2004. **377**(1-2): p. L1-L3.

42. Kojima, Y. and Y. Kawai, *Hydrogen storage of metal nitride by a mechanochemical reaction*. Chemical Communications, 2004(19): p. 2210-2211.
43. Markmaitree, T., R. Ren, and L.L. Shaw, *Enhancement of lithium amide to lithium imide transition via mechanical activation*. Journal of Physical Chemistry B, 2006. **110**(41): p. 20710-20718.
44. Yang, J., A. Sudik, and C. Wolverton, *Activation of hydrogen storage materials in the Li-Mg-N-H system: Effect on storage properties*. Journal of Alloys and Compounds, 2007. **430**(1-2): p. 334-338.
45. Dolotko, O., et al., *Mechanochemical transformations in Li(Na)AlH₄-Li(Na)NH₂ systems*. Acta Materialia, 2007. **55**(9): p. 3121-3130.
46. Luo, W.F., *(LiNH₂-MgH₂): a viable hydrogen storage system*. Journal of Alloys and Compounds, 2004. **381**(1-2): p. 284-287.
47. Ichikawa, T., et al., *Lithium nitride for reversible hydrogen storage*. Journal of Alloys and Compounds, 2004. **365**(1-2): p. 271-276.
48. Nakamori, Y. and S. Orimo, *Li-N based hydrogen storage materials*. Materials Science and Engineering B-Solid State Materials for Advanced Technology, 2004. **108**(1-2): p. 48-50.
49. Yao, J.H., et al., *Desorption characteristics of mechanically and chemically modified LiNH₂ and (LiNH₂+ LiH)*. Journal of Alloys and Compounds, 2007. **432**(1-2): p. 277-282.

50. Gregory, D.H., *Lithium nitrides, imides and amides as lightweight, reversible hydrogen stores*. Journal of Materials Chemistry, 2008. **18**(20): p. 2321-2330.
51. Gregory, D.H., *Lithium nitrides as sustainable energy materials*. The Chemical Record, 2008. **8**(4): p. 229-239.
52. Hu, Y.H. and E. Ruckenstein, *Ultrafast Reaction between Li_3N and LiNH_2 To Prepare the Effective Hydrogen Storage Material Li_2NH* . Industrial & Engineering Chemistry Research, 2006. **45**(14): p. 4993-4998.
53. Kojima, Y. and Y. Kawai, *IR characterizations of lithium imide and amide*. Journal of Alloys and Compounds, 2005. **395**(1–2): p. 236-239.
54. Moody, G.J. and J.D.R. Thomas, *Alkali metal nitrides*. Journal of Chemical Education, 1966. **43**(4): p. 205.
55. Fischer, D. and M. Jansen, *Synthesis and Structure of Na_3N* . Angewandte Chemie International Edition, 2002. **41**(10): p. 1755-1756.
56. Fischer, D., et al., *Zur Synthese und Struktur von K_3N* . Zeitschrift für anorganische und allgemeine Chemie, 2004. **630**(1): p. 156-160.
57. Brese, N.E. and M. O'keeffe, *Crystal chemistry of inorganic nitrides*. Structure and Bonding, 1992. **79**: p. 307-378.
58. Zintl, E. and G. Brauer, *Constitution of lithium nitride*. Z. Elektrochem., 1935. **41**: p. 102-107.
59. Rabenau, A. and H. Schulz, *Re-evaluation of the lithium nitride structure*. Journal of the Less Common Metals, 1976. **50**(1): p. 155-159.

60. Gregory, D.H., et al., *Structure of lithium nitride and transition-metal-doped derivatives, $Li_{3-x-y}M_xN$ ($M = Ni, Cu$): a powder neutron diffraction study.* Chemistry of Materials, 2002. **14**(5): p. 2063-2070.
61. Lapp, T., S. Skaarup, and A. Hooper, *Ionic conductivity of pure and doped Li_3N .* Solid State Ionics, 1983. **11**(2): p. 97-103.
62. Brendecke, H. and E. Wagner, *Electronic properties of superionic conductor Li_3N .* Journal of The Electrochemical Society, 1977. **124**(8): p. C305-C305.
63. Wahl, J. and U. Holland, *Local ionic motion in the superionic conductor Li_3N .* Solid State Communications, 1978. **27**(3): p. 237-241.
64. Boukamp, B.A. and R.A. Huggins, *Lithium ion conductivity in lithium nitride.* Physics Letters A, 1976. **58**(4): p. 231-233.
65. Alpen, U.V., A. Rabenau, and G.H. Talat, *Ionic conductivity in Li_3N single crystals.* Applied Physics Letters, 1977. **30**(12): p. 621-623.
66. Schulz, H. and K.H. Thiemann, *Defect structure of the ionic conductor lithium nitride (Li_3N).* Acta Crystallographica Section A, 1979. **35**(MAR): p. 309-314.
67. Mali, M., J. Roos, and D. Brinkmann, *Nuclear-magnetic-resonance evidence for a new phase induced by pressure in the superionic conductor Li_3N .* Physical Review B, 1987. **36**(7): p. 3888-3890.
68. Schon, J.C., M.A.C. Wevers, and M. Jansen, *Prediction of high pressure phases in the systems Li_3N , Na_3N , $(Li,Na)_3N$, Li_2S and Na_2S .* Journal of Materials Chemistry, 2001. **11**(1): p. 69-77.

69. Beister, H.J., et al., *Phase transformations of lithium nitride under pressure*. Angewandte Chemie International Edition, 1988. **27**(8): p. 1101-1103.
70. Li, W., et al., *Li^+ ion conductivity and diffusion mechanism in α - Li_3N and β - Li_3N* . Energy & Environmental Science, 2010. **3**(10): p. 1524-1530.
71. Huo, Y. and Y.H. Hu, *UV-visible absorption spectrum determination of optical energy gaps of α and β lithium nitrides*. Journal of Physics and Chemistry of Solids, 2012. **73**(8): p. 999-1002.
72. Ho, A.C., et al., *Experimental and theoretical study of Li_3N at high pressure*. Physical Review B, 1999. **59**(9): p. 6083-6086.
73. Lazicki, A., et al., *New cubic phase of Li_3N : stability of the N^{3-} ion to 200 GPa*. Physical Review Letters, 2005. **95**(16): p. 165503.
74. Brendecke, H. and W. Bludau, *Optical absorption of lithium nitride*. Journal of Applied Physics, 1979. **50**(7): p. 4743-4746.
75. Brendecke, H. and W. Bludau, *Photoluminescence properties of lithium nitride*. Physical Review B, 1980. **21**(2): p. 805-815.
76. Kerker, G., *Electronic structure of Li_3N* . Physical Review B, 1981. **23**(12): p. 6312-6318.
77. Dovesi, R., et al., *Hartree-Fock study of crystalline lithium nitride*. Physical Review B, 1984. **30**(2): p. 972-979.
78. Lazicki, A., et al., *Pressure-induced loss of electronic interlayer state and metallization in the ionic solid Li_3N : Experiment and theory*. Physical Review B, 2008. **78**(15): p. 155133.

79. Fister, T.T., et al., *The local electronic structure of α -Li₃N*. Journal of Chemical Physics, 2008. **129**(4): p. 044702.
80. Wu, S.N., et al., *Electronic structure and vacancy formation of Li₃N*. Applied Physics Letters, 2009. **94**(17): p. 172104.
81. Cui, S., et al., *Structural transition of Li₃N under high pressure: A first-principles study*. Solid State Communications, 2009. **149**(15-16): p. 612-615.
82. Li, W., J.F. Chen, and T. Wang, *Electronic and elastic properties of Li₃N under different pressure*. Physica B, 2010. **405**(1): p. 400-403.
83. Hamann, D.R., *Semiconductor charge densities with hard-core and soft-core pseudopotentials*. Physical Review Letters, 1979. **42**(10): p. 662-665.
84. Sattlegger, H. and H. Hahn, *Über Versuche zur Umsetzung von Li₃N mit Lithiumhalogeniden*. Naturwissenschaften, 1964. **51**(22): p. 534-535.
85. Hartwig, P., W. Weppner, and W. Wichelhaus, *Fast ionic lithium conduction in solid lithium nitride chloride*. Materials Research Bulletin, 1979. **14**(4): p. 493-498.
86. Hartwig, P., et al., *Ionic transport in the lithium nitride bromides, Li₆NBr₃ and Li₁₃N₄Br*. Solid State Communications, 1979. **30**(10): p. 601-603.
87. Hartwig, P., et al., *Lithium Nitride Halides—New Solid Electrolytes with High Li⁺ Ion Conductivity*. Angewandte Chemie International Edition in English, 1980. **19**(1): p. 74-75.

88. Hartwig, P., A. Rabenau, and W. Weppner, *Phase equilibria and thermodynamic properties of the Li-N-Cl, Li-N-Br and Li-N-I systems*. Journal of the Less Common Metals, 1981. **80**(1): p. 81-90.
89. Weppner, W., P. Hartwig, and A. Rabenau, *Consideration of lithium nitride halides as solid electrolytes in practical galvanic cell applications*. Journal of Power Sources, 1981. **6**(3): p. 251-259.
90. Kitahama, K., Y. Furukawa, and S. Kawai, *X-ray and pulsed NMR-studies of lithium nitride chlorides in anti-fluorite type structures*. Solid State Communications, 1980. **36**(8): p. 703-705.
91. Obayashi, H., A. Gotoh, and R. Nagai, *Composition dependence of lithium ionic conductivity in lithium nitride-lithium iodide system*. Materials Research Bulletin, 1981. **16**(5): p. 581-585.
92. Kitahama, K., et al., *Synthesis and NMR study of solid electrolytes in the system Li_3N -LiCl*. Solid State Ionics, 1981. **3-4**(AUG): p. 335-339.
93. Marx, R., *Preparation and crystal-structure of lithium trinitride bromide $Li_{10}N_3Br$* . Zeitschrift Fur Naturforschung Section B-a Journal of Chemical Sciences, 1995. **50**(7): p. 1061-1066.
94. Marx, R. and H.M. Mayer, *Preparation and crystal-structure of lithium nitride dibromide, Li_5NBr_2* . Zeitschrift Fur Naturforschung Section B-a Journal of Chemical Sciences, 1995. **50**(9): p. 1353-1358.

95. Marx, R. and H.M. Mayer, *Preparation and lithium sublattice of lithium nitride trihalides, Li_6NHal_3 (Hal=Br, I).* Zeitschrift Fur Naturforschung Section B-a Journal of Chemical Sciences, 1996. **51**(4): p. 525-530.
96. Marx, R., *Preparation and crystal structure of lithium nitride chloride Li_4NCl .* Journal of Solid State Chemistry, 1997. **128**(2): p. 241-246.
97. Marx, R., *Time-of-flight neutron diffraction study on the Li_2O type phases of Li_6NBr_3 .* Journal of Alloys and Compounds, 1997. **256**(1-2): p. 196-206.
98. Marx, R. and R.M. Ibberson, *Time-of-flight neutron diffraction study on the cryolite type phases of Li_6NBr_3 .* Journal of Alloys and Compounds, 1997. **261**(1-2): p. 123-131.
99. Marx, R. and H.M. Mayer, *Preparation and crystal structure of ordered and disordered lithium nitride dichloride, Li_5NCl_2 .* Journal of Solid State Chemistry, 1997. **130**(1): p. 90-96.
100. Marx, R., *Time-of-flight neutron diffraction study on lithium dinitride iodide, Li_7N_2I .* European Journal of Solid State and Inorganic Chemistry, 1998. **35**(3): p. 197-209.
101. Jia, Y. and J. Yang, *Study of the lithium solid electrolytes based on lithium nitride chloride ($Li_9N_2Cl_3$).* Solid State Ionics, 1997. **96**(1-2): p. 113-117.
102. Bräunling, D., et al., *Synthesis, Crystal Structure and Lithium Motion of Li_8SeN_2 and Li_8TeN_2* Zeitschrift für anorganische und allgemeine Chemie, 2010. **636**(6): p. 936-946.

103. Rabenau, A., *Lithium nitride and related materials case study of the use of modern solid state research techniques*. Solid State Ionics, 1982. **6**(4): p. 277-293.
104. David, W.I.F., et al., *A mechanism for non-stoichiometry in the lithium amide/lithium imide hydrogen storage reaction*. Journal of the American Chemical Society, 2007. **129**(6): p. 1594-1601.
105. Crivello, J.C., et al., *Density functional study of Li_4NH and $\text{Li}_{1.5}\text{NH}_{1.5}$ as intermediary compounds during hydrogenation of Li_3N* . Physical Review B, 2010. **81**(10): p. 104113.
106. Juza, R. and K. Opp, *Metallamide und Metallnitride, 25. Mitteilung. Zur Kenntnis des Lithiumimides*. Zeitschrift für anorganische und allgemeine Chemie, 1951. **266**(6): p. 325-330.
107. Pinkerton, F.E., *Decomposition kinetics of lithium amide for hydrogen storage materials*. Journal of Alloys and Compounds, 2005. **400**(1-2): p. 76-82.
108. Alapati, S.V., J.K. Johnson, and D.S. Sholl, *Identification of destabilized metal hydrides for hydrogen storage using first principles calculations*. Journal of Physical Chemistry B, 2006. **110**(17): p. 8769-8776.
109. Weidner, E., et al., *Observation of novel phases during deuteration of lithium nitride from in situ neutron diffraction*. Chemical Physics Letters, 2007. **444**(1-3): p. 76-79.

110. Ohoyama, K., et al., *Revised crystal structure model of Li_2NH by neutron powder diffraction*. Journal of the Physical Society of Japan, 2005. **74**(1): p. 483-487.
111. Noritake, T., et al., *Crystal structure and charge density analysis of Li_2NH by synchrotron X-ray diffraction*. Journal of Alloys and Compounds, 2005. **393**(1-2): p. 264-268.
112. Balogh, M.P., et al., *Crystal structures and phase transformation of deuterated lithium imide, Li_2ND* . Journal of Alloys and Compounds, 2006. **420**(1-2): p. 326-336.
113. Zhang, C.J., M. Dyer, and A. Alavi, *Quantum delocalization of hydrogen in the Li_2NH crystal*. Journal of Physical Chemistry B, 2005. **109**(47): p. 22089-22091.
114. Mueller, T. and G. Ceder, *Effective interactions between the N-H bond orientations in lithium imide and a proposed ground-state structure*. Physical Review B, 2006. **74**(13): p. 134104.
115. Magyari-Köpe, B., V. Ozoliņš, and C. Wolverton, *Theoretical prediction of low-energy crystal structures and hydrogen storage energetics in Li_2NH* . Physical Review B, 2006. **73**(22): p. 220101.
116. Niewa, R. and D.A. Zherebtsov, *Redetermination of the crystal structure of tetralithium mononitride monohydride, Li_4NH* . Zeitschrift Fur Kristallographie-New Crystal Structures, 2002. **217**(3): p. 317-318.

117. Marx, R., *Preparation and crystal structure of lithium nitride hydride, Li_4NH , Li_4ND* . Zeitschrift Fur Anorganische Und Allgemeine Chemie, 1997. **623**(12): p. 1912-1916.
118. Hu, Y.H., *A method for calculating desorption kinetic parameters*. Petrochemical Technology (China), 1986. **15**(3): p. 167-170.
119. Chakrabarti, P., *Anion-binding sites in protein structures*. Journal of Molecular Biology, 1993. **234**(2): p. 463-482.
120. Scheele, J., P. Timmerman, and D.N. Reinhoudt, *A significant effect of anion binding ureas on the product ratio in the palladium(II)-catalyzed hydrocarbonylation of alkenes*. Chemical Communications, 1998(23): p. 2613-2614.
121. Glidewell, C., *The nitrate nitrite controversy*. Chemistry in Britain, 1990. **26**(2): p. 137-140.
122. Holloway, J.M., et al., *Contribution of bedrock nitrogen to high nitrate concentrations in stream water*. Nature, 1998. **395**(6704): p. 785-788.
123. Sun, M. and R. Prins, *A kinetic investigation of the effects of fluorine and nickel on the HDN of toluidine on fully sulfided tungsten sulfide catalysts*. Journal of Catalysis, 2001. **203**(1): p. 192-200.
124. Schwartz, V., M.Y. Sun, and R. Prins, *An EXAFS study of the influence of fluorine on the structure of sulfided $\text{W}/\text{Al}_2\text{O}_3$ and $\text{NiW}/\text{Al}_2\text{O}_3$ catalysts*. Journal of Physical Chemistry B, 2002. **106**(10): p. 2597-2605.

125. Wang, P., X.D. Kang, and H.M. Cheng, *Improved hydrogen storage of TiF_3 -doped NaAlH_4* . Chemphyschem, 2005. **6**(12): p. 2488-2491.
126. Yin, L.-C., et al., *Functional anion concept: effect of fluorine anion on hydrogen storage of sodium alanate*. Physical Chemistry Chemical Physics, 2007. **9**(12): p. 1499-1502.
127. Yin, L., et al., *Thermodynamically tuning LiBH_4 by fluorine anion doping for hydrogen storage: A density functional study*. Chemical Physics Letters, 2008. **450**(4-6): p. 318-321.
128. Ma, L.P., et al., *Superior catalytic effect of TiF_3 over TiCl_3 in improving the hydrogen sorption kinetics of MgH_2 : Catalytic role of fluorine anion*. Acta Materialia, 2009. **57**(7): p. 2250-2258.
129. Pinkerton, F.E., et al., *Hydrogen desorption exceeding ten weight percent from the new quaternary hydride $\text{Li}_3\text{BN}_2\text{H}_8$* . Journal of Physical Chemistry B, 2005. **109**(1): p. 6-8.
130. Aoki, M., et al., *Destabilization of LiBH_4 by mixing with LiNH_2* . Applied Physics a-Materials Science & Processing, 2005. **80**(7): p. 1409-1412.
131. Chater, P.A., et al., *Synthesis and crystal structure of $\text{Li}_4\text{BH}_4(\text{NH}_2)_3$* . Chemical Communications, 2006(23): p. 2439-2441.
132. Chater, P.A., et al., *Synthesis and characterization of amide-borohydrides: New complex light hydrides for potential hydrogen storage*. Journal of Alloys and Compounds, 2007. **446**: p. 350-354.

133. Bevers, E.R.T., et al., *Thermodynamic properties of lithium chloride ammonia complexes for application in a high-lift high temperature chemical heat pump*. Journal of Thermal Analysis and Calorimetry, 2006. **86**(3): p. 825-832.
134. Johnson, C.E., S.E. Wood, and C.E. Crouthamel, *Studies of Lithium Hydride Systems. I. Solid-Liquid Equilibrium in the Lithium Chloride-Lithium Hydride System*. Inorganic Chemistry, 1964. **3**(11): p. 1487-1491.
135. Hu, Y.H. and Y. Huo, *Fast and exothermic reaction of CO₂ and Li₃N into C-N-containing solid Materials*. Journal of Physical Chemistry A, 2011. **115**(42): p. 11678-11681.
136. Trudeau, M.L., *Advanced materials for energy storage*. Mrs Bulletin, 1999. **24**(11): p. 23-24.
137. Abay, B., H.S. Guder, and Y.K. Yogurtcu, *Urbach-Martienssen's tails in layered semiconductor GaSe*. Solid State Communications, 1999. **112**(9): p. 489-494.
138. Chandrasekhar, H.R., et al., *Phonon spectra and lattice dynamics of lithium nitride*. Solid State Communications, 1977. **22**(11): p. 681-684.
139. Chandrasekhar, H.R., et al., *Infrared and raman-spectra and lattice-dynamics of superionic conductor Li₃N*. Physical Review B, 1978. **17**(2): p. 884-893.
140. Brooker, M.H. and J.B. Bates, *Raman and infrared spectral studies of anhydrous Li₂CO₃ and Na₂CO₃*. Journal of Chemical Physics, 1971. **54**(11): p. 4788-4796.

141. Pasierb, P., et al., *Structural properties of $\text{Li}_2\text{CO}_3\text{--BaCO}_3$ system derived from IR and Raman spectroscopy*. Journal of Molecular Structure, 2001. **596**(1–3): p. 151-156.
142. Jones, L.H., *The infrared spectra and structure of LiOH , LiOHH_2O and the deuterium species. Remark on fundamental frequency of OH* . Journal of Chemical Physics, 1954. **22**(2): p. 217-219.
143. Kamaya, N., et al., *A lithium superionic conductor*. Nat Mater, 2011. **10**(9): p. 682-686.
144. Yamane, H., S. Kikkawa, and M. Koizumi, *Lithium aluminum nitride, Li_3AlN_2 as a lithium solid electrolyte*. Solid State Ionics, 1985. **15**(1): p. 51-54.
145. Panabi re, E., et al., *Chemical stability of layered lithium cobalt nitrides in air*. Corrosion Science, 2012. **58**(0): p. 237-241.
146. Cabana, J., et al., *Oxynitrides as electrode materials for lithium-ion batteries - Characterization and performance of $\text{Li}_{7.9}\text{MnN}_{3.2}\text{O}_{1.6}$* . Journal of The Electrochemical Society, 2005. **152**(11): p. A2246-A2255.
147. Sotelo-Lerma, M., R.A. Zingaro, and S.J. Castillo, *Preparation of CdTe coatings using the chemical deposition method*. Journal of Organometallic Chemistry, 2001. **623**(1-2): p. 81-86.
148. Riveros, G., et al., *Electrodeposition and characterization of ZnX ($\text{X}=\text{Se}$, Te) semiconductor thin films*. Bolet n De La Sociedad Chilena De Qu mica, 2002. **47**(4): p. 411-429.

149. Shen, W.Z., *A Novel Approach for the Evaluation of Band Gap Energy in Semiconductors*. International Journal of Infrared and Millimeter Waves, 2002. **23**(1): p. 61-69.

Appendix

Figure 1.1, reference [1]

Copyrights and Reuse

Public domain and use of EIA content

U.S. Government publications are in the public domain and are not subject to copyright protection. You may use and/or distribute any of our data, files, databases, reports, graphs, charts, and other information products that are on our website or that you receive through our email distribution service. However, if you use or reproduce any of our information products, you should use an acknowledgment, which includes the publication date.

http://www.eia.gov/about/copyrights_reuse.cfm

Table 1.1, reference [4]; Table 1.2, reference [6]

Copyright

Materials on the EERE Web site are in the public domain. EERE requests that it be acknowledged as the source in any subsequent use of its information.

<http://www1.eere.energy.gov/webpolicies/#copyright>

Figure 1.2, reference [7]; Figure 1.3, reference [7]

This is a License Agreement between Junqing Zhang ("You") and Springer ("Springer") provided by Copyright Clearance Center ("CCC"). The license consists of your order details, the terms and conditions provided by Springer, and the payment terms and conditions.

License Number	3152830859885
License date	May 19, 2013
Licensed content publisher	Springer
Licensed content publication	Naturwissenschaften
Licensed content title	Hydrogen storage methods
Licensed content author	Andreas Züttel
Licensed content date	Jan 1, 2004
Volume number	91
Issue number	4
Type of Use	Thesis/Dissertation
Portion	Figures
Author of this Springer article	No
Order reference number	
Title of your thesis / dissertation	PROPERTIES AND STRUCTURES OF Li-N BASED HYDROGEN STORAGE MATERIALS
Expected completion date	Jun 2013
Estimated size(pages)	1
Total	0.00 USD

Figure 1.4, reference [53]

This is a License Agreement between Junqing Zhang ("You") and Elsevier ("Elsevier") provided by Copyright Clearance Center ("CCC"). The license consists of your order details, the terms and conditions provided by Elsevier, and the payment terms and conditions.

Supplier	Elsevier Limited The Boulevard, Langford Lane Kidlington, Oxford, OX5 1GB, UK
Registered Company Number	1982084
Customer name	Junqing Zhang
Customer address	1806B, Woodmar Dr. Houghton, MI 49931
License number	3152841507404
License date	May 19, 2013
Licensed content publisher	Elsevier
Licensed content publication	Journal of Alloys and Compounds
Licensed content title	IR characterizations of lithium imide and amide
Licensed content author	Yoshitsugu Kojima, Yasuaki Kawai
Licensed content date	31 May 2005
Licensed content volume number	395
Licensed content issue number	1–2
Number of pages	4
Start Page	236
End Page	239
Type of Use	reuse in a thesis/dissertation
Intended publisher of new work	other
	120

Portion	figures/tables/illustrations
Number of figures/tables/illustrations	1
Format	both print and electronic
Are you the author of this Elsevier article?	No
Will you be translating?	No
Order reference number	
Title of your thesis/dissertation	PROPERTIES AND STRUCTURES OF Li-N BASED HYDROGEN STORAGE MATERIALS
Expected completion date	Jun 2013
Estimated size (number of pages)	1
Elsevier VAT number	GB 494 6272 12
Permissions price	0.00 USD
VAT/Local Sales Tax	0.0 USD / 0.0 GBP
Total	0.00 USD

Figure 4.1, reference [40]

This is a License Agreement between Junqing Zhang ("You") and Elsevier ("Elsevier") provided by Copyright Clearance Center ("CCC"). The license consists of your order details, the terms and conditions provided by Elsevier, and the payment terms and conditions.

Supplier	Elsevier Limited The Boulevard, Langford Lane Kidlington, Oxford, OX5 1GB, UK
Registered Company Number	1982084
Customer name	Junqing Zhang
Customer address	1806B, Woodmar Dr. Houghton, MI 49931
License number	3153080090347
License date	May 20, 2013
Licensed content publisher	Elsevier
Licensed content publication	Journal of Alloys and Compounds
Licensed content title	Hydrogen storage properties in Ti catalyzed Li–N–H system
Licensed content author	T. Ichikawa, N. Hanada, S. Isobe, H. Y. Leng, H. Fujii
Licensed content date	8 December 2005
Licensed content volume number	404–406
Licensed content issue number	
Number of pages	4
Start Page	435
End Page	438
Type of Use	reuse in a thesis/dissertation
Intended publisher of new work	other
Portion	figures/tables/illustrations
Number of figures/tables/illustrations	1
Format	both print and electronic
Are you the author of this Elsevier article?	No
Will you be translating?	No

Order reference number	
Title of your thesis/dissertation	PROPERTIES AND STRUCTURES OF Li-N BASED HYDROGEN STORAGE MATERIALS
Expected completion date	Jun 2013
Estimated size (number of pages)	1
Elsevier VAT number	GB 494 6272 12
Permissions price	0.00 USD
VAT/Local Sales Tax	0.0 USD / 0.0 GBP
Total	0.00 USD

Chapter 2 and Chapter 4

Reprinted (adapted) with permission from (Zhang, J.; Hu, Y. H., Decomposition of Lithium Amide and Lithium Imide with and without Anion Promoter. Ind. Eng. Chem. Res. 2011, 50 (13), 8058-8064). Copyright (2011) American Chemical Society.



Title: Decomposition of Lithium Amide and Lithium Imide with and without Anion Promoter
Author: Junqing Zhang and Yun Hang Hu
Publication: Industrial & Engineering Chemistry Research
Publisher: American Chemical Society
Date: Jul 1, 2011
Copyright © 2011, American Chemical Society

Logged in as:
Junqing Zhang
Account #:
3000649899

[LOGOUT](#)**PERMISSION/LICENSE IS GRANTED FOR YOUR ORDER AT NO CHARGE**

This type of permission/license, instead of the standard Terms & Conditions, is sent to you because no fee is being charged for your order. Please note the following:

- Permission is granted for your request in both print and electronic formats, and translations.
- If figures and/or tables were requested, they may be adapted or used in part.
- Please print this page for your records and send a copy of it to your publisher/graduate school.
- Appropriate credit for the requested material should be given as follows: "Reprinted (adapted) with permission from (COMPLETE REFERENCE CITATION). Copyright (YEAR) American Chemical Society." Insert appropriate information in place of the capitalized words.
- One-time permission is granted only for the use specified in your request. No additional uses are granted (such as derivative works or other editions). For any other uses, please submit a new request.

[BACK](#)[CLOSE WINDOW](#)

Copyright © 2013 [Copyright Clearance Center, Inc.](#) All Rights Reserved. [Privacy statement.](#)
Comments? We would like to hear from you. E-mail us at customer@copyright.com

Chapter 3

To: Junqing Zhang [junqingz@mtu.edu]

Cc: Emre A. Veziroglu [emrev1@cox.net]

Subject: Copyright Permission

Dear Junqing:

Thank you very much for your email of 20 May 2013. In accordance with your request, we are happy to give you permission to use the following article both electronically and in print in your PhD thesis:

"Zhang, Junqing, and Yun Hang Hu. Intermediate Species and Kinetics of Lithium Imide Decomposition. International Journal of Hydrogen Energy 2012, 37 (13), 10467-10472

Wishing you all the best in your endeavors, I remain

Sincerely yours,

A black rectangular box redacting the signature of T. Nejat Veziroglu.

T. Nejat Veziroglu

Founding Editor-in-Chief

International Journal of Hydrogen Energy (IJHE)

5794 SW 40 St. #303

Miami, FL 33155, USA

Tel: 1-305-456-9353

Fax: 1-305-675-3295

Email: veziroglu@iahe.org